Non-Stationary Stochastic Modelling of Climate Hazards for Risk and Reliability Assessment

by

Rituraj Bhadra

A thesis
presented to the University of Waterloo
in fulfillment of the
thesis requirement for the degree of
Doctor of Philosophy
in
Civil Engineering

Waterloo, Ontario, Canada, 2024

© Rituraj Bhadra 2024

Examining Committee Membership

The following served on the Examining Committee for this thesis. The decision of the Examining Committee is by majority vote.

External Examiner:	Dr. Yong Li Associate Professor, Civil and Environmental Engineering Dept., University of Alberta
Internal-External Member:	Dr. Kshirasagar Naik Professor, Dept. of Electrical and Computer Engineering, University of Waterloo
Internal Members:	Dr. Wei-Chau Xie Professor, Dept. of Civil and Environmental Engineering, University of Waterloo
	Dr. Shunde Yin Associate Professor, Dept. of Civil and Environmental Engineering, University of Waterloo
Supervisor:	Dr. Mahesh D. Pandey Professor, Dept. of Civil and Environmental Engineering, University of Waterloo

Author's Declaration

I hereby declare that I am the sole author of this thesis. This is a true copy of the thesis, including any required final revisions, as accepted by my examiners.

I understand that my thesis may be made electronically available to the public.

Abstract

This thesis presents methodologies for studying the effects of climate change on natural hazards. The thesis is structured around three key aspects: first, the stochastic modelling of non-stationary hazards; second, the modelling of concrete degradation in a changing climate; and third, the economic risk evaluation associated with these non-stationary hazards.

The initial focus of this thesis is on applying a non-stationary stochastic process to model the increasing frequency and intensity of climate-driven hazards in Canada. The early chapters provide an overview of the effects of climate change in Canada. To understand the trends and projections of various climatic variables, such as temperature, precipitation, and wind speed, recent studies and reports from Environment and Climate Change Canada, along with other relevant literature, are examined and analyses were performed on the model outputs of the Couple Model Inter-comparison Project Phase 6 (CMIP6) data. The overview highlights the growing occurrence and severity of climate hazards, including hurricanes, droughts, wildfires, and heatwaves, as supported by other independent studies. In the light of such analyses, this study demonstrates the inadequacy of traditional stationary models for future predictions and risk assessments, thereby advocating for a shift to non-stationary frameworks.

The thesis provides a robust theoretical foundation for non-stationary hazard modelling using stochastic process models. Traditional extreme value analysis (EVA) typically assumes stationarity. However, this assumption is invalidated by gradual changes in the frequency and intensity of climate-driven hazards. This research proposes methodologies to model climatic hazards using a non-stationary stochastic shock process, specifically the non-homogeneous Poisson process (NHPP), to derive the maximum value distributions over any finite period and not just restricted to annual maxima. These models account for changes in the underlying processes over time, providing a more accurate representation of climate-driven hazards by incorporating time-varying parameters that reflect the dynamic nature of climatic extremes. By integrating stochasticity and temporal variability, these stochastic process models offer a robust framework for predicting the future occurrence and intensity of climate-driven hazards. The proposed methods are demonstrated through

the estimation of maximum value distributions for precipitation events using the Coupled Model Inter-comparison Project (CMIP) phase-6 multi-model ensemble data, with an analysis of inter-model variability. Furthermore, the thesis presents a case study on modeling heatwaves to illustrate the application of these models to climatic data, particularly for events where the asymptotic assumptions of extreme value theory do not hold.

Climate change will not only influence the loads and hazards on infrastructure, but it will also exacerbate the degradation processes of structures due to harsher climatic conditions such as higher temperatures and increased humidity. To model these effects on the degradation of concrete bridges, simulations were conducted using physico-chemical concrete degradation processes. Based on the simulation results, non-stationary Markov transition probabilities were estimated for several key locations in Canada under various Shared Socioeconomic Pathway (SSP) scenarios.

The final chapter of the thesis addresses the economic aspects of climate-driven hazards. It includes derivations to estimate various statistics of damage costs, such as the mean, variance, moments, and distribution, resulting from a non-stationary hazard process. The analytical results were derived for several cases, such as considering the loss magnitudes to be identically and non-identically distributed, and whether discounting is applied to the losses or not to address the effect of time in evaluating the net present losses or not. This analysis offers valuable information for policy makers, engineers, and scientists involved in climate adaptation and mitigation efforts.

Acknowledgements

I would like to sincerely thank my supervisor, Professor Mahesh Pandey, for giving me the opportunity to join his group as a Ph.D. student. He has mentored and supported me throughout my PhD journey. I am truly grateful for his valuable directions and guidance at every step of this process, which has made this study possible.

I express my heartfelt gratitude to my Ph.D. supervisor, Professor Mahesh Pandey, and other committee members, Professors Wei-Chau Xie, Shunde Yin, and Kshirasagar Naik, for agreeing to be on my committee. Their comments and feedback have been extremely valuable in shaping the course of this thesis.

I also thank Professor Yong Li for agreeing to serve as my external examiner and for providing feedback on my study. I am immensely grateful to him.

I extend my gratitude to Professor C.S. Manohar, who has been a wonderful mentor since my Master's studies and has encouraged me to pursue my PhD. I offer my heartfelt thanks to Professors Arup Guha Niyogi and Shibnath Chakrabarty for recognizing my potential and motivating me to reach where I am today.

I am grateful to the researchers whose revered works have provided me a foundation to extend the knowledge in this area, and to the reviewers, whose constructive criticism and comments have helped me improve the content of my publications.

Heartfelt thanks go to my parents, Nandita Bhadra and Subhasis Bhadra, for supporting and motivating me to accomplish everything I have achieved today, and to my beloved little sister, Ritwika, for bringing a world of happiness into my life.

Special thanks go out to my friends, colleagues, and seniors Abhisek Paul, Indranil Hazra, Sourav Das, Upasana Pandey, Prasanna Salasiya, Rui Wang, Prithwish Jana, Rupam Ghosh, and Cibi Chakraborty, whose companionship and advice have kept me motivated even during the toughest times.

Dedication

This is dedicated to my mother, Smt. Nandita Bhadra.

Table of Contents

Examining Committee ii

Author's Declaration iii

Abstract iv

Acknowledgements vi

Dedication vii

List of Figures xiv

List of Tables xviii

List of Abbreviations xx

List of Symbols xxii

1 Climate Change in Canada: Overview 1

1.1 Introduction 1

1.2 Climate Models 2

1.3 Uncertainties in Climate modeling . . . 2
1.3.1 Sources of uncertainties . . . 2
1.3.2 Tackling the uncertainties . . . 4
1.4 Coupled Model Intercomparison Project (CMIP) . . . 4
1.4.1 CMIP(Phase 5) . . . 5
1.4.2 CMIP (Phase 6) . . . 6
1.5 Weather variables . . . 7
1.6 Ambient temperature . . . 8
1.7 Precipitation and rainfall . . . 9
1.8 Wind pressures . . . 11
1.9 Research Objectives . . . 12
1.10 Thesis organization . . . 13
1.11 Conclusions . . . 14

2 Non-Stationary Probabilistic Analysis of Extremes 16

2.1 Introduction . . . 16
2.2 Extreme Value Theory . . . 17
2.2.1 Stationary Extreme Value Distribution (EVD) . . . 17
2.2.2 Non-stationary EVD . . . 19
2.2.3 Limitations of NS EVD models . . . 21
2.3 Stochastic process model . . . 23
2.3.1 Stationary Poisson process . . . 23
2.3.2 Non-Homogeneous Poisson process (NHPP) . . . 27
2.4 Statistical estimation . . . 34

2.4.1 Gumbel model . . . 34
2.4.2 NHPP model . . . 35
2.5 Conclusion . . . 37

3 Non-Stationary Model of Precipitation Events 39
3.1 Introduction . . . 39
3.1.1 Background . . . 39
3.1.2 Data . . . 40
3.2 Base Period -Stationary climate . . . 42
3.2.1 Gumbel Extreme Value Analysis . . . 42
3.2.2 Stochastic process model . . . 44
3.3 Future period - Non-stationary Climate . . . 48
3.3.1 Non-stationary Gumbel EVA . . . 49
3.3.2 Stochastic process model . . . 52
3.4 Future period : 2070-2100 . . . 60
3.4.1 Non-stationary Gumbel EVA . . . 64
3.4.2 Stochastic process model . . . 64
3.5 Model Pooling . . . 64
3.6 Discussion . . . 67
3.7 Limitations . . . 71
3.8 Conclusions . . . 71

4 Non-Stationary Model of Heatwave Events 73
4.1 Introduction . . . 73
4.1.1 Background . . . 73

4.1.2 Data . . . 75
4.2 Analysis . . . 75
4.2.1 NS Gumbel . . . 76
4.2.2 NHPP . . . 78
4.3 Results . . . 79
4.3.1 Estimated Parameters . . . 79
4.3.2 Maximum value distributions . . . 79
4.3.3 Mean waiting times . . . 84
4.4 Conclusions . . . 84

5 Concrete Degradation in Changing Climate using Markov Process 87
5.1 Introduction . . . 87
5.2 Literature . . . 88
5.3 Research objectives . . . 90
5.4 Concrete degradation process and climate change . . . 90
5.4.1 Climate projections . . . 91
5.4.2 Chloride diffusion . . . 91
5.4.3 Carbonation . . . 93
5.4.4 Reinforcement corrosion . . . 94
5.4.5 Concrete Cracking . . . 95
5.5 Rate of crack-width increase . . . 96
5.6 Analysis . . . 97
5.6.1 Defining the uncertain parameters . . . 97
5.6.2 Markov process model . . . 100

5.6.3 Markov condition states and TPM estimation . . . 102
5.7 Estimation of Markov transition probabilities . . . 104
5.8 Validation . . . 105
5.9 Monte Carlo Simulation cases . . . 105
5.10 Results . . . 106
5.11 Illustrative example . . . 107
5.12 Conclusion . . . 109

6 Estimation of Economic Risk **111**
6.1 Introduction . . . 111
6.1.1 Literature review . . . 112
6.2 Model of economic loss . . . 114
6.3 Case I: IID damage costs . . . 114
6.3.1 Expected damage cost . . . 116
6.3.2 Second moment and variance of damage cost . . . 117
6.3.3 Undiscounted cost . . . 118
6.3.4 Distribution of damage cost . . . 119
6.4 Case II: Time dependent costs . . . 119
6.4.1 Moment generating function . . . 120
6.4.2 Expected loss . . . 122
6.4.3 Variance . . . 123
6.4.4 General n^{th} moment . . . 124
6.5 Simulation based validation of analytical results . . . 125
6.6 Examples . . . 126

6.6.1 Example 1: Tornadoes in Ontario, Canada . . . 126
6.6.2 Example 2: Heat wave (HW) in US cities . . . 131
6.7 Conclusions . . . 134

References **136**

APPENDICES **150**

A Estimated Parameters for Precipitation Analysis **151**
A.1 Stationary case (1950-1990): Benchmark Case . . . 152
A.2 Non-stationary Case I: 2020-2100 Period . . . 153
A.2.1 Non-stationary Gumbel parameters . . . 153
A.2.2 NHPP parameters . . . 154
A.3 Non-stationary Case II: 2070-2100 Period . . . 155
A.3.1 Non-stationary Gumbel parameters . . . 155
A.3.2 NHPP parameters . . . 156

B Markov transition probabilities **157**
B.1 Markov probabilities . . . 157

C Formulas for computing risk **162**
C.1 Variance and second moment of damage costs . . . 162
C.2 Distribution . . . 165

List of Figures

1.1 Increase in mean temperatures of Canada due to Global rise in temperature[15]. 9

1.2 Percentage increase in annual rainfall as a function of the global temperature rise[15] 11

1.3 The percentage increase in hourly wind pressures for 50-year and 10-year return period, as a function of the global temperature rise[15] 12

2.1 Stochastic process 23

2.2 Extreme value distribution for an HPP, Parameters: $X_i's \sim Exponential(\ mean = 10\ units), t = 20\ years$ 26

2.3 Difference in the NHPP annual extreme value CDF for precipitation obtained using direct integration and approx method for the year 2100 for SSP5(8.5) scenario(detailed discussion in Chapter 3). 32

3.1 CMIP6 Multi-model ensemble for the projected annual 24-hour precipitation values for SSP5-8.5 scenario 40

3.2 Fitted Gumbel probability plots for annual maximum precipitation for the base period 1951-1990 43

3.3 Histograms of the Gumbel parameters estimated for the base period showing the inter-model variability. 45

3.4 Weibull Probability Paper Plot with a Location Parameter of 25mm/day (Threshold Value) 46

3.5 Histograms of the fitted Weibull distribution parameters estimated for the base period showing the inter-model variability. 47
3.6 Annual probability of exceedance from the fitted HPP model for the base period 1951-1990. 48
3.7 The median and the 95th percentile values of the Gumbel annual EVD in the future period. 51
3.8 Fit of the mean value function with event times for IPSL.CM6A.LR model output in future period (2020-2100) 53
3.9 Fitted NHPP log-linear rate functions to the models in the future period (2020-2100) 54
3.10 Fitted NHPP log-linear mean value functions to the models in the future period (2020-2100) 55
3.11 Changes in mean value of individual precipitation events in the future period 56
3.12 Histograms of the NHPP parameters estimated for the future period showing the inter-model variability. 58
3.13 The median and the 95th percentile values of the NHPP annual maximas in the future period. 59
3.14 NHPP return periods for given return levels. 61
3.15 NHPP mean waiting time till next event for given return levels. 62
3.16 NHPP mean waiting times compared with the NS Gumbel return period. . 63
3.17 Comparison of the ensemble medians of different percentiles of annual maximas for the non-stationary Gumbel method 65
3.18 Comparison of the ensemble medians of different percentiles of annual maximas for the NHPP analysis 66
3.19 Comparison of the percentiles of annual maximum precipitation obtained as ensemble median and model pooling 68

3.20 Comparison of the ensemble medians of different percentiles of annual maxima for the non-stationary Gumbel method and the NHPP for 2020-2100 period 69

3.21 Comparison of the ensemble medians of different percentiles of annual maxima for the non-stationary Gumbel method and the NHPP reanalyzed for 2070-2100 period 70

4.1 Heatwave duration obtained from the model output KACE-1-0-G (r2i1p1f1) 77

4.2 Rate of occurrence heatwave events 80

4.3 Mean duration of heatwave events 80

4.4 Estimated Gumbel EV percentiles of the annual maximum heatwave duration for SSP5 (8.5) scenario 81

4.5 The median and the 95th percentile of the annual EVD obtained from the NS Gumbel analysis. 82

4.6 Estimated NHPP percentiles of the annual maximum heatwave duration for SSP5 (8.5) scenario 82

4.7 The median and the 95th percentile of the annual maximum value distribution obtained from the NHPP analysis. 83

4.8 The median and the 95th percentile of the annual maximum value distributions obtained from the NS Gumbel and NHPP model for SSP5(8.5) scenario. 84

4.9 The mean waiting times to the next heatwave event of given return level. . 85

5.1 Annual average temperature increase in different provinces (BC: British Columbia, ON: Ontario, QC: Quebec, NS: Nova Scotia) for different Carbon emission scenarios [2] 92

5.2 Simulated temperature realization in the period 2021-2040 100

5.3 Concrete Degradation model and the Condition states 103

5.4 Transition probabilities for British Columbia under RCP8.5 emission scenario 107

5.5 Expected states with time for the different cases 109

6.1 The damage cost process 115

6.2 Verification using Monte Carlo simulation (MCS) 126

6.3 Expected number of tornadoes (Mean value function) until a given year exceeding different threshold wind speeds 129

6.4 Tornado wind speed distribution 130

6.5 Tornado damage costs 131

6.6 Discounted and undiscounted damage costs for the Tornadoes with a threshold of 32.6 m/s (i.e. above F0) and 50.3 m/s (i.e. above F1) 132

6.7 Cumulative distribution of damages 133

6.8 Coefficient of Variation of the damages 134

6.9 Cost in equivalent $^{\circ}C - days$ 135

List of Tables

3.1 Multi-model ensemble and their reporting institutes in CMIP6 for precipitation 41

3.2 Gumbel parameters and percentile values for the base period 1951-1990. . . 42

3.3 Ranges of HPP parameter estimates and percentile values of the EVD for the multi-model ensemble in the base period. 46

3.4 Non-stationary Gumbel parameters 50

3.5 Estimated NHPP Rate and shock height (precipitation) distribution parameters 57

4.1 Estimated parameters of the NHPP model and NS Gumbel distribution . . 79

5.1 Parameter values 98

5.2 Markov condition state definitions 102

6.1 Fujita scale classification 127

A.1 Estimated parameters of the Gumbel distributions and the Homogeneous Poisson Process for all the climate models for the stationary benchmark scenario i.e. 1950-1990 period. 152

A.2 Estimated Parameters of non-stationary Gumbel distributions for all models in the period 2020-2100. 153

A.3 Estimated Parameters of Non-homogeneous Poisson process for all models in the period 2020-2100. 154

A.4 Estimated Parameters of non-stationary Gumbel distributions for all models in the period 2070-2100. 155

A.5 Estimated Parameters of Non-homogeneous Poisson process for all models in the period 2020-2100. 156

B.1 Probabilities for British Columbia 158

B.2 Probabilities for Ontario 159

B.3 Probabilities for Quebec 160

B.4 Probabilities for Nova Scotia 161

List of Abbreviations

CC Climate Change

GCM Generalized Circulation Model

CMIP Coupled Model Inter-Comparison Project

RCP Representative Concentration Pathway

SSP Shared Socio-Economic Pathway

ECCC Environment and Climate Change, Canada

CDF Cumulative Distribution Function

PMF Probability Mass Function

HPP Homogeneous Poisson Process

NHPP Non-Homogeneous Poisson Process

EVA Extreme Value Analysis

EVD Extreme Value Distribution

MVD Maximum Value Distribution

MLE Maximum Likelihood Estimation

MVF Mean Value Function

HW Heatwave

NS Non-Stationary

RP Return Period

MWT Mean Waiting Time

MCS Monte Carlo Simulation

MTP Markov Transition Probabilities

CS Condition State

List of Symbols

$E[.]$ Expectation: The expectation of a random variable or a random process

$P[.]$ Probability: Probability of the event given in [.]

$\lambda(t)$ Rate Function: Time dependent rate function of a Non-Homogeneous Poisson process

$F_X(x)$ Cumulative Distribution Function (CDF): Cumulative Distribution of the random variable X

$f_X(x)$ Density: Probability Density Function of the random variable X

Chapter 1

Climate Change in Canada: Overview

1.1 Introduction

The Earth's climate has undergone natural fluctuations over geological timescales, but anthropogenic activities have significantly accelerated this process, posing a profound threat to the environment. The consequences of human-induced climate change (CC) are far-reaching, impacting various meteorological variables worldwide, with significant implications for ecosystems, human health, and the economy.

The release of massive amounts of greenhouse gases (GHGs) from industrial activities, transportation sectors, and land-use changes has led to a steady increase in the Earth's average temperature. This temperature increase manifests in extreme climate variations across different geographic locations, depending on local topography and meteorological conditions, resulting in altered precipitation patterns, sea-level rise, and more frequent and intense weather events.

In recent decades, the frequency and severity of natural hazards such as hurricanes, droughts, wildfires, and heatwaves have increased, with devastating impacts on human settlements, infrastructure, and ecosystems. These changes are attributed to CC, highlighting

the urgent need for effective mitigation and adaptation strategies.

This chapter presents an overview of the latest simulations from global climate models and a review of recent literature to discuss projections of key environmental variables such as temperature, wind speed, and precipitation. However, before diving into that, let us briefly understand the working of the climate models and the different kind of forcing incorporated to derive the predictions of these climate variables in the future.

1.2 Climate Models

Climate models or the General Circulation Models (GCMs) are computer simulations that uses a mathematical framework to predict future climate conditions based on different physical processes [77]. They discritize the Earth's surface into a three-dimensional grid of cells, with resolution depending on cell size and time steps ranging from minutes to years. This discretized domain is subjected all kinds of known physical processes to simulate the path of all weather variables such as air temperature, precipitation, and humidity.

These models are used to generate ensemble of paths by varying the initial conditions and the other forcings. Therefore, these future simulated climate variables contain a number of uncertainties in their predictions, as discussed next.

1.3 Uncertainties in Climate modeling

1.3.1 Sources of uncertainties

The climate model projections are subject to several sources of uncertainties of which some of them are attributed to the lack of knowledge i.e. the epistemic uncertainties and others due to the inherent stochasticity of the weather processes i.e. aleatory. Some of the sources of uncertainty are listed as follows:

- Uncertainty attributed to the lack of complete understanding of governing physical processes resulting in modelling errors. Some examples include:

  - Formation, distribution and effects of other processes on cloud formations;
  - Uncertainties in the Carbon cycle and how it will be effected in the future climatic scenarios;
  - Lack of understanding of ice-sheet models and hence different models would predict different sea level rise.

- Uncertainty may arise from variations in analysis methods as well, such as
  - Selection of numerical propagation methods;
  - Variation in the parameterization processes;
  - Resolution of small-scale processes compared to larger scales .

- Uncertainties arising from the possible future emission scenarios considered in climate projections. These scenarios depend on factors such as future population levels, social and economic development pathways, and government policy decisions. Climate models can exhibit large differences under various emission scenarios, leading to uncertainty in projections.

- Uncertainties also stem from the internal variability of the system and is represented by the natural disturbances in the climate system that occur without external influences, such as radiative forcing. For example, internal variability arising from natural climate oscillations includes the El Nio South Oscillation, the North Atlantic Oscillation, and the Pacific Decadal Oscillation.

Climate models may capture the broad-scale behavior of these oscillations, but predicting exact timing and magnitude is always a challenge. This internal variability can contribute to the uncertainty in climate projections, especially in the short term [129]. The climatic systems have an inherent chaos arising from its highly non-linear behavior that may manifest itself in abrupt changes resulting from small changes in radiative forcing [44, 6].

In addition, other weather processes like the heatwaves or hurricanes have inherent randomness in their arrival and intensities. In these cases, climate models may be able to simulate the probability distributions of these events, but will not be able to predict their occurrence in the long run.

1.3.2 Tackling the uncertainties

There are several approaches to dealing with the uncertainties described in the last section. Although it is impossible to fully account for the uncertainties in the prediction, a number of approaches are often implemented to reduce the uncertainties to a manageable extent, some of which are listed below.

1. **Bias Correction:** The validity of these models is tested through something called ***"hind-casting"*** [88, 23], in which the models are used to obtain the path of weather variables in the historical time-period. Bias correction is applied to the model outputs to match the reference datasets and hence have more confidence in the future projections.

2. **Model Weighting:** Results of some models are closer to the reference datasets giving more accurate hind-casting, and hence while model averaging of the results more weightage is given to those models than the others.

3. **Model Evaluation:** Sometimes only the models with good accuracy in the hind-casting are selected for analysis from a given ensemble to reduce the uncertainty.

Once validated, they project future climate scenarios based on Representative Concentration Pathways (RCPs) or Shared Socio-economic Pathways (SSP), which describe possible future conditions based on greenhouse gas levels in 2100.

1.4 Coupled Model Intercomparison Project (CMIP)

The Coupled Model Intercomparison Project (CMIP) is a joint effort by climate researchers and organizations to understand climate change in the past, present, and future [30]. It uses multiple models to study how natural changes and human activities affect the climate. CMIP runs experiments to predict future climate changes and explores how well we can predict climate changes at different times and places. It also compares the results of different models to understand their differences.

CMIP started in 1995 as a way to compare climate models. Initially, it focused on simple scenarios, such as a steady increase in CO2. Over time, it has evolved to include more complex scenarios, such as historical and future climate changes. CMIP manages large amounts of data, with help from organizations like the US Department of Energy, and collaborates with other groups to improve climate modeling. The project is led by the CMIP Panel and the Working Group on Coupled Modelling (WGCM) Infrastructure Panel (WIP), which coordinates model comparisons and develops infrastructure for data sharing.

CMIP has gone through several phases, each building on the previous one with new and improved simulations. The latest phases, CMIP5 and CMIP6, are the most recent developments in this effort.

1.4.1 CMIP(Phase 5)

The CMIP5 project represents a significant advancement in climate research, building on its predecessors CMIP3 and CMIP4 to provide a comprehensive dataset to study climate variability and change [113]. In this model intercomparison project, multiple modeling groups and incorporating feedback from various stakeholders were involved from all over the globe to enhance the understanding of climate processes and improve model performance. In this phase of assessment, the climate projections provided, were based on the Representative Concentration Pathway (RCP) scenarios [79] which are pathways of different extent of radiative forcings defined as follows.

- **RCP2.6**: Peak in radiative forcing at approximately 3 W/m2 mid-century before declining to 2.6 W/m2 by 2100.
- **RCP4.5**: Stabilization in radiative forcing at 4.5 W/m2 post 2100.
- **RCP6.0**: Stabilization in radiative forcing at 6 W/m2 post 2100.
- **RCP8.5**: Rise in radiative forcing to 8.5 W/m2 in 2100.

The extensive dataset generated by CMIP5 allows for the exploration of model differences, climate predictability, and the impacts of various climate scenarios. Through collaboration with the broader climate research community and coordination by the World Climate Research Programme, CMIP5 serves as a valuable resource for scientists studying climate dynamics, informing key scientific assessments such as the IPCC reports, and addressing fundamental questions about climate and CC.

1.4.2 CMIP (Phase 6)

This development over CMIP5 in the multimodel ensemble projections was based on Shared Socio-economic Pathways (SSP) which describes socioeconomic conditions, land use, and other anthropogenic climate-driven greenhouse gas emissions.

Not only do SSP scenarios provide socioeconomic characteristics in a standardized manner, that is, SSP based scenarios correlate societal changes such as population, education and governmental policies related to CC mitigation, and hence lead to possible mitigation measures depending on the pathway [29].

Ultimately, the two main strategies to combat CC have boiled down to mitigation and adaptation in a broad sense, depending on which the SSP scenarios are classified.

Mitigation refers to taking actions to reduce anthropogenic interactions to CC which comes through reduction in emissions of GHGs and hence reducing the heat-trapping in the atmosphere.

Whereas, **adaptation** refers to the situation to make the best out of the changing scenario and also to taking precautionary measures to survive the increased adversities led by climate, for example investing and building flood-proof infrastructures, considering higher design floods for bridges, etc.

These several SSP scenarios with extent of challenges in mitigation and adaptation are described as follows [78].

- **SSP1:** Sustainability – Taking the Green Road (Low challenges to mitigation and adaptation)

- **SSP2:** Middle of the Road (Medium challenges to mitigation and adaptation)
- **SSP3:** Regional Rivalry – A Rocky Road (High challenges to mitigation and adaptation)
- **SSP4:** Inequality – A Road Divided (Low challenges to mitigation, high challenges to adaptation)
- **SSP5:** Fossil-fueled Development – Taking the Highway (High challenges to mitigation, low challenges to adaptation)

These SSPs are used to decide on the emission scenario i.e. the RCP scenario, depending on the adaptation or mitigation strategies, which is then used to run the simulations on the GCMs. However, the relations between SSPs and RCPs are not that simple. For example, SSP1 can have different emissions scenarios such as RCP 1.9 and 2.6 depending on the mitigation actions taken; hence, the model outputs are usually denoted in CMIP6 using both the SSP and RCP scenarios together, i.e. SSP1(1.9) and SSP1(2.6).

Of all the SSP scenarios linked to their RCP scenarios, it is found that the SSP5(RCP8.5) will result in the highest increase in the global temperatures over the years, which is why several analyses conducted in this thesis are only performed for this worst case scenario.

1.5 Weather variables

The output of the climate models are given in the form of gridded time series data of various weather variables. Depending upon the analysis, the spatial and temporal ranges of the data can be used, or as need may arise the data might require spatial downscaling using several downscaling methods available. The uncertainty in the results of various weather variables are different and depending on the extent of uncertainty they are categorized in several tiers. The various tiers of variables are described as follows [15].

1. **Tier-1**: The tier 1 variables are those that can be projected into the future with maximum confidence for given global warming levels, due to the high level of confidence in the underlying physical processes involved in the climate models. This

also implies that the change factors or the percentage changes projected for these variables can be directly used for new designs and if there exists other sources of uncertainties, they can be quantified with high confidence. Some examples of tier-1 variables include the heating degree days, hourly temperatures, daily maximum, and minimum temperatures.

2. **Tier-2**: This classification represents a medium level of confidence in the physical processes that are used to project these variables in the future, and as such these changes may need to be supplemented by additional evidence. But, even then there might be inconsistencies in the results resulting in lower confidence in the projections over the future. In such a situation, these variables are suitable for risk analysis or studying uncertainty with design. Some examples of tier 2 variables include annual total precipitation and rainfall, and other extreme values associated to rainfall.

3. **Tier-3**: This classification indicates lowest confidence in the projections arising from the poor understanding of the physical processes used in the model. The projected changes in these variables are suitable for structural reliability studies in different climate scenarios. Examples of these variables include annual mean humidity, hourly wind pressures, ice accretion, and snow loads.

In the following sections, the effect of various global warming levels on some key weather variables are discussed.

1.6 Ambient temperature

The temperature change is the most direct consequence of global warming, and it is observed that there has been an increase in temperature to the extent of 1.6 degrees Celsius in the mean annual temperature of Canada during the period 1948 to 2016 [15].

For the RCP8.5 emission scenario, there is a possibility of up to 6.3 $^{\circ}C$ in the mean temperature of Canada by the year 2100.

For the near future, that is, by approximately 2050, the temperature of Canada can increase by 1.5$^{\circ}C$ (low emission, RCP2.6) to the extent of 2.3$^{\circ}C$ (high emission, RCP8.5)

relative to the period 1986-2005, with greater effects expected to be experienced in the winters of northern Canada [12].

In Fig(1.1) shows the magnification in the increments of annual averages of maximum temperature and the minimum temperatures with respect to the global temperature increments, putting greater strain on Canada's policy makers mitigation and adaptation measures.

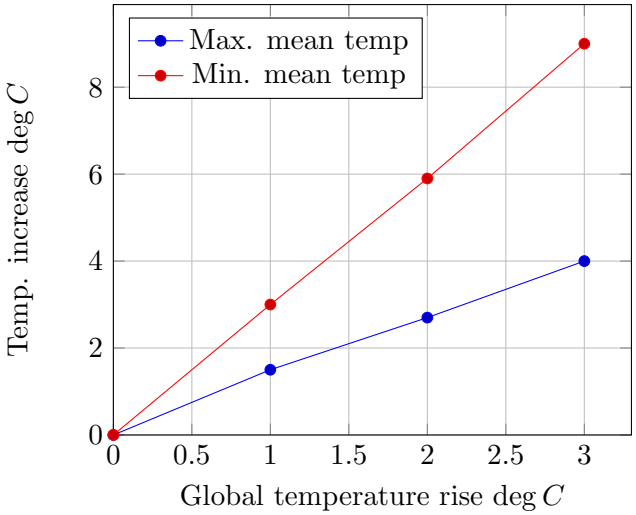


Figure 1.1: Increase in mean temperatures of Canada due to Global rise in temperature[15].

Let us also discuss the effects of CC briefly on the Tier-2 variables, that is, the variables which are dependent on the Tier-1 variable like temperature but are subjected to higher levels of uncertainty in their prediction. The following section discusses the effect of CC on precipitation and rainfall.

1.7 Precipitation and rainfall

From a water infrastructure design point of view, the study of precipitation changes is crucial when dealing with flood risk, rainfall-induced landslides, bridge designs, snow loads, and the design of drainage systems in cities and towns.

Since changes in precipitation and rainfall are secondary effects of global warming, uncertainties in the prediction of changes can be greater[15]. However, with much confidence, it is predicted that there will be a substantial increase in mean annual precipitation and rainfall.

Based on a national average, it was found that, during the period 1948-2012, there has been an increase in the annual precipitation of Canada of approximately 18.3%, with the highest effect in northern Canada ($\sim 32\%$). The model simulations have predicted a net increase in the mean annual precipitation of 7.3% by 2050 and up to the extent of 24.2% by the end of this century for RCP8.5, which is the scenario of high emissions.

When it comes to extreme precipitation events, the simulations predict a decrease in the recurrence times for the events corresponding to all return periods. In other words, the frequency of precipitation events corresponding to any intensity/magnitude is likely to increase in the coming years.

For example, under the high emission scenario, precipitations with a return period of 50 years at present can decrease to the extent of 10 years by 2100, which is alarming from the design considerations of most structures that are constructed and intended to be in service beyond this period of time [12]. The report recommends that, for the purpose of design, one may consider an increase in the intensity of one-day rainfall events with a return period of 50 years to increase following the Clausius-Clapeyron condition. The Clausius-Clapeyron relation suggests that with an increase in local temperature there is supposed to be an increase in the moisture content of the atmosphere to approximately $7\%/^{\circ}C$.

There are several other studies as well that suggest with conviction that there will be an increase in intensity and frequency of precipitation and rainfall in the coming years. In [87], the simulation results suggest that the Intensity-Duration-Frequency curve lower bounds for the 100-year return period short-duration rainfall events, in around 2050, will be around 35% higher than the current government IDF curves for the City of London in Ontario.

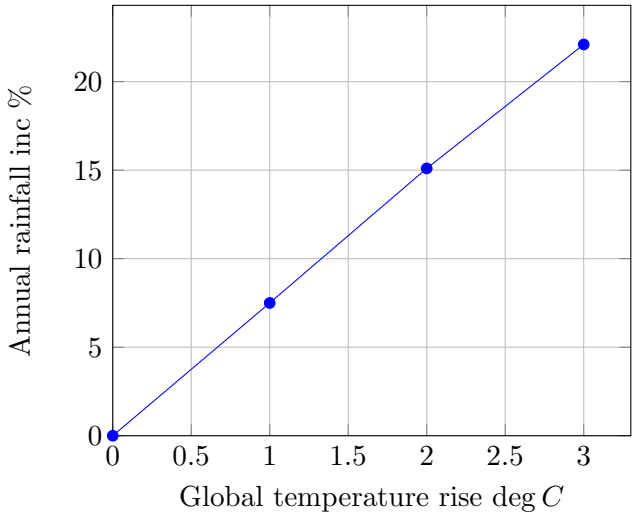


Figure 1.2: Percentage increase in annual rainfall as a function of the global temperature rise[15]

Figure 1.2), shows that a 3.5° rise in global temperature can result in an increase of 25% in annual rainfall in Canada which would also roughly correspond to the Clausius-Clapeyron condition.

1.8 Wind pressures

Although, this variable has not been analysed in this thesis, but for the sake of completing the discussion on the effects of key weather variables, a brief discussion on the effect of global warming on wind is included here. For the design of important infrastructural systems, such as tall buildings, bridges, and calamity shelters, design against wind loading is of utmost importance. The design of roofing in large industrial shades also requires information on wind loading in their design. In addition to that, in regions more prone to tornadoes or cyclones, wind loading is an important consideration in the design and reliability analysis of the system.

The wind pressure effects are an indirect consequence of global warming and since design wind pressures are treated as Tier-3 variables because of their dependence on Tier-1

and 2 meteorological variables and result in the highest uncertainties in their prediction [15].

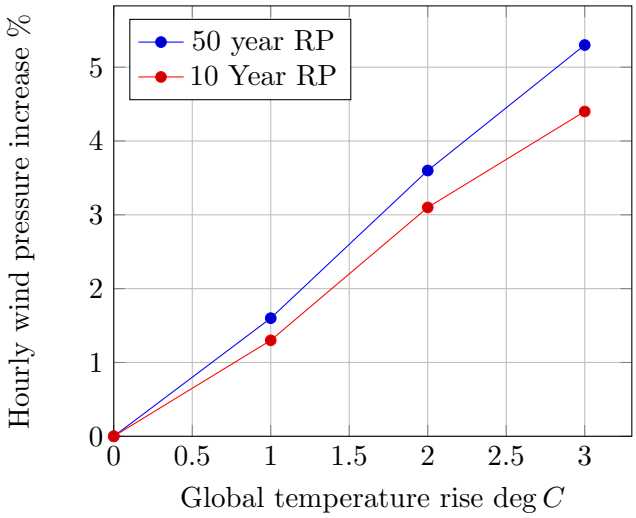


Figure 1.3: The percentage increase in hourly wind pressures for 50-year and 10-year return period, as a function of the global temperature rise[15]

Nonetheless, there is a suspected increase in wind pressures in the future years as a result of CC with significant regional variability, although, the changes in the extreme wind pressures with an increase in global temperatures are not as significant compared to changes in the other weather variables as depicted in Figure 1.3.

1.9 Research Objectives

This study has explored various implications of climate change from various perspectives that includes modelling the non-stationary climate-driven hazards, the impacts of climate change on concrete degradation, and economic risk estimation due to these kind of hazards.

The research objectives can be summarized as follows.

- To propose a non-stationary stochastic process model to estimate the maximum value distribution of hazard events that are influenced by climate change and hence

aid time-dependent reliability calculations in infrastructure design. In that context, the challenges of using the traditional stationary models and other extreme value distribution models are also discussed which serves as a motivation for this study.

- To apply and demonstrate the usage of these models by analyzing the projected weather data from the CMIP6 multi-model ensemble and discuss the critical concepts like extreme value distribution and return periods in the non-stationary context. Specifically, the extreme precipitation and the heat wave events were analyzed in the demonstration.

- Not only will the hazard processes but the degradation processes are expected to accelerate due to harsher environmental conditions with increased temperatures and relative humidity. Therefore, the next objective is to study the effect of climate change on concrete degradation processes, specifically for bridges by simulating the physico-chemical degradation processes in the changing climatic conditions, and estimating the equivalent Markov transition probabilities for bridge condition states.

- Another important aspect of optimal design is the economic risk assessment and due to the changing load patterns, accompanied with faster degradation, the economic risk is going to be affected. Therefore, for a comprehensive overview of the implications of climate change, the final objective is to derive the various moments and distribution of non-stationary compound stochastic processes and use them to estimate the economic risk due to the climate-driven hazards over any given period.

1.10 Thesis organization

The various objectives of this study are organized to maintain the flow of discussion as suggested in the last section. Chapter 2 begins with the discussion about the basic concepts of stationary and non-stationary hazard modelling and various methods of obtaining the extreme value distributions for a given hazard processes. The chapter provides the necessary definitions and formulations of the non-stationary stochastic process hazard models

and demonstrates the applicability of the stochastic process models over the traditional extreme value models that come from asymptotic assumptions.

The proposed methods were demonstrated using a case study involving extreme precipitation events in changing climate, using the CMIP6 multi-model ensemble data in Chapter 3. Another case study involving heat waves was considered in Chapter 4 to further demonstrate the applicability of these models for hazards which are not that frequent and hence challenge the asymptotic assumptions but can be suitably modelled by the stochastic process models.

Chapter 5 covers the second aspect of the thesis which is studying the effect of climate change on concrete degradation, more specifically concrete bridges.

The final aspect of the thesis, that is, the estimation of the economic risk due to hazards influenced by climate change, is presented in Chapter 6.

1.11 Conclusions

.

The atmosphere of the Earth has heated up by around 1.6° Celsius in the period 1948 to 2016 due to natural and anthropogenic causes. This has raised concerns in the engineering community since the changing climate has resulted in an intensification of several climate-driven hazards such as flash floods, thunderstorms, tornadoes, and droughts, depending on the geographical location. This gradual intensification is concerning for the reliability of the infrastructure systems that are expected to witness frequent calamities within their design life.

This has led to thorough and ongoing experimentation on climate models or GCMs, which are mathematical models of the various physical processes that occur around the globe, developed by several climate agencies. The GCMs are subjected to varying levels of radiative forcing simulating different levels of global warming, and predictions of several weather variables are obtained for the past and future. Since the level of global warming depends on the emission of greenhouse gases (GHGs) by human activities, depending on

the levels of mitigation and adaptation measures, several pathways of radiative forcing may be expected, giving rise to different probable scenarios in the future.

The model outputs from different reporting institutes were brought together in a project for comparison called the Coupled Model Intercomparison Project (CMIP) in 1995 and since then, there have been different phases in the project, each building up on the earlier phases. In this context, the 5th and 6th phases of CMIP, which are the two of the most recent phases and their salient features are discussed in this chapter. In addition, the effect of global warming and changing climate on temperature, precipitation, and wind speed is discussed.

The changing climate will manifest itself in an increase in frequency and intensity of hazards, and hence it is important to consider its expected ramifications on infrastructure systems in the future. Some of the typical manifestations might be in the form of increased energy loads to cool buildings due to more frequent heat events, faster degradation of construction materials due to increased temperature and humidity and hence lowering the design life of the structures, increased flows in water infrastructure systems due to increased precipitation, increased wind loads on tall structures.

Chapter 2

Non-Stationary Probabilistic Analysis of Extremes

2.1 Introduction

Engineering systems are designed on the basis of extreme loading conditions. Mostly, annual extreme value distributions are obtained by fitting the annual maxima data of the concerned hazard process and used to calculate the annual probability of failure.

So, let us begin with the discussion on the extreme value theory. We will discuss the theory in its widely used stationary context and then the non-stationary generalizations and the limitations associated with these generalizations. Later, citing several challenges in the theory, we will introduce the stochastic process model of hazard processes, which can provide a more comprehensive overview of the changes in the underlying hazard processes in the non-stationary context.

2.2 Extreme Value Theory

2.2.1 Stationary Extreme Value Distribution (EVD)

Let us define a random sequence $\{X_1, ..., X_n\}$, where $X_i's$ are independent and identically distributed (IID) with a common distribution $F_{X_i}(x)$. Then the extreme value (here maxima) is given by random variable, $X_{max} = Max\{X_1, ..., X_n\}$,

$$\begin{aligned} &P[X_{max}(n) \leq x] = P[X_1 \leq x_1, ..., X_n \leq x_n] \\ \Rightarrow &F_{X_{max}}(x) = [F_{X_i}(x)]^n \end{aligned} \tag{2.1}$$

If $n \to \infty$,an asymptotic limit is derived as the generalized extreme value or the GEV distribution [22].

$$F_{X_{max}}(x) = exp\left[-\left(1+\xi\left(\frac{x-\mu}{\sigma}\right)\right)^{-1/\xi}\right], \left(1+\xi\left(\frac{x-\mu}{\sigma}\right)\right) > 0 \tag{2.2}$$

where, ξ, μ and σ are the distribution parameters, called the shape, location and the scale parameter, respectively.

The parameter, ξ has information regarding the tail characteristics of the distribution and depending on the value of this parameter, three different classes of EVDs can be defined,

- $\xi \to 0$: Leads to Gumbel EVD as a limiting form of the GEV as follows, having exponential tails
$$G(x) = exp\left[-exp\left(-\frac{x-\mu}{\sigma}\right)\right] \tag{2.3}$$
- $\xi > 0$: Frechet EVD having thick tails
- $\xi < 0$: Weibull EVD having short tails with finite endpoints.

However, these extreme value distributions have some drawbacks from a statistical point of view. Since this is a block maxima method i.e. only the maximum value of the

events in a given year are used, without giving any importance to other events which may have significantly high impacts, leading to the under-utilization of the data.

To avoid this limitation, some other models were developed such as the Generalized Pareto distributions discussed briefly as follows.

Generalized Pareto Distribution (GPD) For an arbitrary sequence $\{X_1, ..., X_n\}$, for which the maximum value distribution follows a GEV as given in Equation (2.2), for a sufficiently large value of l_0, the distribution of X, an element in that sequence $\{X_i\}$, conditioned on the event $X > l_0$, can be approximated by the Generalized Pareto Distribution [22].

$$H(x) = P[X < x | X > l_o] = 1 - \left(1 + \frac{\xi(x - l_0)}{\sigma + \xi(l_0 - \mu)}\right)^{-1/\xi} \tag{2.4}$$

in which, $x > l_0$ and $\left(1 + \frac{\xi(x-l_0)}{\sigma+\xi(l_0-\mu)}\right) > 0$.

Similar to GEV, the shape parameter ξ influences the tail characteristics of the distribution. However, in GPD models, even the selection of the threshold value (l_0) is ambiguous and arbitrary, since, selecting a lower threshold will not satisfy the asymptotic assumption of the model and choosing a very high threshold will not leave sufficient events crossing the threshold for the model fitting, and hence again lead to the under-utilization of the data.

2.2.1.1 Return periods

This is related to a geometric stochastic process. If the GEVD parameters are estimated for the annual extreme values of a hazard process, then we can calculate the annual probability of exceedance (POE) of the magnitude of the hazard over a given level. Suppose, the POE is denoted as p and the corresponding level is x_0, then, if we define a random variable T denoting the year when the hazard event first crosses the level x_0. The distribution of T is given by the geometric distribution with the parameter p as follows.

$$f_T(i) = P[T = i] = (1 - p)^{i-1}p, \quad i \in \{1, 2, 3...\} \tag{2.5}$$

The expected value of this time T is defined as the return period (RP).

$$E[T] = \sum_{i=1}^{\infty} i(1-p)^{i-1}p = \frac{1}{p} \tag{2.6}$$

These models are not suitable under non-stationary conditions.

2.2.2 Non-stationary EVD

To account for non-stationary effects, the constant parameters of the Gumbel or GEV distribution are replaced by time-dependent functions[83, 71, 21, 119].

For the non-stationary Gumbel distribution, the location and the scale parameters are now considered to be functions of time [22].

$$G(x;t) = exp\left[-exp\left(-\frac{x-\mu(t)}{\sigma(t)}\right)\right] \tag{2.7}$$

For example, these parameters can be linear function of time.

$$\mu(t) = \mu_0 + \mu_1 t \tag{2.8}$$

$$\sigma(t) = \sigma_0 + \sigma_1 t \tag{2.9}$$

Parameter estimation is based on Maximum Likelihood Estimation (MLE). The confidence intervals of these parameters can be obtained using the Bootstrapping methods.

The parameters μ_1 and σ_1 are coefficients of time in Equation (2.9), and upon estimation if they are found to be statistically significant, it can be concluded that there is a non-stationarity in the underlying process. However, if these parameters are not found to be significant, then there could be two possible conclusions, i.e. there is no time dependence and the process is stationary or there could be other kind of nonlinear temporal relationships in the data, which can be decided upon further investigation of the data.

This method can be easily extended for other kind EVD models, for example, for Pareto distributions, a time-dependent threshold can be utilized to represent the changing

conditions, and in the case of a GEV, the shape parameter can be also considered to be time-dependent [81].

2.2.2.1 Return period

In this case the annual POE of a hazard is also a function of time, which we can denote as $p(i)$ as the POE of a return level x_0 in the year i,

$$p(i) = P[X_{max}(i) > x_0] \tag{2.10}$$

where, $X_{max}(i)$ denotes the annual maximum value corresponding to the ith year. Therefore, following a similar framework for the definition of the return period, we can assign probabilities to the values attained by the random variable T denoting the time of first occurrence of the event [97].

$$f_T(i) = P[T = i] = p(i)\prod_{t=1}^{i-1}(1 - p(t)), \quad i \in \{1, 2, 3...\} \tag{2.11}$$

Again, using similar argument, the expected value of T can be considered to be the return period given as follows:

$$E[T] = \sum_{i=1}^{\infty} ip(i)\prod_{t=1}^{i-1}(1 - p(t)) \tag{2.12}$$

This sum can be taken for sufficiently large number of terms at which the value of the return period converges.

In the context of climate change modelling, assessment of changes in the frequency and intensity of extreme events is a topic of primary interest. In the NS Gumbel model, this assessment is made in a somewhat indirect manner.

The change in the frequency is estimated by evaluating change in the return period of an extreme event of interest. For example, total daily rain fall exceeding 40 mm, $x = 40$, is an event of interest. The return period in a future year, t, is approximately defined as

a reciprocal of probability of exceeding this level in the t^{th} year as (REF)

$$T(t,x) = \frac{1}{1 - F_{max}(x,t)} \tag{2.13}$$

The change in frequency is thus signified in terms of the difference in the stationary return period and that given by above equation.

It should be noted that this expression is just an approximation that is based on the assumption that the probability of exceedance in every year from t onward, i.e., $t, t+1, t+2, \ldots, \infty$, is constant and equal to $(1 - F_{max}(x,t))$. However, this assumption is untenable in a non-stationary climate.

The change in intensity is signified in terms of change in the probability of exceeding a threshold with time. For example, change in the probability of exceeding a threshold, such as $x = 40$ mm can be estimated over time as, $1 - F_{max}(40,t)$. The change in this probability as compared to that estimated under the assumption of stationary climate has been used as a measure of change in intensity.

A general observation is that NS Gumbel model provides indirect measures of changes in the frequency and intensity of extreme events. This limitation can be overcome by the use of a non-stationary stochastic model, as discussed in the next Section It must be noted that in the non-stationary scenario, the return period definition applies only to the first arrival of the event, and there is no way to obtain the return period as the mean interarrival time for recurring events.

2.2.3 Limitations of NS EVD models

Some limitations associated to the GEV models can be specified as

- Although stationary versions of the model can be manipulated to accommodate the gradual changes, the definitions of the return period cannot be used for recurring events and are only applicable to the time of first arrival.

- The GEV models provide no information about the underlying hazard process apart from the changes in the extreme value distribution. It is impossible to identify if the changes in the extreme value is due to changes in frequency or intensity of the individual events, leading to a lack of specificity.

These limitations can be addressed by using a stochastic process model, which can capture the information regarding the arrival of the events and their magnitude, and hence provide a complete description of the process. Therefore, several aspects of a stochastic hazard process have been explored in the following sections.

2.3 Stochastic process model

An environmental hazard can be modelled as a stochastic shock process model [82]. A stochastic shock process model is characterized by a stochastic arrival process which is usually a point process and the shocks associated with each of the arrivals. Figure 2.1 demonstrates a stochastic process, in which the sequence of random variables $\{S_i\}$ denotes the arrival times of the hazard events and the process $\{X_i\}$ denotes the respective shock heights.

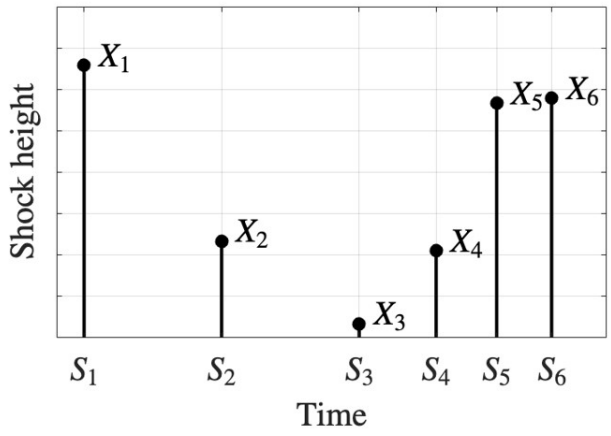


Figure 2.1: Stochastic process

The Poisson shock process is widely used in stationary reliability analysis.

2.3.1 Stationary Poisson process

Stationary or homogeneous Poisson process (HPP) is characterized by inter-arrival times, T_i, expressed as the difference of the arrival times, $S_i's$, is distributed as IID Exponential.

$$T_i = S_i - S_{i-1}, \quad i = 1, 2, ... \tag{2.14}$$

Therefore, the arrival times $S_i's$ given as [94],

$$S_n = \sum_{i=1}^{n} T_i \tag{2.15}$$

follows a Gamma distributed with the following parameters.

$$S_n \sim Gamma(n, \lambda) \tag{2.16}$$

The joint density of the arrival times conditioned on the number of events until t is given as:

$$f_{S_1,...,S_n|N(t)}(s_1, ..., s_n|N(t) = n) = n!\frac{1}{t^n} \tag{2.17}$$

In the above equation it can be seen, that in a time constrained situation, the joint density of arrival times is independent of the variables $\{s_1, ..., s_n\}$, which follows from the order statistics property followed by the arrival times of the Poisson process.

For further discussion and detailed proofs, the reader is referred to [24, 99].

The distribution of the number of events in a period $(0, t)$ is given as

$$P[N(0, t) = k] = \frac{e^{\lambda t}(\lambda t)^k}{k!} \tag{2.18}$$

The mean value function $\Lambda(0, t) = E[N(0, t)]$ is given as:

$$\Lambda(0, t) = E[N(0, t)] = \lambda t \tag{2.19}$$

The expected number of events per unit time, i.e., rate $\lambda(t)$ is given as

$$\lambda(t) = \frac{d(\Lambda(0, t)}{dt} = \lambda \tag{2.20}$$

The HPP has a constant rate, which signifies the stationary property.

The estimation of the rate parameters in the Poisson process is usually done using

maximum likelihood estimation (MLE) [27] and the ML estimate of the rate is given as:

$$\lambda = \frac{n}{t} \tag{2.21}$$

This expression has been used in several places in the thesis to estimate the rates of hazard process in the stationary base case scenarios. Next we discuss the second component of the shock process which is the shock heights.

2.3.1.1 Shock height distribution

Each of the shock arrivals is associated with some magnitude of the shock height, which of course is uncertain as well, and hence represented as another sequence $\{X_i\}$. For the stationary scenario, this sequence is considered independent of arrival times and IID with a common distribution $F_X(x)$. With the historical data available, this distribution can be easily estimated using any distribution fitting technique like probability paper plotting (PPP), and MLE.

Together, with the arrival times, this conjugated sequence (S_i, X_i), is called the shock or marked process.

2.3.1.2 Thinning Property

Consider a parent HPP, $N(t)$ with rate λ and a probability p to accept a point and hence reject a point with probability $(1-p)$, then we can construct two independent HPPs, one the accepted process, $N_1(t)$ with rate λp and a rejected process, $N_2(t)$ with rate $\lambda(1-p)$ [99].

$$N(t) = N_1(t) + N_2(t) \tag{2.22}$$

As a corollary, the HPP can be partitioned into several independent HPPs using some partitioning criteria.

This probability of acceptance of a given event in the parent HPP denoted as p, can be associated with marks process, for example, if we want to isolate the events for which the

shock heights exceeds a value x_0, then p becomes $(1 - F_X(x_0))$ and we will have a process with rate $\lambda(1 - F_X(x_0))$ and its associated marks will be distributed as $F_{X|X>x_0}(x|x > x_0)$

2.3.1.3 Maximum value distribution (MVD)

The distribution of the maximum shock height in $(0, t)$ is given by [82] It may be noted that here, for the stochastic process, we are using the term "maximum value" instead of "extreme value" because we want to keep the latter reserved for maximum value concept stemming from asymptotic extreme value theories.

$$F_{max}(x;t) = exp\left[-\lambda t\left(1 - F_X(x)\right)\right] \tag{2.23}$$

Therefore, with a shear increase in the rate of arrivals the distribution of the maximum shock height in a given interval increases and this is reflected in the maximum value distribution (MVD) corresponding to an HPP in Figure 2.2.

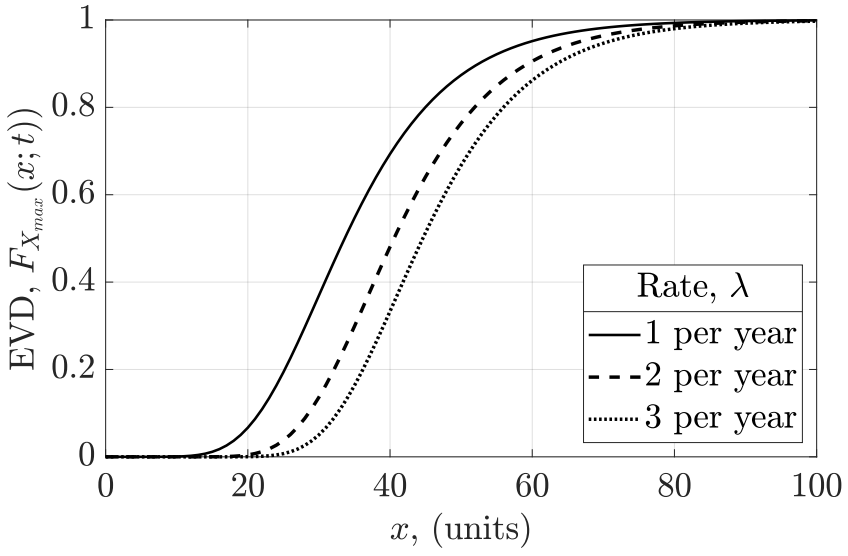


Figure 2.2: Extreme value distribution for an HPP, Parameters: $X_i's \sim Exponential(\ mean = 10\ units), t = 20\ years$

However, in several cases, for reliability analysis, designers are interested in the annual MVD, in which case, we can set $t = 1$ year to have the following.

$$F_{max(A)}(x) = exp\left[-\lambda\left(1 - F_X(x)\right)\right] \tag{2.24}$$

2.3.1.4 Return periods

In case of a stochastic process, $E[T_1],\ E[T_2], ...,\ E[T_n]$ can be considered to the first, second, and nth mean inter-arrival times or return periods. For an HPP,

$$E[T_1] = \ E[T_2] = ... = \ E[T_n] = 1/\lambda \tag{2.25}$$

Therefore, we have discussed several aspects of the Poisson process in the stationary scenario, and now we will see how these aspects can be extended and generalized for the non-stationary case.

2.3.2 Non-Homogeneous Poisson process (NHPP)

2.3.2.1 Definition

In the non-stationary extension of the HPP, the property that the number of events in a given time-interval is Poisson distributed still holds i.e. for the counting process, $(N(t), t \geq 0)$, increments in time are independent and is Poisson distributed, and the process starts at zero, i.e. $(N(0) = 0)$. The increment in an NHPP for any interval (t_1, t_2) is Poisson distributed (Equation (2.26)).

$$P(N(t_1 + t_2) - N(t_1) = n) = \frac{[\Lambda(t_1, t_2)]^n e^{\Lambda(t_1,t_2)}}{n!}, \quad t_2 > t_1 \tag{2.26}$$

in which $\Lambda(t_1, t_2)$ is the mean value function.

The modelling of non-stationary environmental loads by NHPP was extensively discussed in [82] where several useful properties of NHPP were derived and compiled from the literature.

NHPP can also be defined using an equivalent definition provided in [94] and given as follows:

NHPP is a counting process $(N(t), t \geq 0)$, with a rate function $\lambda(t)$, if the following holds .

1. $N(0) = 0$
2. Increments in $N(t)$ are independent.
3. $P[N(t+h) - N(t) \geq 2] = O(h)$
4. $P[N(t+h) - N(t) = 1] = \lambda(t)h + O(h)$
5. And indentically, $P[N(t+h) - N(t) = 0] = 1 - \lambda(t)h + O(h)$

where, $O(h)$ is defined as a function for which $\lim_{h\to 0} \frac{O(h)}{h} = 0$, that is $O(h)$ approaches 0 faster than h in the limiting condition. This second definition will deem to be more useful for deriving the expression of risk in non-stationary climate as discussed in Chapter 6.

The function $\Lambda(0,t) = E[N(0,t)]$ or simply $\Lambda(t)$ in Equation (2.27) is called the mean value function (MVF) for the NHPP, and, the mean number of events in that interval can be given in terms of the mean value function as:

$$\Lambda(t_1, t_2) = \Lambda(0, t_2) - \Lambda(0, t_1) = \Lambda(t_2) - \Lambda(t_1) \tag{2.27}$$

The time derivative of the MVF gives the rate function of the NHPP (Equation (2.28).) as follows:

$$\frac{d\Lambda(t)}{dt} = \lambda(t) \tag{2.28}$$

However, if the rate function, $\lambda(t)$ is supplied, then the MVF can be obtained by taking the anti-derivative as follows:

$$\Lambda(t_1, t_2) = \int_{t_1}^{t_2} \lambda(s) ds \tag{2.29}$$

The rate function, $\lambda(t)$ can take several forms, however one of the most generalized forms is the exponential-polynomial-trigonometric function (EPTF) proposed in [60] as

follows, where $\alpha_i's$, γ, ψ and m are coefficients and parameters of the function.

$$\lambda(t) = exp\left[\sum_{i=0}^{m} \alpha_i t^i + \gamma sin(\omega t + \psi)\right] \tag{2.30}$$

2.3.2.2 Thinning property

If $N(t)$ is a Poisson process with rate function $\lambda(t)$, and a point at an instant of time s, is retained with a probability $p(s)$, or deleted with a probability $(1 - p(s))$, then the retained and deleted processes are independent Poisson processes $N_R(t_1, t_2)$ and $N_D(t_1, t_2)$ [99]. The rate functions of the processes are $\lambda_R(t)$ and $\lambda_D(t)$, respectively, with the mean value functions $\Lambda_R(t_1, t_2)$ and $\Lambda_D(t_1, t_2)$ given below.

$$\Lambda_R(t_1, t_2) = \int_{t_1}^{t_2} \lambda_R(s)ds = \int_{t_1}^{t_2} p(s)\lambda(s)ds \tag{2.31}$$

and

$$\Lambda_D(t_1, t_2) = \int_{t_1}^{t_2} \lambda_D(s)ds = \int_{t_1}^{t_2} (1 - p(s))\lambda(s)ds \tag{2.32}$$

2.3.2.3 Arrival time distribution

The order statistics property for an NHPP, states that the joint density of the arrival times conditioned on numer of events until t, i.e. $N(t) = n$, is same the joint density of the ordered set of n random variables drawn from a common distribution given by $f_S(s) = \lambda(s)/\Lambda(t)$, i.e. the joint density of the arrival times is given as follows:

$$f_{S_1,...,S_n|N(t)=n}(s_1, ..., s_n|N(t) = n) = n! \prod_{i=1}^{n} \lambda(s_i)/\Lambda(t) \tag{2.33}$$

The marginal distribution of the arrival times of an NHPP can be obtained as follows [82]:

$$F_{S_n}(t) = P[S_n \leq t] = P[N(t) \geq n] = \sum_{k=n}^{\infty} P[N(t) = k] \tag{2.34}$$

The marginal density of the arrival times can be deduced by taking the derivative of the above expression and simplifying it.

$$f_{S_n}(t) = \frac{(\Lambda(t))^{n-1}}{(n-1)!}\lambda(t)e^{-\Lambda(t)} \tag{2.35}$$

This expression is useful in determining the distribution of the inter-arrival times, which are equivalent to return periods for a non-stationary process.

2.3.2.4 Shock height distribution

Non-stationary modelling of shock height is proposed as function of the arrival times, $X_i = X_i(S_i)$.

One simple way to represent the time dependence of the shock heights could be as follows[82]:

$$X_i(S_i) = X_{0,i}\phi_1(S_i) + \phi_2(S_i) \tag{2.36}$$

where, $X'_{0,i}s$ are IID with a density function $f_X(x)$, and $\phi_1(.)(\neq 0)$ and $\phi_2(.)$ are time-dependent functions of arrival times that can capture the multiplicative and additive components of shock height intensification. We shall denote the distribution of time-dependent shock height as $F_{X(t)}(x;t)$.

The IID variables $X'_{0,i}s$ can be used to denote some shock heights in a base scenario which is being amplified. The common distribution can be fitted from the historical data of some base period, for example, the pre-industrial period, based on which the comparisons can be made for the future scenarios.

Following the thinning property which is also preserved for the NHPP, the thinned mean value function denoting the mean number of events over a specified interval following a certain criteria can be isolated, for example if we are interested in the events crossing a certain design value x_0, then the thinned NHPP will have a rate as follows:

$$\lambda(x_0, t) = \lambda(t)(1 - F_{X(t)}(x_0; t)) \tag{2.37}$$

and the corresponding MVF of the thinned process can be given as

$$\Lambda(x_0, t_1, t_2) = \int_{t_1}^{t_2} \lambda(s)(1 - F_{X(s)}(x_0; s))ds \tag{2.38}$$

The above equation can be used to predict the mean number of failure events corresponding to a design value x_0 in any interval of time.

2.3.2.5 Maximum value distribution

The maximum value distribution for the NHPP, $F_{Max}(x, t_1, t_2)$, in any given interval of time $(t_1, t_2]$ can be derived as [82]:

$$F_{Max}(x, t_1, t_2) = e^{-\Lambda(x,t_1,t_2)} \tag{2.39}$$

Where, $\Lambda(x, t_1, t_2)$ is the thinned MVF defined in Equation (2.38) and hence can be expanded as follows:

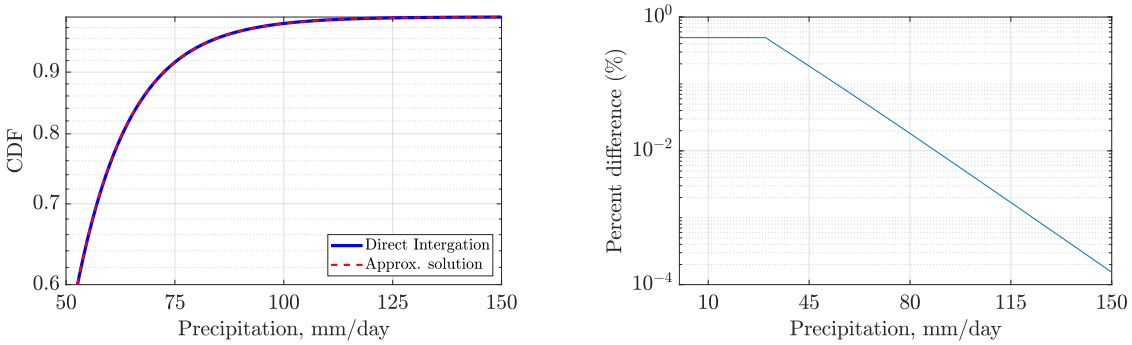
$$F_{max}(x, t_1, t_2) = exp\left[-\int_{t_1}^{t_2} \lambda(t)\left(1 - F_{X(t)}(x; t)\right) dt\right] \tag{2.40}$$

By setting the values of t_1 and t_2 as follows, we can obtain the annual EVD for the NHPP as follows.

$$F_{max}(x, t, t+1) = exp\left[-\int_{t}^{t+1} \lambda(t)\left(1 - F_{X(t)}(x; t)\right) dt\right] \tag{2.41}$$

It can be clearly seen that now, the annual EVD is time-dependent. It may be noted that in general the integrand in Equations (2.40) and (2.42) can often attain non-integrable forms and hence requires numerical integration. However, for the case of annual EVD, since the time-interval is low and the change in the underlying process is slow, we can apply an approximation as follows:

$$F_{max}(x, t, t+1) \approx exp\left[-\lambda(t)\left(1 - F_{X(t)}(x; t)\right)\right] \tag{2.42}$$



(a) EVD-CDF (b) Percentage difference

Figure 2.3: Difference in the NHPP annual extreme value CDF for precipitation obtained using direct integration and approx method for the year 2100 for SSP5(8.5) scenario(detailed discussion in Chapter 3).

The error in this approximation is quite low since, for natural processes, the changes due to climate change is slow and gradual, for example, when the formulations were used for precipitation data (discussed in Chapter 3), it was found that the difference in EVD due to this approximation was less than 1% (see Figure 2.3).

Similar to other attributes of the non-stationary processes, the return periods for a non-stationary process no longer remains constant over time. In the following subsections two prominent definitions of return periods in this context are presented.

2.3.2.6 Return periods

The inter-arrival times, $T_i = S_i - S_{i-1}$, as defined in Equation (2.14), in this case will not be IID due to the non-stationary nature of the process. The distribution of the inter-arrival times can be obtained as shown in [82] :

$$P[T_n > t] = 1 - F_{T_n}(t) = \int_0^\infty f_{T_1}(s+t)\frac{(\Lambda(s))^{n-1}}{(n-1)!}ds \tag{2.43}$$

In the above expression, the fact that $\bar{F_{T_1}}(s+t)$ and $\Lambda(s)$ vanishes at $s \to \infty$ and $s \to 0$

, respectively, has been used.

One formal way of defining the return period can be taken as the mean inter-arrival times $E[T_i]$. It can be understood from the above discussion that the return period is no longer constant. This expected value of the inter-arrival times can be given as Equation (2.44).

$$E[T_n] = \int_0^\infty e^{-\Lambda(s)} \frac{[\Lambda(s)]^{n-1}}{(n-1)!} ds \tag{2.44}$$

When we want to obtain the return periods corresponding to a certain return level x_0, we can simply use the MVF of the thinned process defined in Equation (2.38), in the above expression, i.e.

$$E[T_n(x_0)] = \int_0^\infty e^{-\Lambda(x_0,0,s)} \frac{[\Lambda(x_0,0,s)]^{n-1}}{(n-1)!} ds \tag{2.45}$$

Although, we have formally defined the concept of return period in one way, but in the following section we use a simpler definition of return period which might be more useful in the non-stationary scenario.

2.3.2.7 Mean Waiting Times

For any given time t, the time $W(t)$ till the occurrence of the next event is a quantity of interest and the mean value of this quantity can be considered as another representative definition of the return period. The complementary CDF of the waiting time is given (using the independence of the number of events in disjoint intervals of time) as follows [82].

$$\bar{F_{W(t)}}(s) = 1 - P[W(t) \leq s] = P[W(t) > s] = P[N(t, t+s) = 0] = e^{-\Lambda(t,t+s)} \tag{2.46}$$

Again, for a given return level (or a specified design value) x_0, the mean waiting time can be obtained using the MVF of the thinned process.

$$E[W(x_0;t)] = \int_0^\infty e^{-\Lambda(x_0,t,t+s)} ds \tag{2.47}$$

2.4 Statistical estimation

The CMIP6 dataset contains the output of weather variables from several climate agencies from different countries. To analyze the extreme values and fit the distributions to the data, two different approaches were used in Chapters 3 and 4.

1. Fit a distribution for each of the climate models, creating an ensemble of outputs.
2. Pooling data from all models assuming that the different climate model data are independent thus resulting in a single parameter estimate for each of the parameters.

2.4.1 Gumbel model

The Non-stationary Gumbel distribution and density functions are denoted as $G(x;t)$ and $g(x;t)$, respectively with time-dependent location and scale parameters, $\mu(t)$ and $\sigma(t)$, respectively. Let, the annual maximum shock height in a given year t_i is given as x_i, then the likelihood of the parameters of the NS Gumbel for that climate model will be given as follows:

$$L(x_1,...,x_n;t_1,...t_n|\mu_0,\mu_1,\sigma_0,\sigma_1) = \prod_{i=1}^{n} g(x_i;t_i,\mu(\mu_0,\mu_1,t_i),\sigma(\sigma_0,\sigma_1,t_i)) \tag{2.48}$$

Therefore, for each model, we will obtain a set of parameter values using which the various EVD percentiles can be calculated for each member of the ensemble and then take the median of those values.

However, if we want to pool all the model outputs from the multi-model ensemble, assuming statistical independence of the various models, then, we can obtain the likeli-

hood as follows. Let $\{x_{ij}\}$ denote the set of annual maxima, in which each element x_{ij} represents the annual maxima in the $'i'$th year for the $'j'$th model. Consequently, the year corresponding to $\{x_{ij}\}$ is denoted as $\{t_{ij}\}$. Let there be n_j years of data from the jth model, then

$$L[\{x_{ij}, t_{ij}\}; \{n_j\}|\mu_0, \mu_1, \sigma_0, \sigma_1] = \prod_{j=1}^{m} \prod_{i=1}^{n_j} g(x_{ij}; \mu(\mu_0, \mu_1, t_{ij}), \sigma(\sigma_0, \sigma_1, t_{ij})) \tag{2.49}$$

In this case, we will obtain only one estimate for the parameters for the NS Gumbel model. For the estimation of the stationary cases, the time-dependent parameters can be eliminated in Equation (2.48) to obtain,

$$L(x_1, ..., x_n|\mu, \sigma) = \prod_{i=1}^{n} g(x_i, \mu, \sigma) \tag{2.50}$$

2.4.2 NHPP model

The maximum likelihood estimation procedures for the estimation of the rates and intensities are presented below.

2.4.2.1 Rate function

Using the joint density function of the arrival times and the number of events until a given time t for an NHPP, the likelihood of events until a given time t can be given as follows [92]:

$$L_{S_1,...,S_n;N(t)}(s_1, ..., s_n; n) = exp[-\Lambda(t)] \prod_{i=1}^{n} \lambda(s_i) \tag{2.51}$$

For a log-linear rate function, the likelihood function for the estimation of the parameters in the rate function is given as follows.

$$L((s_1, ..., s_n; n|\lambda_0, \lambda_1) = exp\left[-\frac{1}{\lambda_1}\left(e^{(\lambda_0+\lambda_1 t)} - e^{(\lambda_0)}\right)\right]\prod_{i=1}^{n}[e^{(\lambda_0+\lambda_1 s_i)}] \tag{2.52}$$

The ML estimates can be obtained by minimizing the logarithm of the likelihood function with respect to the parameters λ_0 and λ_1.

The ML estimate for the rate of stationary Poisson process is given by the rather simple expression as follows, in which N denotes the total number of shock incidences, i.e., the number of threshold crossings in this case in the duration of T years.

$$\hat{\lambda} = \frac{N}{T} \tag{2.53}$$

Considering the second approach for the estimation where all the climate model data were pooled under the assumption that the climate models are independent, the likelihood functions can be modified as follows. Suppose s_{ij} denotes the $'j'$th arrival time for the $'i'$th model. Let n_j denote the number of events in the $'j'$th model path, and let the number of models be m. T denotes the end time (in this case 80 years, i.e. 2020-2100).

$$L[\{s_{ij}\}; \{n_j\}|\lambda_0, \lambda_1] = \prod_{j=1}^{m} exp\left[-\frac{1}{\lambda_1}\left(e^{(\lambda_0+\lambda_1 T)} - e^{(\lambda_0)}\right)\right]\prod_{i=1}^{n_j}[e^{(\lambda_0+\lambda_1 s_{ij})}] \tag{2.54}$$

Taking the logarithm and optimizing with respect to the rate parameters will yield the maximum-likelihood estimates.

2.4.2.2 Shock height distribution

The parameters of the shock height distribution are estimated using the shock heights corresponding to their arrival times as defined in . For a Weibull shock height distribution, with a linear scale parameter and a constant shape parameter, the likelihood function for the estimation of the parameters for each of the model paths can be constructed as follows:

$$L(x_1, ..., x_n; s_1, ...s_n; n|\alpha, x_0, \beta_0, \beta_1) = \prod_{i=1}^{n} f_X(x_i; x_0, \alpha, \beta(t) = \beta_0 + \beta_1 s_i) \tag{2.55}$$

Taking the logarithms of the above expression and maximizing this function with respect to the parameters, with the constraint that the overall scale parameter $\beta(t)$ is positive, will yield the estimates.

When all models are pooled, similarly to the likelihood of the rate parameters, the likelihood of the time-dependent shock height parameters can be obtained as follows, where $\{x_{ij}\}$ denotes the set of shock heights, in which each element x_{ij} represents the shock height of the $'i'$th event that occurs at s_{ij} in the $'j'$th model.

$$L[\{x_{ij}, s_{ij}\}; \{n_j\}|\alpha_0, \alpha_1, \beta_0, \beta_1] = \prod_{j=1}^{m} \prod_{i=1}^{n_j} f_{X(t)}(x_{ij}; \alpha(\alpha_0, \alpha_1, s_{ij}), \beta(\beta_0, \beta_1, s_{ij})) \tag{2.56}$$

The above likelihood was used to estimate the parameters of the time-dependent shape and scale parameters.

2.5 Conclusion

In this chapter, the contrast was drawn between the traditionally used Random variable method for extreme value analysis i.e. the Generalized Extreme Value (GEV) theories and with that of the proposed stochastic process models, in particular the Poisson process models. The changing climate demands that the gradual non-stationarity in the climate process be reflected in the extreme value analysis (EVA) of the climate-driven hazard processes. In that context, initially, both the stationary and non-stationary versions of the GEV were discussed in detail along with their implementation in the literature.

Thereafter, the several challenges with the usage of the GEV models were discussed. Some of the prominent challenges are summarised as follows:

- GEV methods lack specificity about the underlying hazard process towards the reflected changes in EVD over time.
- Increments in the frequency and that of intensity of events have the same effect on the random variable method and hence the effect cannot be separately assessed based on the changes in the EVD.
- Although the concept of return period is applicable for stationary processes, but in a non-stationary scenario, the return periods cannot be defined for recurring events.

To tackle these challenges and gain deeper insights about the underlying process in the EVA, the stochastic process-based EVA was proposed. Therefore, a stochastic shock process, more specifically, the non-homogeneous Poisson process (NHPP) model, was proposed for the EVA. The two main components of the marked NHPP hazard process, which are the rate function and the time-dependent intensity functions are discussed in detail. The several concepts and theories such as the distribution of arrival times, return periods, and Extreme value distribution for this process were presented with supporting derivations. In this proposed approach, the non-stationarity can be conveniently modelled using time-dependent rate and intensity functions and hence their effect of the changes in the MVDs can be easily distinguished.

Chapter 3

Non-Stationary Model of Precipitation Events

3.1 Introduction

3.1.1 Background

Simulations carried out by various agencies using simulated climate data indicate that there will likely be an increase in the intensity and frequency of hazards, such as floods [58], landslides [52], droughts [32], and wind activities [11] in several regions of the world, posing a greater risk in those areas.

Although in most of the available literature, the models are fitted to historical data, the simulated data from the general circulation models is not utilized to predict the changes in climate variables. In this chapter, we model the precipitation variable using a marked NHPP process, show the applicability of the process in modelling weather variables, and estimate the weather extremes over the remainder of the current century. Several other key results of the NHPP analysis conducted on the precipitation variable have been presented in this chapter.

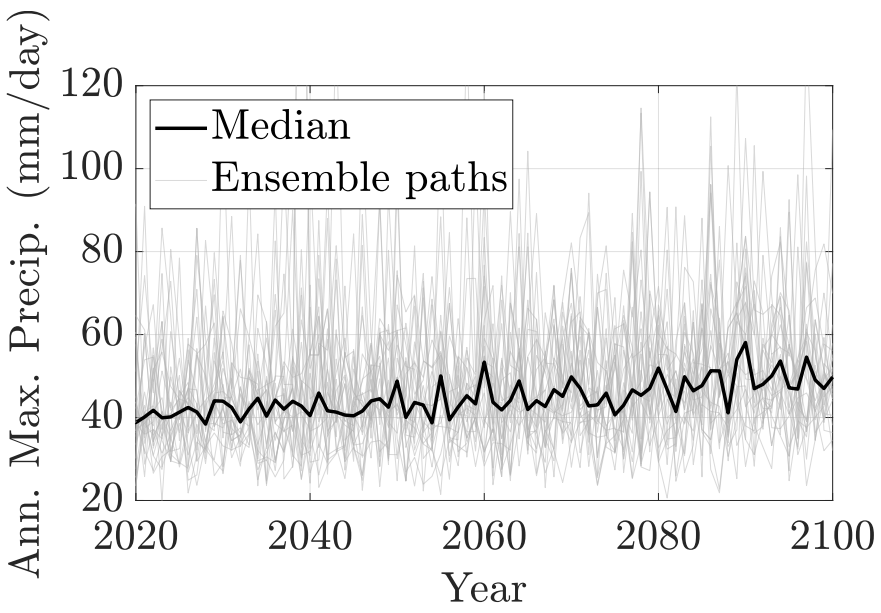


Figure 3.1: CMIP6 Multi-model ensemble for the projected annual 24-hour precipitation values for SSP5-8.5 scenario

3.1.2 Data

For this study, the multi-model ensemble corresponding to the Coupled Model Intercomparison Project Phase 6 (CMIP6) was considered. CMIP6 is based on Shared Socio-Economic Pathways (SSP) scenarios. These SSP scenarios describe the social and economic factors that influence radiative forcing and, hence, indicate different levels of global warming. For the precipitation variable, 26 different model outputs were available for the period 1950–2100, as listed in Table 3.1. For our demonstration, we extracted simulated daily precipitation data in mm/day for the grid point with coordinates Lat: 43.625, Lon: -79.375 (in the region of Toronto, Ontario). This data corresponds to SSP5-8.5, the 'Fossil-fueled Development' pathway, which is a scenario with high challenges to mitigation and low challenges to adaptation, with a radiative forcing of RCP8.5 (the Representative Concentration Pathway).

Table 3.1: Multi-model ensemble and their reporting institutes in CMIP6 for precipitation

Model	Reporting institute
ACCESS.CM2	Commonwealth Scientific and Industrial Research Organisation (CSIRO)
ACCESS.ESM1.5	Commonwealth Scientific and Industrial Research Organisation (CSIRO)
BCC.CSM2.MR	Beijing Climate Center
CanESM5	Canadian Centre for Climate Modelling and Analysis, Environment and Climate Change Canada, Victoria, Canada
CMCC.ESM2	Fondazione Centro Euro-Mediterraneo sui Cambiamenti Climatici (CMCC), Lecce, Italy
CNRM.CM6.1	Centre National de Recherches Meteorologiques, Centre Europeen de Recherche et de Formation Avancee en Calcul Scientifique, Toulouse, France
CNRM.ESM2.1	Centre National de Recherches Meteorologiques, Centre Europeen de Recherche et de Formation Avancee en Calcul Scientifique, Toulouse, France
EC.Earth3	EC-Earth consortium, Rossby Center, Swedish Meteorological and Hydrological Institute/SMHI, Norrkoping, Sweden
EC.Earth3.Veg	EC-Earth consortium, Rossby Center, Swedish Meteorological and Hydrological Institute/SMHI, Norrkoping, Sweden
FGOALS.g3	Chinese Academy of Sciences, Beijing, China
GFDL.ESM4	National Oceanic and Atmospheric Administration, Geophysical Fluid Dynamics Laboratory, Princeton, NJ, USA
HadGEM3.GC31.LL	Met Office Hadley Centre, Exeter, Devon, UK
INM.CM4.8	Institute for Numerical Mathematics (INM), Russian Academy of Science, Moscow, Russia
INM.CM5.0	Institute for Numerical Mathematics (INM), Russian Academy of Science, Moscow, Russia
IPSL.CM6A.LR	Institut Pierre Simon Laplace (IPSL), Paris, France
KACE.1.0.G	National Institute of Meteorological Sciences; Korea Meteorological Administration
KIOST.ESM	Korea Institute of Ocean Science and Technology (KIOST), Busan, Republic of Korea
MIROC.ES2L	Japan Agency for Marine-Earth Science and Technology (JAMSTEC), Kanagawa, Japan Atmosphere and Ocean Research Institute (AORI), The University of Tokyo, Chiba, Japan National Institute for Environmental Studies (NIES), Ibaraki, Japan RIKEN Center for Computational Science, Hyogo, Japan (MIROC)
MIROC6	Japan Agency for Marine-Earth Science and Technology (JAMSTEC),Kanagawa, Japan Atmosphere and Ocean Research Institute (AORI), The University of Tokyo, Chiba, Japan National Institute for Environmental Studies (NIES), Ibaraki, Japan RIKEN Center for Computational Science, Hyogo, Japan
MPI.ESM1.2.HR	Max Planck Institute for Meteorology (MPI-M), Hamburg, Germany
MPI.ESM1.2.LR	Max Planck Institute for Meteorology (MPI-M), Hamburg, Germany
MRI.ESM2.0	Meteorological Research Institute (MRI), Tsukuba, Ibaraki, Japan
NorESM2.LM	NorESM Climate modelling Consortium, Oslo, Norway
NorESM2.MM	NorESM Climate modelling Consortium, Oslo, Norway
TaiESM1	Research Center for Environmental Changes, Academia Sinica, Nankang, Taipei, Taiwan
UKESM1.0.LL	Met Office Hadley Centre, Exeter, UK

Table 3.2: Gumbel parameters and percentile values for the base period 1951-1990.

	Multi-model median mm/day	Range mm/day
Gumbel location μ	35.071	[33.428, 37.012]
Gumbel scale σ	9.097	[6.893, 10.916]
50th percentile	38.405	[36.488, 40.795]
80th percentile	48.716	[44.797, 53.08]
90th percentile	55.543	[49.97, 61.271]
95th percentile	62.091	[54.931, 69.129]

3.2 Base Period -Stationary climate

A base model is necessary to compare the predicted percentiles of extreme values in the future, for which the simulated precipitation data in the preindustrial period of 1951-1990 are considered. The base case scenario in this period is assumed to be stationary and the extreme value distributions (EVDs) was estimated.

Since it is intended to compare the estimated extreme values with that of the estimates for the future period (2020-2100), the analysis was conducted for both the Gumbel Model and Stochastic process model for the base case.

3.2.1 Gumbel Extreme Value Analysis

The median of the estimated parameters of the Gumbel EVs and some typical percentiles of the distributions for each of the 26 GCMs, along with their ranges, are tabulated in Table 3.2. The inter-model variability is shown through the ensemble plots of the cumulative distributions in Figure 3.2.

The maximum likelihood estimates of the parameters obtained for the several models used in this study shows inter-model variability. To represent this variability, the histograms of some of the typical parameters are provided for reference in this section.

Figures 3.3 and 3.5 shows the variability of the parameters of the stationary Gumbel distributions and HPP model for the analysis of the base period as discussed in Sections 2.2.1

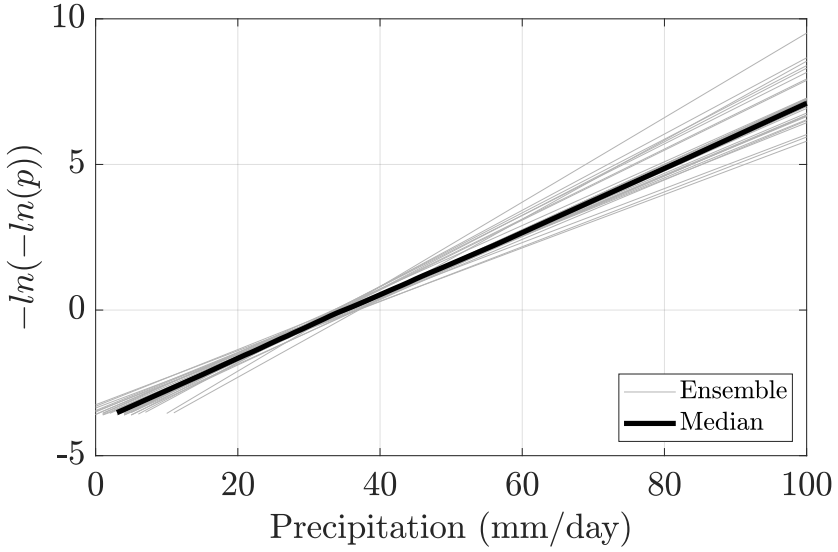


Figure 3.2: Fitted Gumbel probability plots for annual maximum precipitation for the base period 1951-1990

and 2.3.1.1.

3.2.2 Stochastic process model

The heavy precipitation events can be modelled using a stationary Poisson process whose rate and depth are estimated as follows.

3.2.2.1 HPP rate

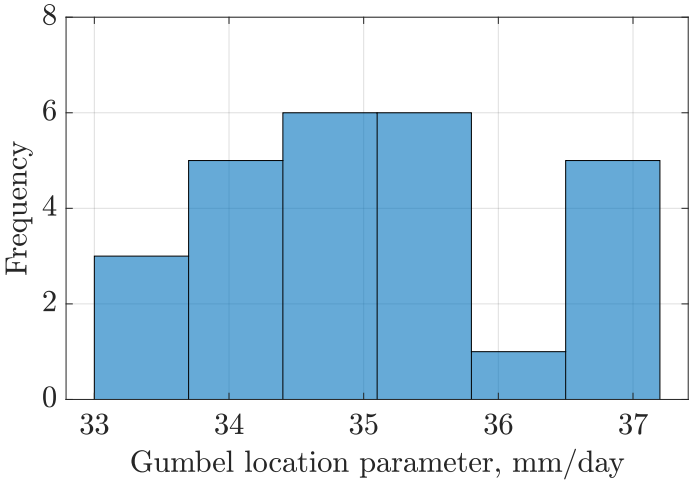
Since during the base period 1950–1990, the number of events that cross any given threshold values does not vary much from model to model, precipitation events that cross 25 mm / day were extracted, giving around 3–4 events per year for each of the models.

3.2.2.2 Precipitation depth distribution

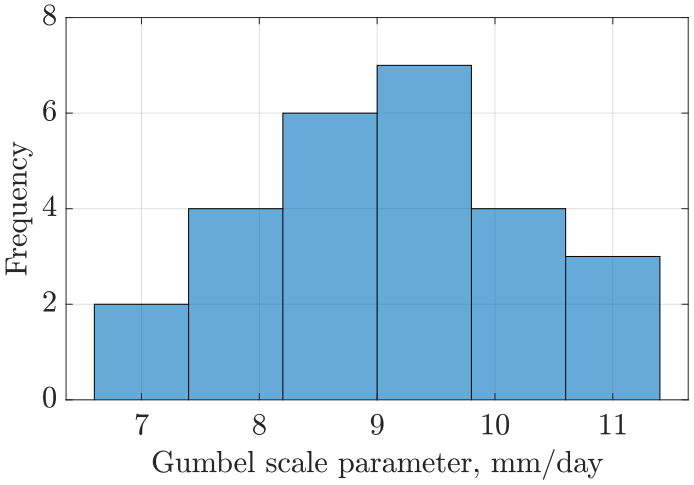
For the second component of the stochastic process model, that is, the shock height distribution ($F_X(x)$ (precipitation), the Weibull distribution was found to be the best fit in terms of the log-likelihood values. The probability paper plot of the precipitation depths as shown in Figure 3.4 indicates that the Weibull distribution is a good fit for the data.

Another reason for selecting the Weibull distribution is that if the shape parameter approaches unity, it results in an exponential distribution, which is also frequently encountered in this kind of climatic data.

The annual maximum value distribution (MVD) for this HPP is calculated following Section 2.3.1.3 and the ensemble of the MVDs for each of the climate models is plotted in Figure 3.6, and some of the important percentiles are listed in Table 3.3.



(a) Location parameter



(b) Scale parameter

Figure 3.3: Histograms of the Gumbel parameters estimated for the base period showing the inter-model variability.

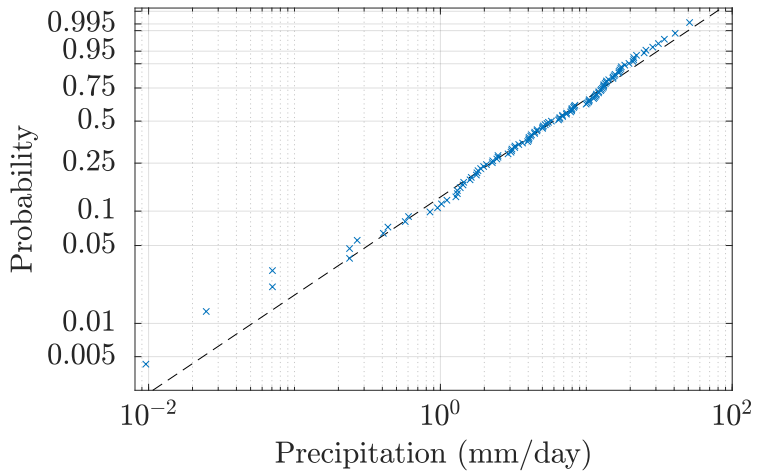
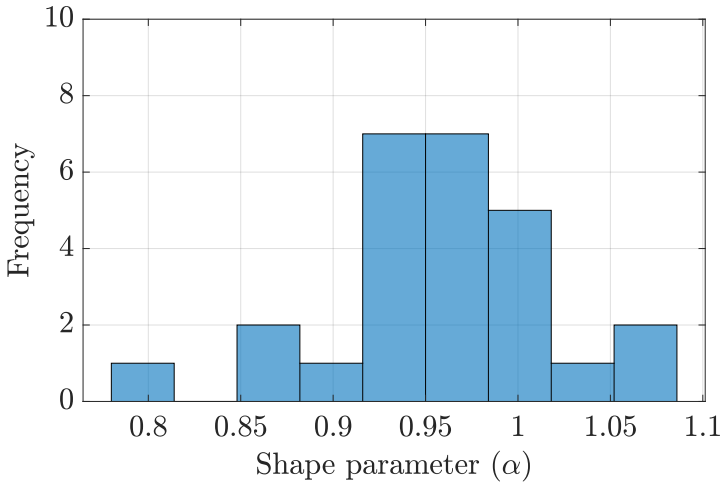


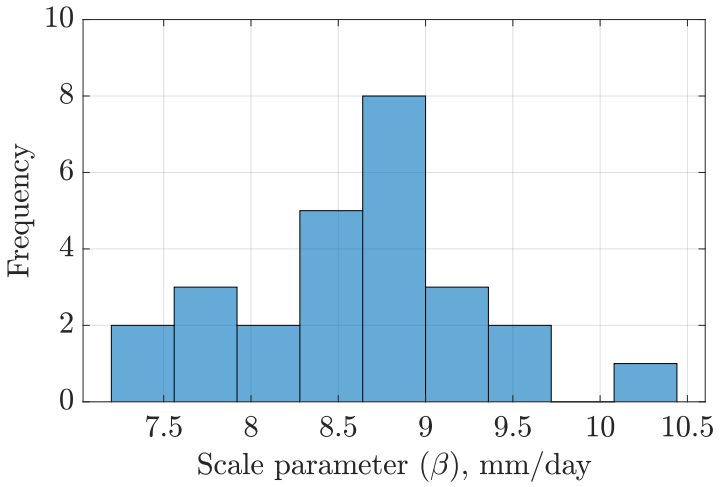
Figure 3.4: Weibull Probability Paper Plot with a Location Parameter of 25mm/day (Threshold Value)

Table 3.3: Ranges of HPP parameter estimates and percentile values of the EVD for the multi-model ensemble in the base period.

	Median	Range
HPP rate, λ	3.182	[2.9, 3.55]
Weibull shape, α	0.959	[0.799, 1.079]
Weibull scale, β, (mm/day)	8.604	[7.432, 10.375]
50th percentile, (mm/day)	38.348	[36.594, 40.098]
80th percentile, (mm/day)	48.917	[45.491, 52.114]
90th percentile, (mm/day)	56.058	[51.374, 60.551]
95th percentile, (mm/day)	62.990	[57.038, 70.001]



(a) Shape parameter



(b) Scale parameter

Figure 3.5: Histograms of the fitted Weibull distribution parameters estimated for the base period showing the inter-model variability.

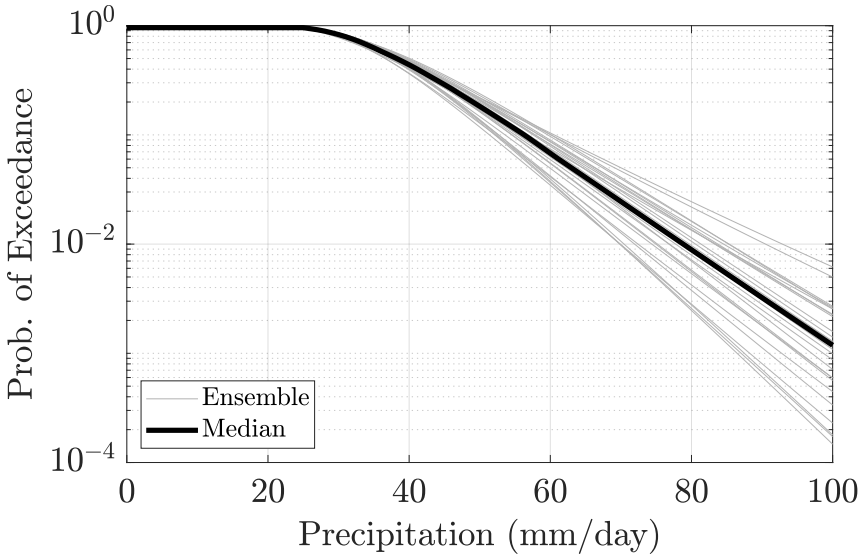


Figure 3.6: Annual probability of exceedance from the fitted HPP model for the base period 1951-1990.

Now that we have conducted the EV analysis for the base case using both methods that is the Gumbel EVA and the stochastic process method, we can proceed with the EVA for the future period 2020-2100.

3.3 Future period - Non-stationary Climate

For the predictions of the changes in the precipitation extremes, the period from 2020–2100 is chosen for the SSP-5 (8.5) scenario to analyze the worst-case scenario. Prevalent literature and preliminary trend analysis suggest that significant non-stationarity will be observed for the precipitation process during the mentioned period. Therefore, to model the time-dependence of the shock arrival process and the precipitation extremes, the non-stationary analysis was carried out. Using the climate model predictions from the CMIP6 multi-model ensemble, the EVA was conducted using the non-stationary Gumbel model and the stochastic process model, i.e., the non-homogeneous Poisson process model.

3.3.1 Non-stationary Gumbel EVA

The non-stationary Gumbel distribution is given in Equation (2.7), in which the location and scale parameters are now considered to be functions of time [22].

3.3.1.1 Parameter estimation

The scale parameter of the Gumbel distribution is impacted solely by the gradual changes in shock heights over time, whereas the location parameter is influenced by both changes in shock heights and the frequency of such events. This can be understood in a somewhat indirect manner by drawing the equivalence between the expression of the annual MVD for an HPP and the Gumbel EVD (not shown here).

Some common forms of time dependence of the location parameter are the linear form or the generalized polynomial form [51]. In this study we have considered a linear form for both the location and the scale parameters as follows:

$$\mu(t) = \mu_0 + \mu_1 t \tag{3.1}$$

$$\sigma(t) = \sigma_0 + \sigma_1 t \tag{3.2}$$

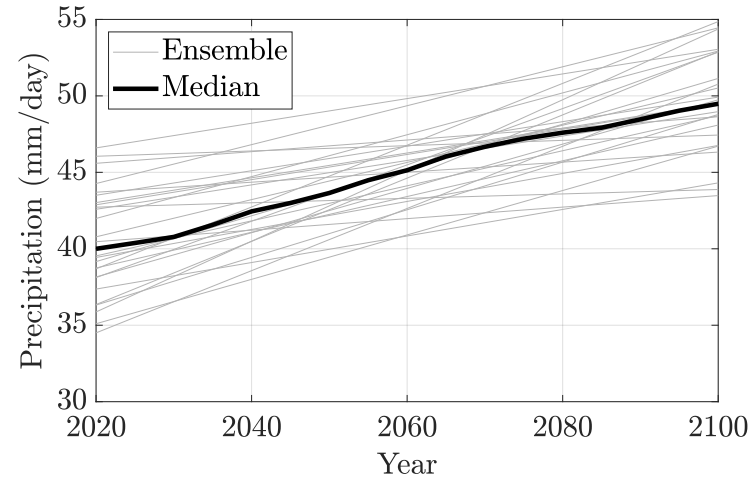
In the above expressions, the parameters μ_1 and σ_1 represents the linear rate of change of the the location and scale parameters with time, and, time variable t is considered to start from the year 2020, i.e. $t = 0$ for 2020. These parameters were estimated for each of the model paths in the duration 2020-2100. The estimated values of these parameters are listed in Table 3.4, and as can be seen, the parameters μ_2 and σ_2 are all greater than zero, indicating a positive time-dependent trend over the period.

Table 3.4: Non-stationary Gumbel parameters

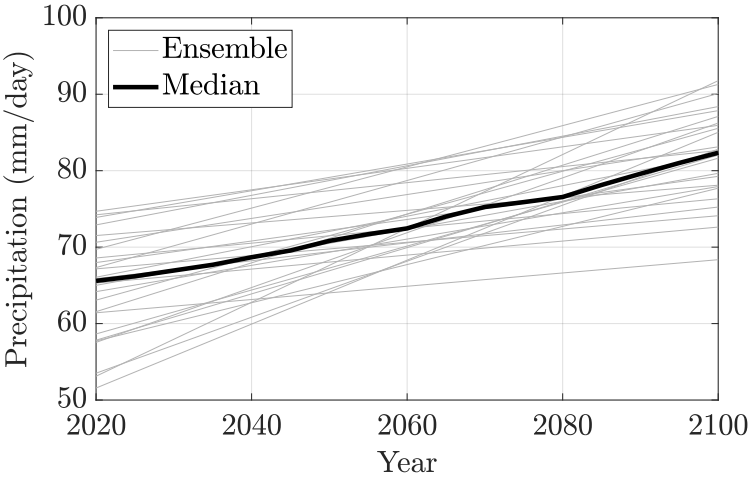
	Mean (mm/day)	Range (mm/day)
μ_1	37.08	[32.03 42.29]
μ_2	0.098	[0.076, 0.122]
σ_1	9.319	[6.31 11.00]
σ_2	0.039	[0.029 0.050]

3.3.1.2 Annual maxima

With the estimated parameters the EVDs can be evaluated for each of the models using Equation (2.7). It can be seen in Figure 3.7, that ensemble median value of the 50th percentile (median) of the EVD rises from around 40mm/day to 49mm/day and the 95th percentile rises from 65mm/day to 82mm/day over the period 2020-2100, showing that the higher percentiles of the annual extremes are more affected due to the non-stationarity, although the change factors are roughly the same for both the percentiles.



(a) Median



(b) 95th percentile

Figure 3.7: The median and the 95th percentile values of the Gumbel annual EVD in the future period.

3.3.2 Stochastic process model

For the NHPP model, we require complete information on its two components, the rate function and the shock height distribution. Here as well, the same threshold value of 25mm/day is chosen to maintain coherency.

3.3.2.1 Rate estimation

A log-linear rate function has been chosen for this study as follows:

$$\lambda(t) = e^{(\lambda_0 + \lambda_1 t)} \tag{3.3}$$

which yields, a mean value function, given by the expected number of events over a given time as defined in terms of the rate function as follows:

$$\Lambda(t) = \int_0^t \lambda(t)dt = \frac{1}{\lambda_1}\left[e^{(\lambda_0+\lambda_1 t)} - e^{(\lambda_0)}\right] \tag{3.4}$$

The prime reasons of using a log-linear function is that

- Values of the parameters of the process are not bounded and any value of the parameters will result in a positive value of the rate function which is a necessity [117].
- The rate function does not start from zero which is the case for some other well known rate functions like the power-law rate function and this is more consistent with the process we are investigating since, a non-zero intercept at $t = 0$ is expected.

For reference, the number of events vs time and the fitted mean value function is plotted for IPSL.CM6A.LR model output in Figure 3.8 showing a good fit for the log-linear model.

Since in the stochastic process model the rate and the intensity of the events are split, it is easy to monitor the changes in the rate of events and that of the changes in the precipitation depths separately giving us more insights about the process. Figures 3.9 and 3.10 shows the ensemble and the median value of the rate functions and the mean value functions for the different models where it can be seen that the median value of

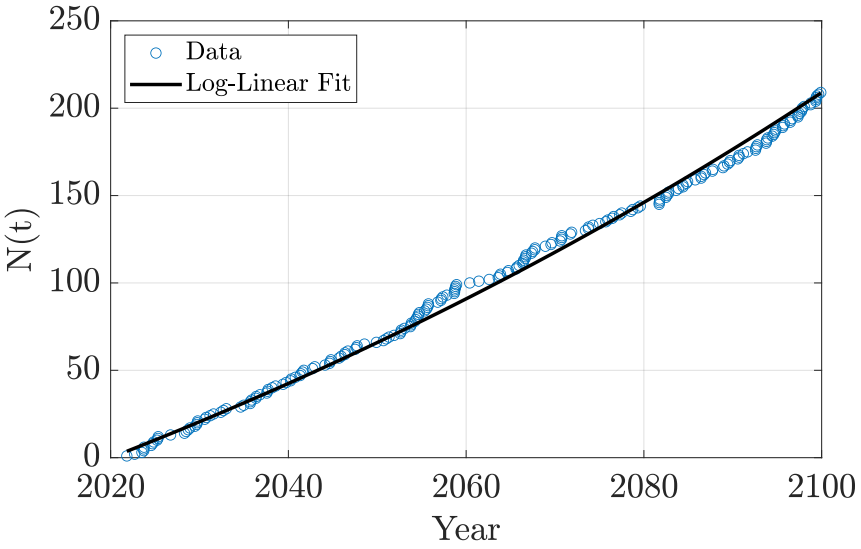


Figure 3.8: Fit of the mean value function with event times for IPSL.CM6A.LR model output in future period (2020-2100)

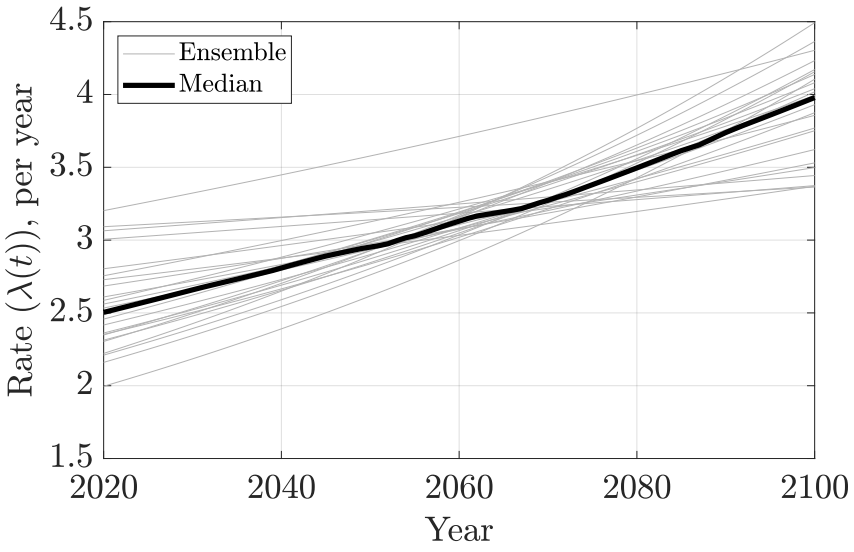


Figure 3.9: Fitted NHPP log-linear rate functions to the models in the future period (2020-2100)

the number of events can be expected to grow from 2.5 to 4 events/year (almost a 60% increase) in the period 2020-2100.

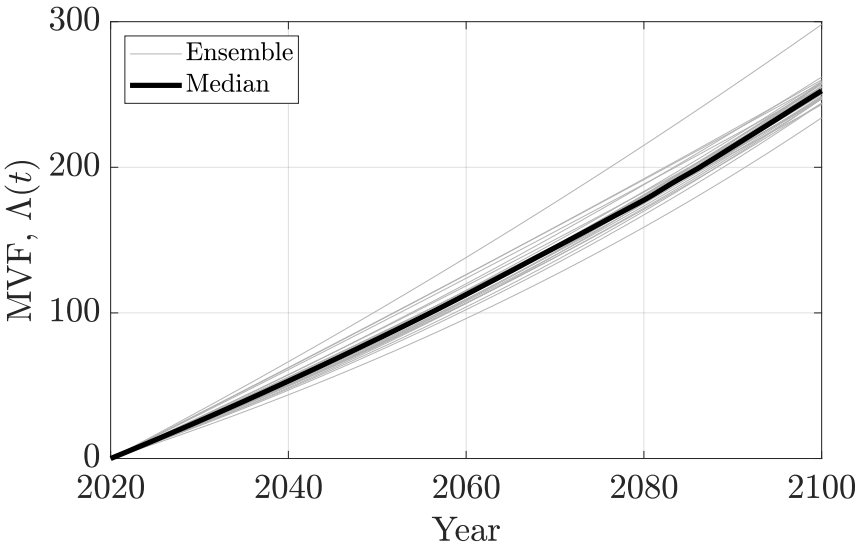


Figure 3.10: Fitted NHPP log-linear mean value functions to the models in the future period (2020-2100)

Having the estimates of the rate function for all models, let us proceed to the estimation of the shock height distribution and check the changes in severity of the precipitation events over time, which is the second vital component of the stochastic process.

3.3.2.2 NS precipitation depth

To show the time-dependence of the precipitation depth distribution, we have chosen a Weibull distribution with time-dependent scale parameter, keeping the shape parameter constant. The Weibull distribution was found suitable for this scenario for two primary reasons, it was the best fitted distribution for the historical precipitation depths and this distribution allows for sufficient flexibility to accommodate the changing shape of the distribution over time. The time dependent three-parameter Weibull distribution can be given as:

$$F_{X(t)}(x;t) = 1 - exp\left(-\left(\frac{x - x_0}{\beta(t)}\right)^{\alpha}\right) \tag{3.5}$$

in which α, β and x_0 represents the shape, scale and location parameters of the distribution.

The time-dependence of the scale parameter $\beta(t)$ is considered to be linear with parameters β_0 and β_1 as follows.

$$\beta(t) = \beta_0 + \beta_1 t \tag{3.6}$$

Similar to the rate function, a statistically significant value of β_1 would indicate a significant time-dependence for the shock height distribution. The ensemble median of the mean shock heights increases from 38 to 41 mm/day over the remaining century as seen in Figure 3.11, which may not seem much but has significant impact on the extreme value distribution as discussed in the next subsection.

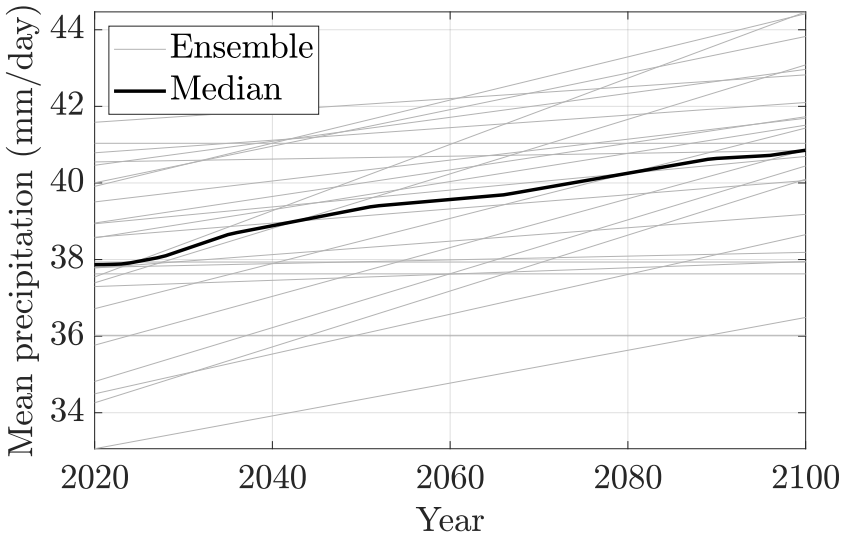


Figure 3.11: Changes in mean value of individual precipitation events in the future period

Therefore, in summary we have obtained the rate function and the time-dependent precipitation depth distribution for all the 26 GCM projections, as shown in tabular form in Table 3.5 and we can proceed to the calculation of their respective extreme value distributions. The full list of parameters estimates is provided in Appendix A.

Table 3.5: Estimated NHPP Rate and shock height (precipitation) distribution parameters

Model	Location parameter, (x_0) (mm/day)	Rate parameters $\lambda(t) = e^{(\lambda_0+\lambda_1 t)}$		Shock height distribution parameters (Weibull) $F_{X(t)}(x;t) = 1 - exp\left(-\left(\frac{x-x_0}{\beta_0+\beta_1 t}\right)^{\alpha}\right)$		
		λ_0	λ_1	α	β_0 (mm/day)	β_1 (mm/day/year)
KACE.1.0.G	30	1.031	0.003	0.950	10.543	0.016
HadGEM3.GC31.LL	26	1.310	0.002	1.000	8.259	0.073
UKESM1.0.LL	28	0.986	0.008	1.052	9.994	0.005
⋮	⋮	⋮	⋮	⋮	⋮	⋮

Similarly, the histograms of the parameter estimates of the non-stationary models are given in Figure 3.12.

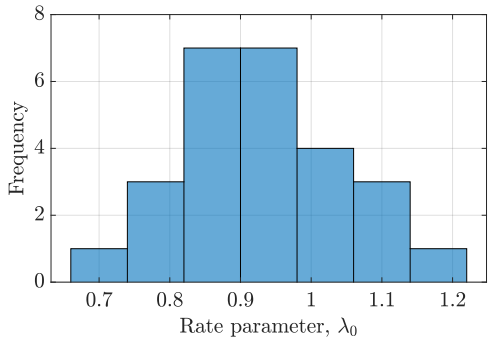
3.3.2.3 Annual maxima

The distribution of annual maxima for an NHPP can be obtained for any given time segment (t_1, t_2) without much of any computational hurdle [82], and the percentile values can be obtained by inverting the following EVD in Equations (2.39) and (2.40) numerically.

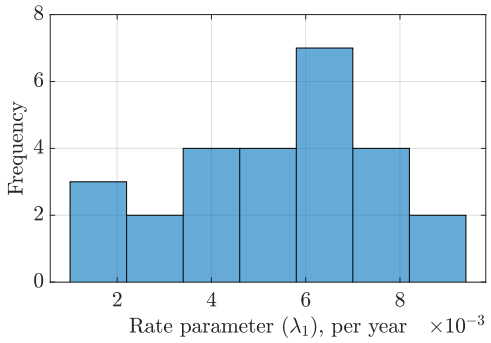
However, to compare our results with the Gumbel EVA, the annual extreme values of precipitation are computed using Equation (2.42)

The ensemble and the ensemble median plots of the annual maxima percentiles over the period 2020-2100 in Figure 3.13 shows that in terms of absolute values the higher percentiles changes more impacted similar to the results of non-stationary Gumbel EVA.

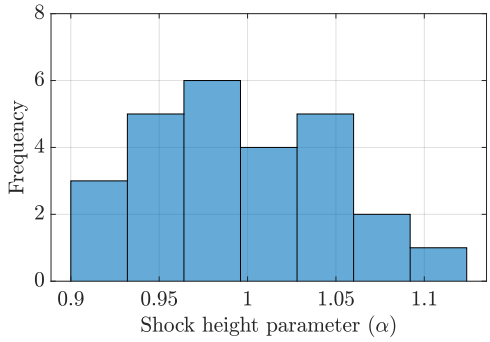
Therefore, it can be concluded that upon using the stochastic process model the results of EVA is preserved and comparable to the prevalent Gumbel models, however, the stochastic process models provide greater insights about the hazard process by decoupling the arrival process and the marks process in which the former gives information about the frequency changes and the later about the intensity changes. The following section highlights several other aspects of the stochastic process model that refines the concepts of return period which is more compatible in this gradually changing scenario.



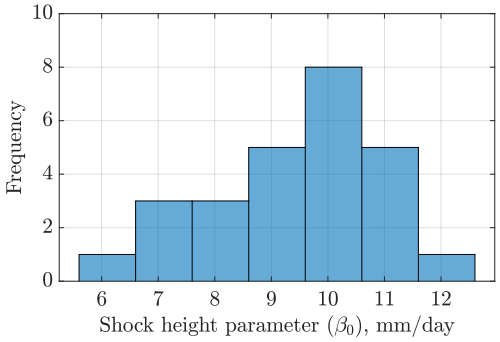
(a) Rate parameter, λ_0



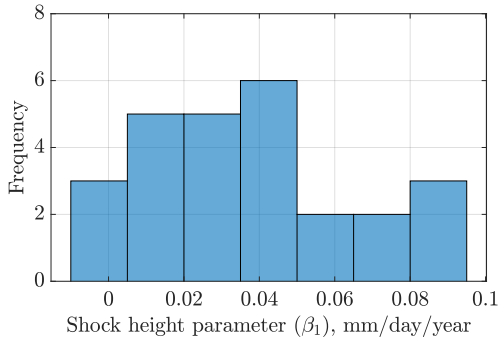
(b) Rate parameter (λ_1), per year



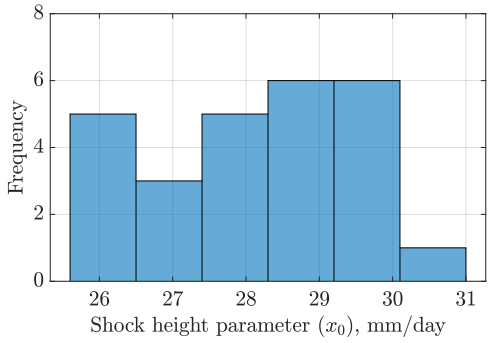
(c) Shock height parameter (α)



(d) Shock height parameter (β_0), mm/day

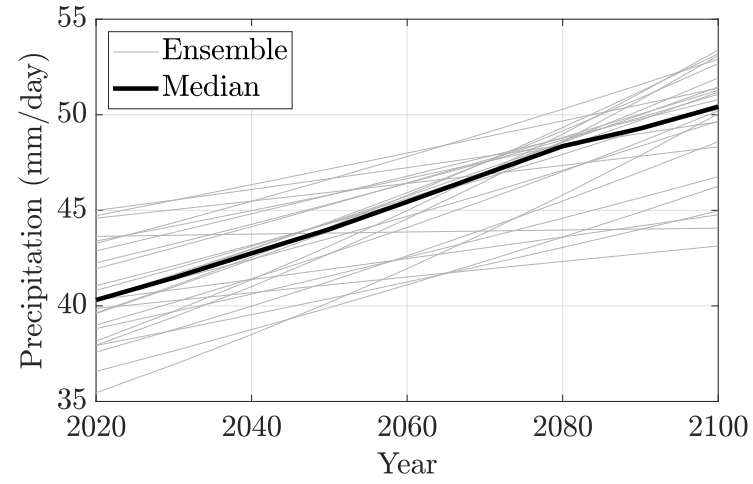


(e) Shock height parameter (β_1), mm/day/year

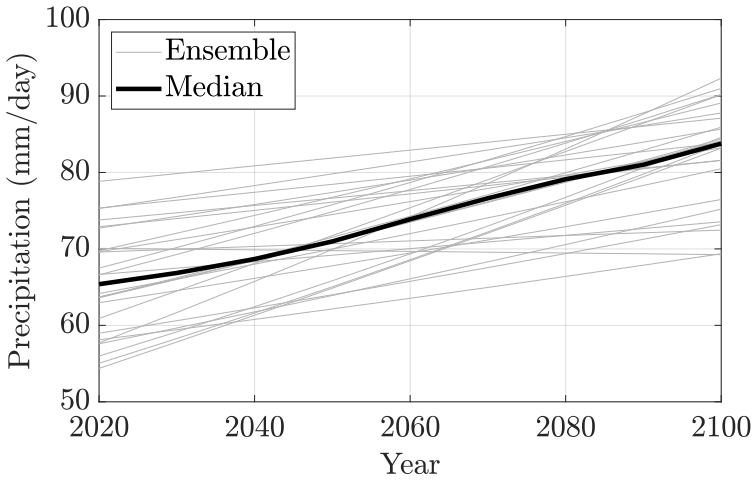


(f) Shock height parameter (x_0), mm/day

Figure 3.12: Histograms of the NHPP parameters estimated for the future period showing the inter-model variability.



(a) Median



(b) 95th percentile

Figure 3.13: The median and the 95th percentile values of the NHPP annual maximas in the future period.

3.3.2.4 Return periods and waiting times

The subsequent return periods are calculated for all the models for the NHPP model using Equation (2.45) for a design precipitation depth (x_0) equal to 65 mm/day and 80 mm / day which roughly correspond to 95th and 98th percentile of the precipitation depths, and plotted in Figure 3.14. The plot shows that there is a drastic decrease in return periods of high intensity precipitation events, for example the 10th return period for the precipitation event exceeding 80 mm/day can be expected to decrease by more than 60%.

Another important observation in Figure 3.14 would be to note that even the first return period for the two values of x_0 is much lower than 20 and 50 years, as one would expect for the 95th and 98th percentile values of the annual EVD in the stationary case.

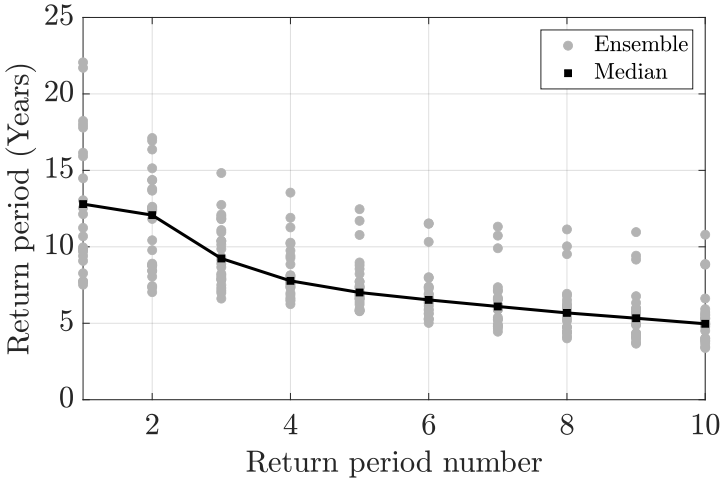
In Figure 3.15, which depicts the gradual decrease in the mean wait times, it can be seen that the initial waiting times i.e. in $t = 2020$, the waiting time and the values of the first return period depicted in Figure 3.14 are equal, which is consistent with the definitions.

It should be noted that equivalent definitions of non-stationary return periods are not applicable for the Gumbel EVA, and the heuristic way to define the return period of NS Gumbel as discussed in Section 2.2.2.1 is compared in Figure 3.16, which serves as one of the prerogatives of using the stochastic process model. It can be observed, that for higher return levels, the estimated return periods by NS Gumbel could be way higher than that estimated by the stochastic process model, which implies that for a given design life, the design load estimated using the NS Gumbel return period would be much less and hence lead to lower reliability.

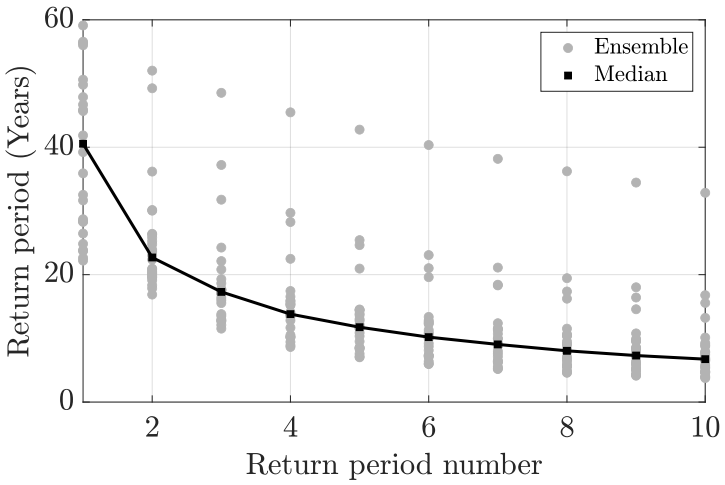
However, in the later years when the frequency of those high intensity events become higher, the return periods obtained using the heuristic definition of the NS-Gumbel gets close to the wait times calculations for the NHPP model.

3.4 Future period : 2070-2100

It was intended to check how the NHPP analysis compares with the Gumbel analysis for short-term trends in the data, for which here the last few decades of the century were

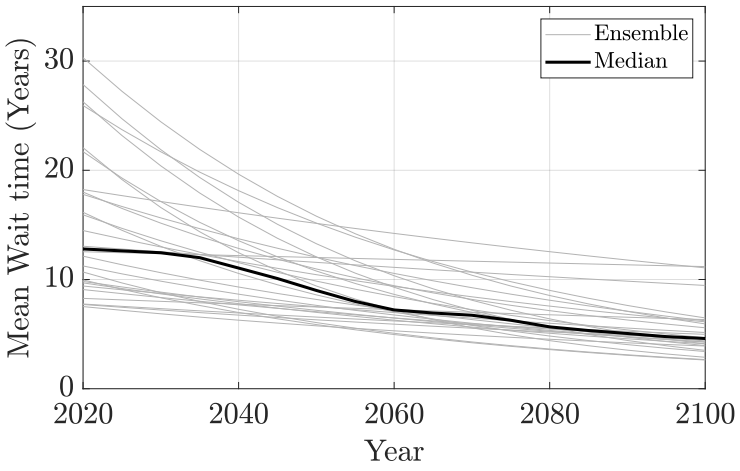


(a) 65 mm/day

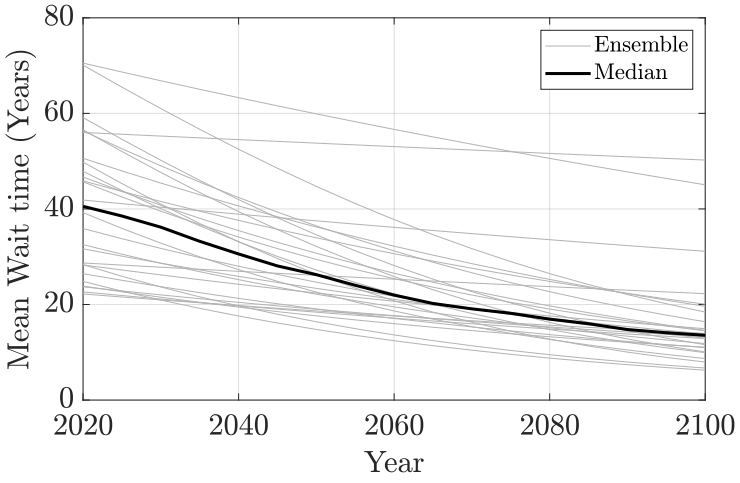


(b) 80 mm/day

Figure 3.14: NHPP return periods for given return levels.

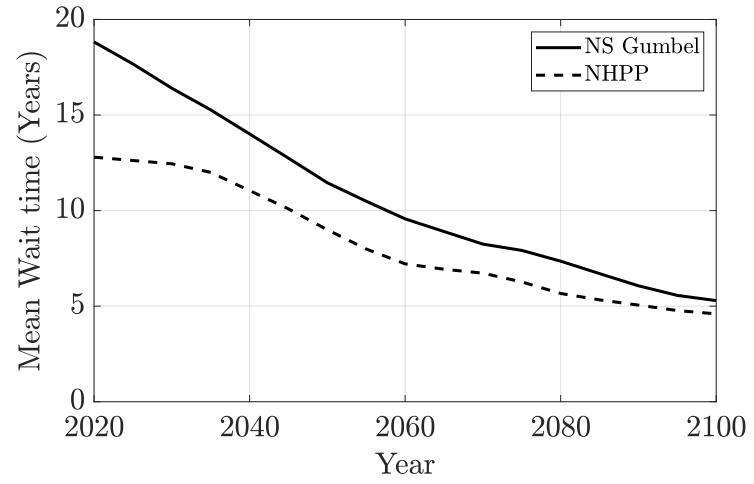


(a) 65 mm/day

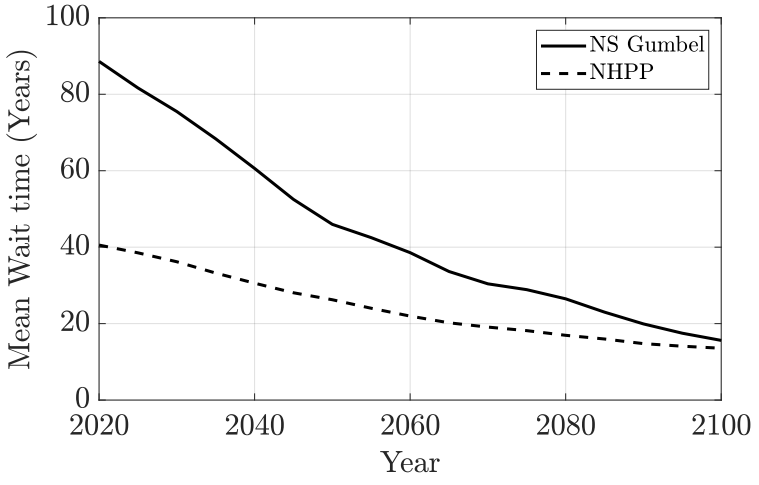


(b) 80 mm/day

Figure 3.15: NHPP mean waiting time till next event for given return levels.



(a) 65 mm/day



(b) 80 mm/day

Figure 3.16: NHPP mean waiting times compared with the NS Gumbel return period.

chosen for the analysis, that is from 2070-2100 (30 years) using the same CMIP6 data used in the previous section.

For convenience, only the median estimates of the various percentiles of the annual maxima were plotted to compare the different analyzes, while refraining from plotting the full ensemble for each case.

3.4.1 Non-stationary Gumbel EVA

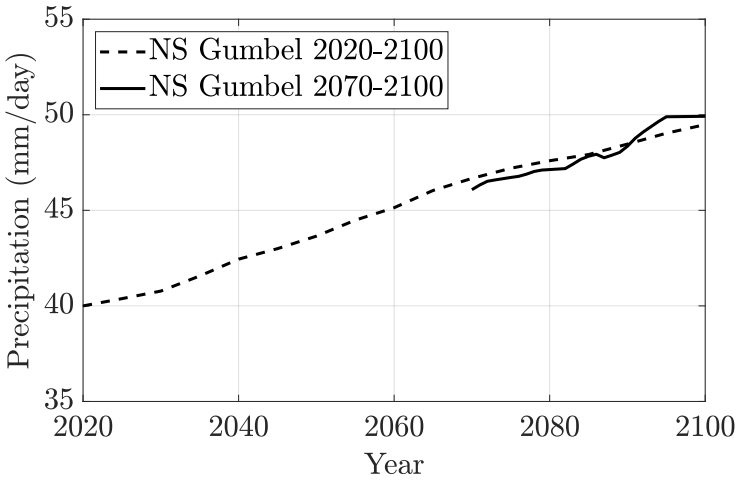
When the NS Gumbel analysis is performed, it is found that the re-analyzed results of the EVD compared well especially in the median measures, with slightly lower estimates of the 95th percentile as shown in Figure 3.17. This difference has resulted because the trends in this reanalysis is done without the influence of the trends in the period 2020-2070. However, for practical purposes and convenience in the design of infrastructure systems, a slightly conservative estimate would be more reliable.

3.4.2 Stochastic process model

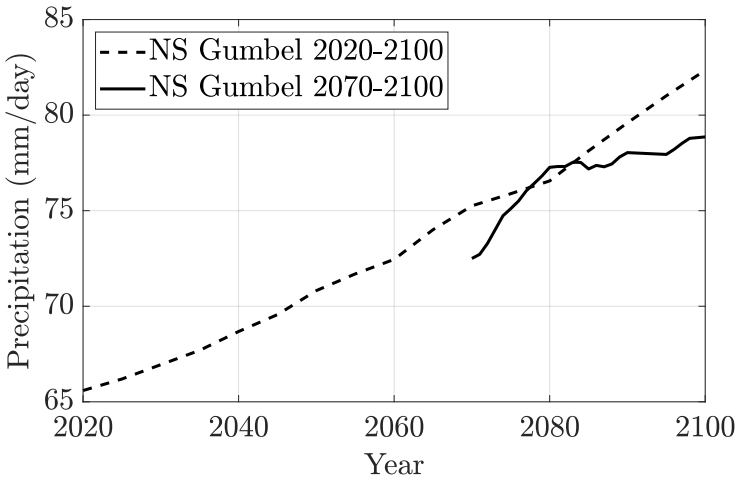
The observations for the NHPP analysis comparing the trends in the several percentiles of the annual maximas are similar to that of the observations in the NS Gumbel analysis. For example, here as well the 95th percentile estimates are slightly conservative for the case when the analysis is performed for the whole period as compared to the analysis of the last three decades.

3.5 Model Pooling

A second approach was to assume statistical independence among the difference climate models and pool all the models in ML estimation to obtain a single estimate from all the models. The details of the statistical estimation is discussed in Section 2.4. The median and the 95th percentile of the annual maximum precipitation obtained for the NHPP model

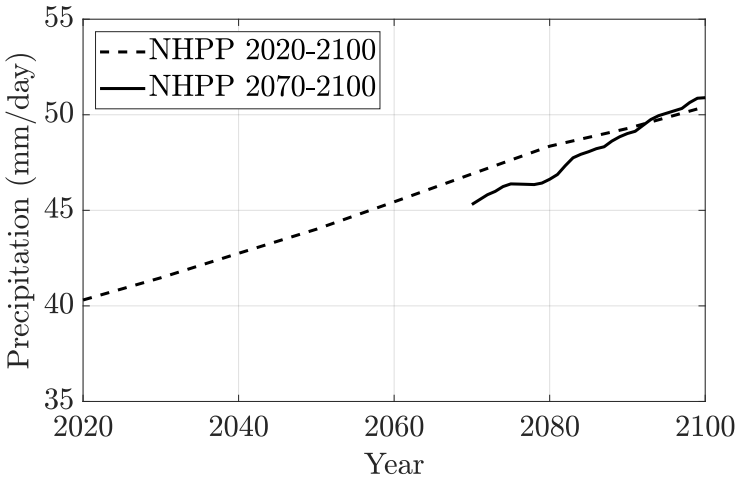


(a) Median

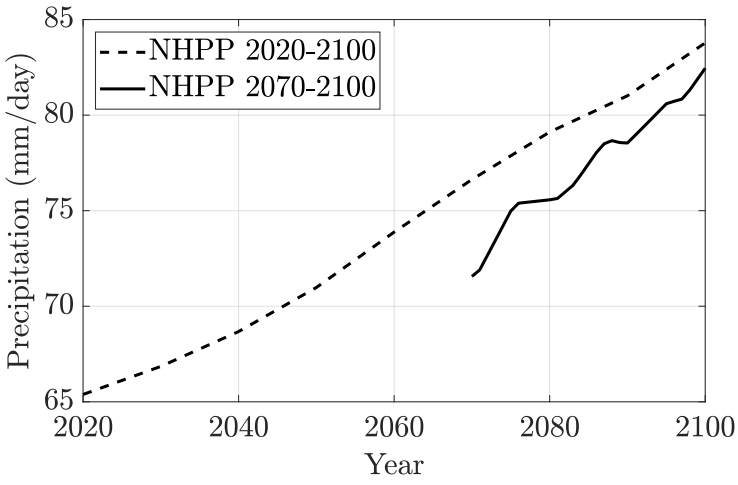


(b) 95th percentile

Figure 3.17: Comparison of the ensemble medians of different percentiles of annual maximas for the non-stationary Gumbel method



(a) Median



(b) 95th percentile

Figure 3.18: Comparison of the ensemble medians of different percentiles of annual maximas for the NHPP analysis

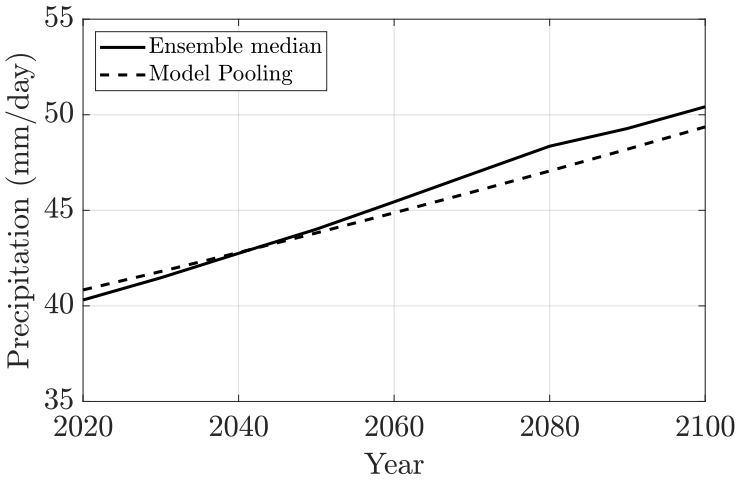
are tallied with the ensemble median estimates of the same percentiles estimated from the first approach.

The difference between the estimated percentiles using the two methods was found to be less than 2. 2% considering the Euclidean norms. Therefore, because of the simplicity of the second approach, it is used for modelling heatwaves in Chapter 4. However, the trade-off is that we cannot obtain the parametric uncertainties using this method and would require other methods such as bootstrapping or some Bayesian framework.

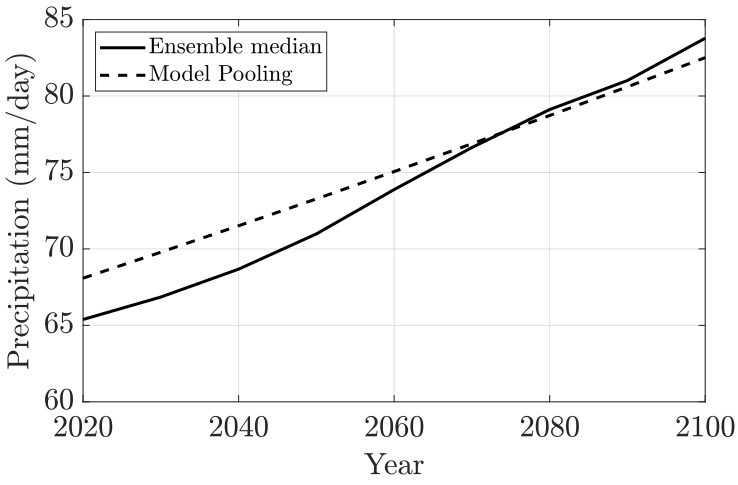
3.6 Discussion

Upon simultaneously comparing the ensemble medians of the different percentiles of the EVDs obtained from non-stationary Gumbel EVA and the NHPP annual maximum value distribution in Figure 3.20, it can be said that for both the analysis, the resulting changes in the percentile values are comparable with the NHPP maximas giving slightly conservative estimates. This is true for the second case also where only the last three decades before 2100 was considered for analysis.

Figure 3.20 also showcases the necessity of conducting a non-stationary analysis to obtain the necessary percentiles since the base case scenario which is obtained from stationary analysis for the period 1950-1990 grossly underestimates the gradual changes and increases in these percentiles owing to climate change. As it can be seen that the median of EVD increases by around 30% while the 95th percentile value increases by 33% over the base case, which is a significant increase and needs to be taken into account while deciding on the design precipitation depth.

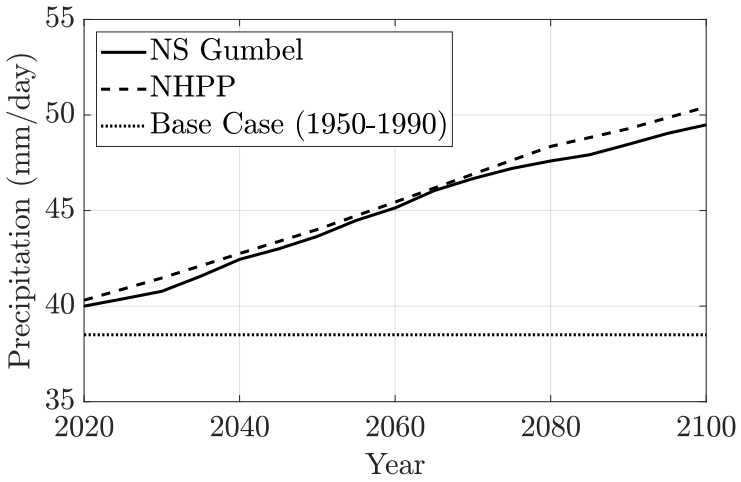


(a) Median

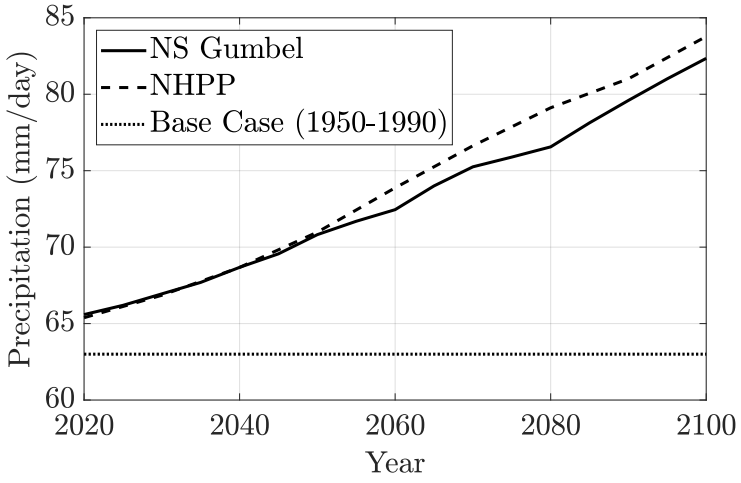


(b) 95th percentile

Figure 3.19: Comparison of the percentiles of annual maximum precipitation obtained as ensemble median and model pooling

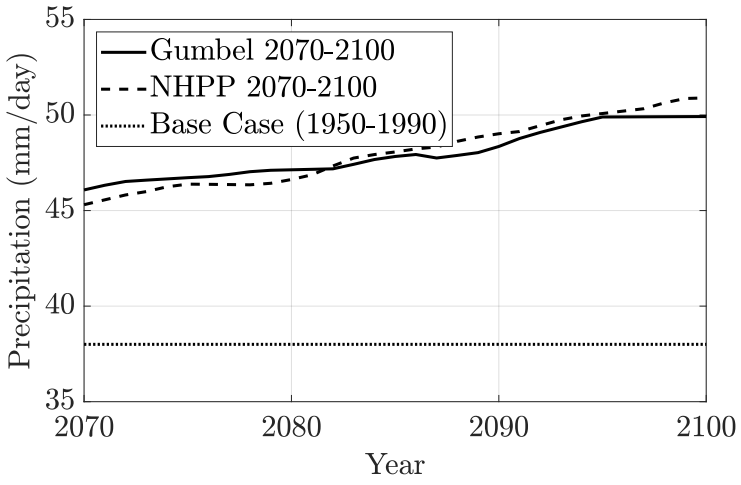


(a) Median

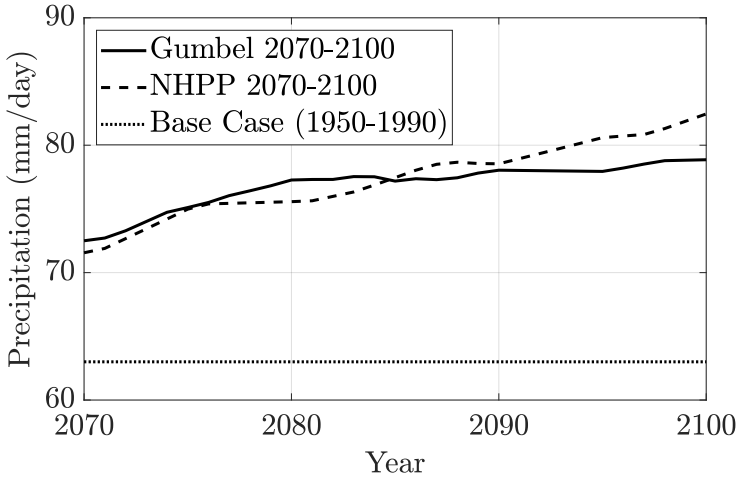


(b) 95th percentile

Figure 3.20: Comparison of the ensemble medians of different percentiles of annual maxima for the non-stationary Gumbel method and the NHPP for 2020-2100 period



(a) Median



(b) 95th percentile

Figure 3.21: Comparison of the ensemble medians of different percentiles of annual maxima for the non-stationary Gumbel method and the NHPP reanalyzed for 2070-2100 period

3.7 Limitations

The limitations of the analysis presented in this chapter are as stated as follows:

- The extrapolation of the model results far in the future may not be reliable due to limitations of the climate models.
- The proposed models captures the variability as described by the 26 climate models in the CMIP6 ensemble. However, the actual extent of the variability could be different from that described by the models.
- This analysis has been performed based on the predefined pathways for emissions scenarios, whereas in reality, the future conditions can be expected to be different than the scenarios suggested by CMIP6.
- Specifically, for the NHPP model, it is based on the assumption, that the events in disjoint intervals of time are independent, which may not be true for several climatic processes. However, its effect in this analysis will be limited since, the heavy precipitation events are well distanced to be influenced by these correlations. However, it may be noted that there are several other stochastic process models such as the Yule processes, that do account for these kind of correlations and can be used suitably.

3.8 Conclusions

In the context of climate change, where most natural hazard processes are expected to demonstrate non-stationarity in terms of frequency and intensity, it is imperative for the maximum value distributions to account for this dynamic trend. The Gumbel EVA allows for obtaining the annual extreme value distribution by adjusting time-dependent parameters, but it has certain limitations. Firstly, the escalation in annual extreme values cannot be specifically attributed to changes in event frequency or intensity. Additionally, in non-stationary scenarios, the definition of return period applies only to the initial return period, neglecting recurrent inter-arrival times.

To address these challenges, employing a stochastic process model, as proposed here, can prove to be beneficial. Such a model can effectively capture and monitor changes in both event frequency and intensity. In this study, simulated 24-hour precipitation data from the CMIP6 multi-model ensemble for SSP-5(8.5) scenario was utilized to illustrate gradual changes in frequency and intensity trends. Analysis was performed using both Gumbel methods and the stochastic process model, specifically the non-homogeneous Poisson process (NHPP) model.

Results indicate that annual extreme value distributions obtained from either method are comparable, and the results from the non-stationary analysis suggest that if using the stationary analyses results from the base period can underestimate the different percentile values of the EVD by more than 30% towards the end of the century. Concurrently, the return periods are also expected to plummet with every subsequent event occurrence, for example, the 10th return period can drop from 22 years to around 9 years for 80 mm/day precipitation events. Therefore, the stochastic process model offers deeper insights into the hazard process and facilitates the estimation of recurrent return periods by considering the mean of inter-arrival times.

Chapter 4

Non-Stationary Model of Heatwave Events

4.1 Introduction

4.1.1 Background

In the recent past, a heatwave event in British Columbia occurred during 25 June-2 July, 2021, where temperatures reached 49.5°C killing more than 619 people [128] and similar extreme heatwave incidents took place in British Columbia in 2009 [59] and Quebec in 2010 [13]. Several more devastating heatwave related incidents were witnessed in the USA in 2003, 2021, and 1988 resulting in the over 35000 deaths and 10 billion USD losses [54]. This chapter will focus on another application of stochastic shock process models to model extreme heatwaves, utilizing CMIP6 data.

A heatwave is characterized by at least two parameters: temperature and duration. Typically, a temperature threshold is established for a specific region based on the typical summer temperatures observed therein. When this threshold is exceeded and sustained for a predefined duration, a heatwave is considered to have occurred. This threshold may be specified as a fixed temperature or as a higher percentile of the temperatures observed on that particular day of the year over a historical reference period [95].

Heatwaves have both direct and indirect impacts on society and the environment, such as loss of lives and economic damage. These events are also closely connected to other natural hazards like droughts[131], wildfires[69], and health-related issues[110]. The definition of a heatwave event is determined by the specific goals of the analysis. For example, from a health perspective, even a short period of 2-3 days with temperatures exceeding a high percentile value, accompanied by high humidity, is considered a heatwave, since even a short duration of exposure to unusually high temperatures and humidity can result in adverse health effects such as heat strokes or mortality associated with it [110]. In contrast, when analyzing from the point of view of drought or water resources, a longer duration of 5-6 days with temperatures exceeding a lower threshold is considered a heatwave [47]. Therefore, in addition to the highest temperature reached in the heatwave the duration plays a significant role in determining the losses due to the heatwave.

Therefore, studying the frequency of heatwave patterns is essential to assess the associated risks comprehensively. With the onset of global warming, it is apparent that heatwaves will become more frequent and severe in the coming future, as suggested by multiple studies[7, 43, 34, 90, 128, 89].

The availability of CMIP6 multimodel ensemble data for future years under different SSP scenarios has enabled the study of future trends in heatwaves. However, it should be noted that performance of these models may vary in different aspects, for example, some model outputs in the ensemble may be more representative of the spatial correlations in a given region, while others may be more accurate when the temporal trends are compared with the historical data. When the CMIP6 data was analysed for India, it was found that the models have a warmer bias in the June-July-August (JJA) months, i.e the predicted temperature means were found to be significantly more than that observed in the historically observed temperatures [76], and a similar warmer bias to the extent of around 8°C for both CMIP5 and CMIP6 was observed for the region of Northern Canada [48].

The analysis of the CMIP6 data suggests that if the climate change is considered, the return period of the so called 'rare' events such as the the British Columbia heatwave in 2021 are much lower than expected indicating increasing frequency of such events over time [68]. Other phenomenon like atmospheric blocking, defined as strong vortices that affect the the westerly flow lasting for several days have shown to be correlated with heatwave

events and hence may trigger drought like conditions. Analysis on the CMIP datasets and CanESM large ensembles have shown increased frequency of such events during 2070-2100 as compared to the baseline period of 1981-2010 [54].

This analysis is distinct from the extreme temperature modelling [63, 114], since here we do not intend to model the annual maximum temperature but model the duration of the heat waves as the shock heights.

Since a large number of heatwave events are not encountered each year for a given region, usage of a Gumbel model to obtain the distribution of the maximum duration of a heatwaves in a given year may not be appropriate, since it would not maintain the asymptotic assumption underlying the extreme value theory. In this case, the stochastic process model can prove to be robust in identifying the trends in the rate and duration of these heat wave events. However, for the sake of comparison and completion, the typical NS Gumbel analysis was conducted simultaneously with the NHPP analysis.

4.1.2 Data

For the analysis, the CMIP6 multi-model ensemble for the daily maximum and minimum temperatures are considered for the three SSP scenarios, SSP1(2.6), SSP2(4.5) and SSP5(8.5). The ensemble consists of the 26 model outputs (the same as the models used in the precipitation analysis in Chapter 3. The daily data is obtained for a single grid box of resolution 6km x 10km (0.0833°latitude x 0.0833°longitude) in Toronto (43.70833, -79.375).

4.2 Analysis

In Toronto region, as per the recommendations of Meteorological Service of Canada (MSC), an extreme heat warning is issued if the days maximum temperature, T_{max} is greater than or equal to 31 degree Celsius accompanied by the days minimum temperature equal to or exceeding 20 degree Celsius, and this condition prevails for at least a duration of 2 consec-

utive days [5]. Based on this definition, heatwave events are identified from temperature data, an example of which is shown in Figure 4.1.

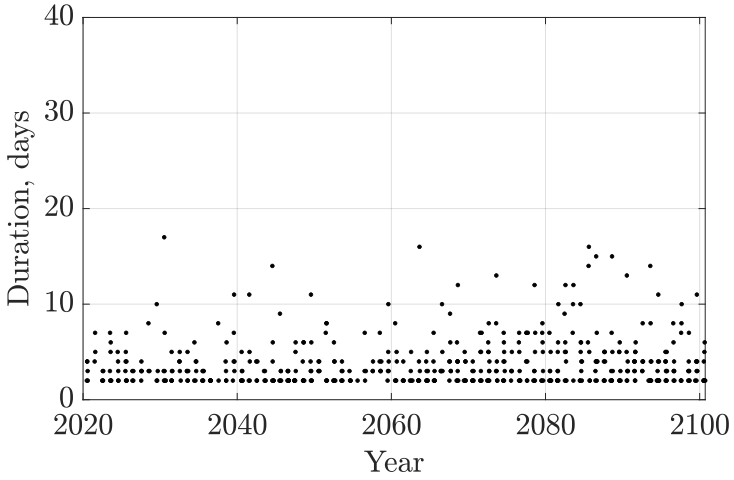
The methods for rate and intensity estimation in this chapter are followed similar to the approaches discussed in Chapter 3. Following the fact from the precipitation analysis, that pooling all the models in the likelihood to obtain a single estimate gives the results close to the median estimates obtained from analyzing each of the climate model data separately, here the models are pooled together to maintain the simplicity of the results. This is done on the basis of the assumption that the output of the different climate models is statistically independent. However, it may be noted here that in this case it is assumed that the functional forms of the rate and the duration for each of the models is assumed to the same for all the climate model data, for example, for the rate function estimation, we need to assume that all the models follow a log-linear rate function for the estimation process, which does not need to be maintained if the different model outputs are analyzed separately.

4.2.1 NS Gumbel

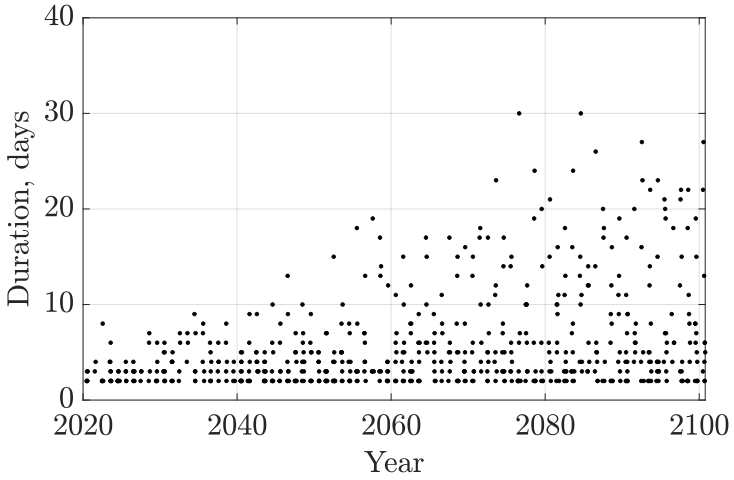
The non-stationary Gumbel analysis was done to serve as a contrast to the NHPP analysis on the same data set by extracting the annual maximum duration of the extreme heat events for all models. Maximum likelihood estimation was performed to obtain the parameters of the time-dependent scale and location parameters of the NS Gumbel distribution. The location parameter and the scale parameters are taken to be log-linear for simplicity as follows:

$$\begin{aligned} \mu(t) &= exp(\mu_0 + \mu_1 t)\ days \\ \sigma(t) &= exp(\sigma_0 + \sigma_1 t)\ days \end{aligned} \tag{4.1}$$

For comparison, we have also performed the analysis of the reference period used in this analysis, that is, the period 1950-1990 using constant shape and scale parameters, assuming stationarity in that time period, similar to the precipitation analysis in Chapter 3.



(a) SSP 2(4.5) (542 events)



(b) SSP 5(8.5) (643 events)

Figure 4.1: Heatwave duration obtained from the model output KACE-1-0-G (r2i1p1f1)

4.2.2 NHPP

The expressions of the likelihood functions for the estimation of the parameters are discussed in Chapter 2, and the specific forms of the rate function and the distribution of the HW duration are presented below.

4.2.2.1 Rate function

For the NHPP rates the log-linear model is used as follows:

$$\lambda(t) = exp(\lambda_0 + \lambda_1 t)\ (per\ year) \tag{4.2}$$

The estimation process followed from Section 2.4.2.1 to obtain the parametersλ_0 and λ_1.

4.2.2.2 HW durations

For the time-dependent shock heights, a Weibull distribution with time-dependent shape and scale parameters has been used, where $F(x;t)$ and $f(x;t)$ denote the CDF and PDF, respectively.

$$F_{X(t)}(x;t) = Weibull(\alpha(t), \beta(t)) = 1 - exp\left[-\left(\frac{x}{\beta(t)}\right)^{\alpha(t)}\right] \tag{4.3}$$

Both the shape and scale parameters are taken to be exponential to once again harness the benefits in the statistical estimation process since, we do not need to apply any constraints on these parameters during the optimization process.

$$\begin{aligned} \alpha(t) &= exp(\alpha_0 + \alpha_1 t) \\ \beta(t) &= exp(\beta_0 + \beta_1 t)\ (days) \end{aligned} \tag{4.4}$$

The likelihood function used for this parameters estimation is given by Equation (2.56). It may be noted that making both the shape and scale parameters time-dependent increases

Table 4.1: Estimated parameters of the NHPP model and NS Gumbel distribution

SSP scenrios	NHPP						NS-Gumbel			
	Rate		Duration distribution				Location		Scale	
	λ_0	λ_1	α_0	α_1	β_0	β_1	μ_0	μ_1	σ_0	σ_1
SSP5	0.8871	0.0173	0.7449	-0.0101	1.1707	0.0128	0.9251	0.0262	0.1495	0.0324
SSP2	0.8101	0.0135	0.6839	-0.0048	1.2596	0.0052	1.1035	0.0108	0.3369	0.0147
SSP1	0.8106	0.0064	0.5944	-0.0008	1.3066	0.0020	1.1679	0.0039	0.4866	0.0048

the complexity of the problem by increasing the number of parameters but at the same time increases the flexibility of the distribution to accommodate any trends in the data.

4.3 Results

4.3.1 Estimated Parameters

The MLE estimates of the various parameters in the NS Gumbel model and the NHPP model are tabulated in Table 4.1.

From Figure 4.2, it can be seen that there is a strong non-stationarity in the occurrence of the extreme heat events depending the SSP scenario. The analysis suggests that such events can become up to 5 times more frequent toward the end of the century for the SSP5 (8.5) scenario.

Similarly, there would be a significant increase in the duration of the heatwave depending on the SSP scenario, as indicated by the ML estimates of the time-dependent distribution of the duration of the heatwave. The increments in the average duration for various scenarios are presented in Figure 4.3. For example, the average duration of heatwaves can increase from around 3 days to close to 10 days by 2100 for the SSP5 scenario.

4.3.2 Maximum value distributions

The annual maximum duration of heatwaves is estimated using the NS Gumbel method and the NHPP model.

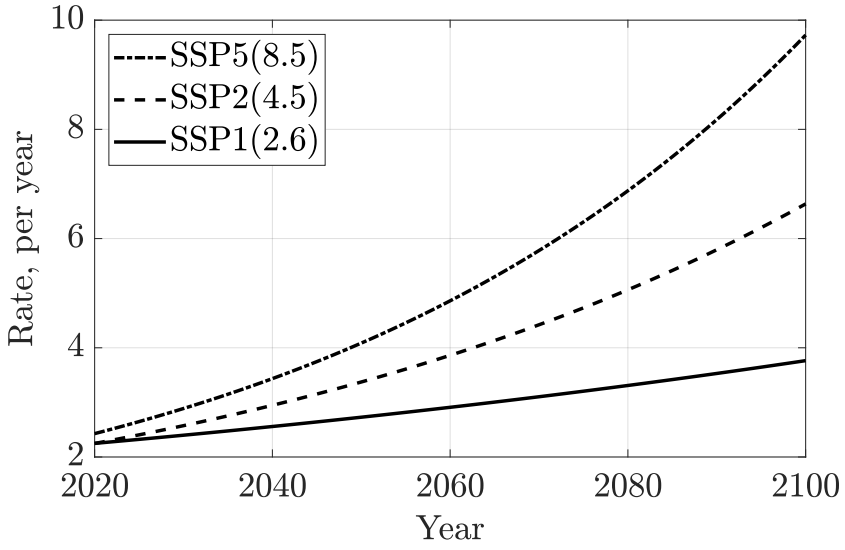


Figure 4.2: Rate of occurrence heatwave events

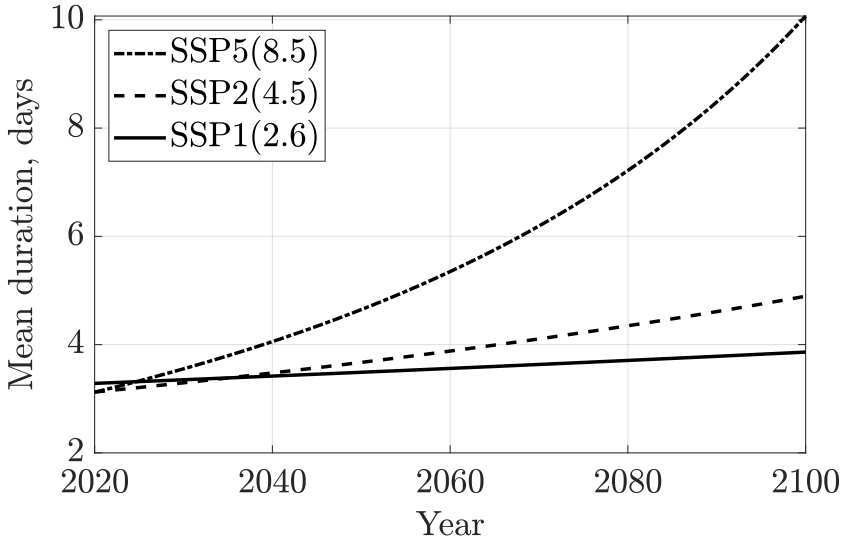


Figure 4.3: Mean duration of heatwave events

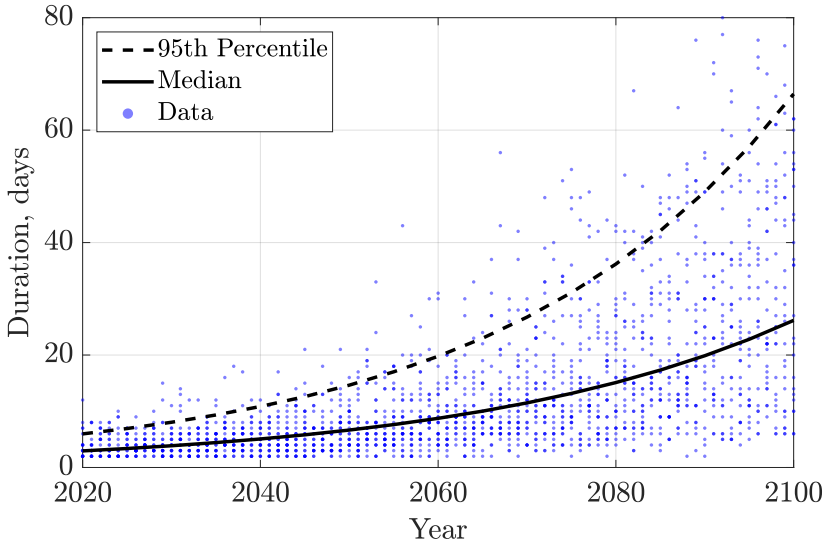


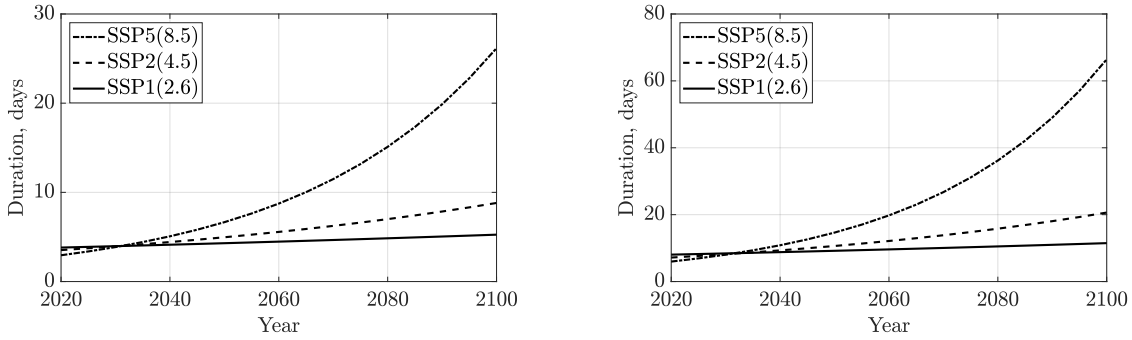
Figure 4.4: Estimated Gumbel EV percentiles of the annual maximum heatwave duration for SSP5 (8.5) scenario

The NS Gumbel estimation indicates that the SSP5 scenario would lead to much higher increases in the duration of heatwave events by 2100 and this is reflected in all the percentiles of the extreme value distributions. The fit of the estimated distribution is shown in Figure 4.4.

For reference, the median and the 95th percentiles of the extreme value distributions for all scenarios are plotted in Figure 4.5. For median of the annual maximum duration can be expected to increase by around 5% to 500% depending on the future emission scenarios, and similar increases can be seen in the higher percentiles as well.

The fit of the estimated NHPP along with the data of the annual maxima of all the model ensembles for the SSP5 (8.5) scenario in Figure 4.6.

Figure 4.7 suggests that the estimates of the annual maximum heatwave duration estimated from the stochastic process model shows similar increments over time as compared to the NS Gumbel estimation.



(a) Median (b) 95th percentile

Figure 4.5: The median and the 95th percentile of the annual EVD obtained from the NS Gumbel analysis.

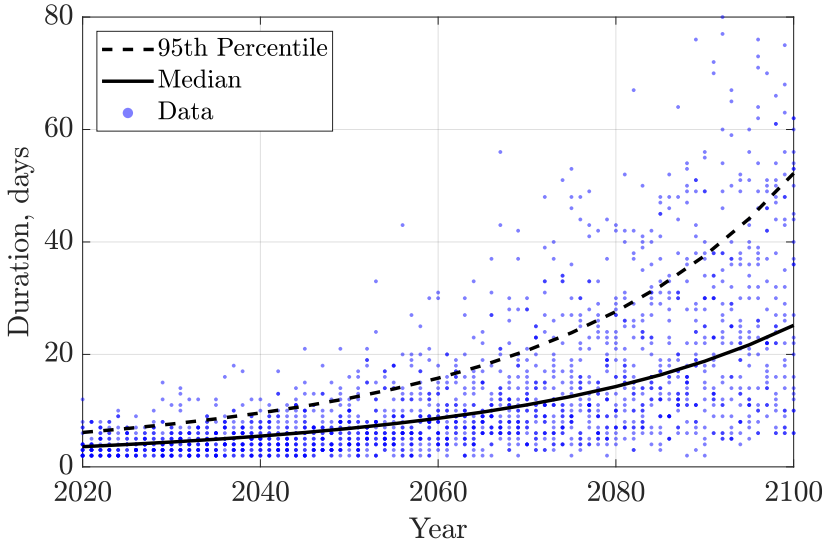
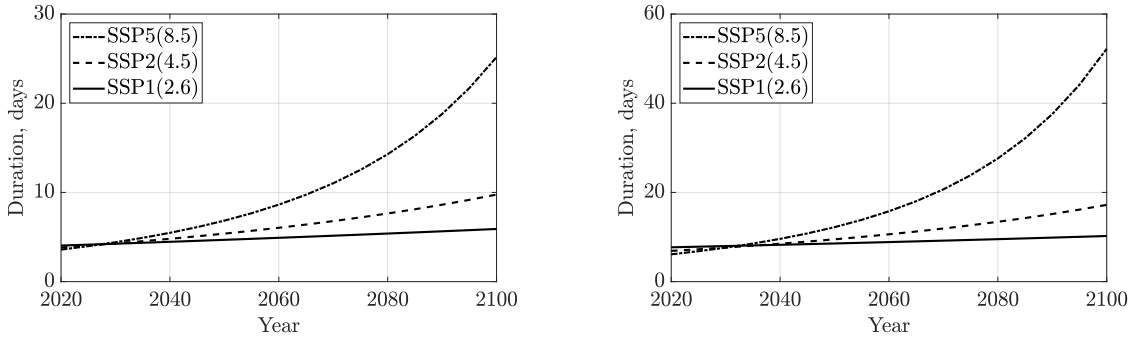


Figure 4.6: Estimated NHPP percentiles of the annual maximum heatwave duration for SSP5 (8.5) scenario



(a) Median

(b) 95th percentile

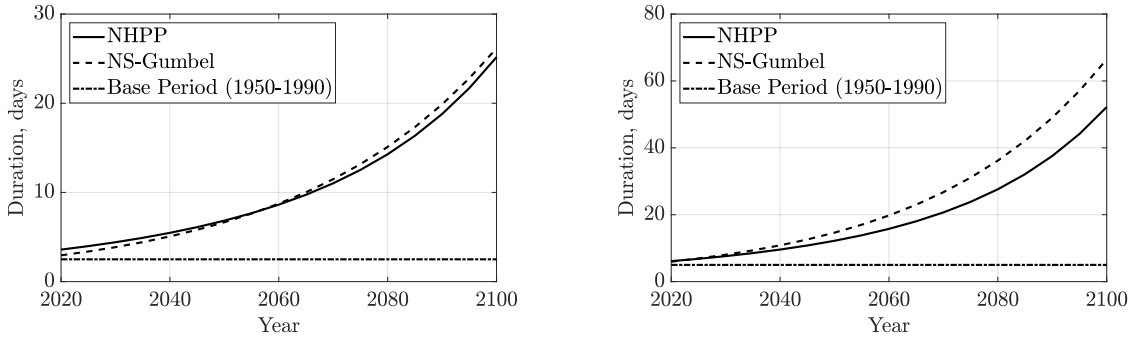
Figure 4.7: The median and the 95th percentile of the annual maximum value distribution obtained from the NHPP analysis.

Here, it can be observed that for the SSP5 scenario the estimated percentiles of the heatwave duration are much higher i.e. of the order of 50 days which may seem to be impractical. However, it may be noted that since most CMIP6 model outputs have a warmer bias for regions of Canada [76, 48], the duration of the estimated heatwaves are likely higher than what can be expected.

4.3.2.1 Comparison

When a comparison is drawn between the annual maximum distributions obtained from the NS Gumbel approach and that stochastic model approach by extracting the several percentiles over the period 2020-2100, it is found that the estimates are quite close to each other for the median estimates; however, it is found that for the 95th percentile, the NHPP underestimates the durations slightly as shown in Figure 4.8.

This difference arises from the difference in the modelling and the choice of rate and intensity functions in the NHPP model, and therefore, choosing other functional forms for rate and duration might lead to slightly different estimates. As speculation, one might choose to fit multiple models to the dataset to estimate a variety of rates and duration, followed by model averaging of the results to reduce this bias.



(a) Median

(b) 95th percentile

Figure 4.8: The median and the 95th percentile of the annual maximum value distributions obtained from the NS Gumbel and NHPP model for SSP5(8.5) scenario.

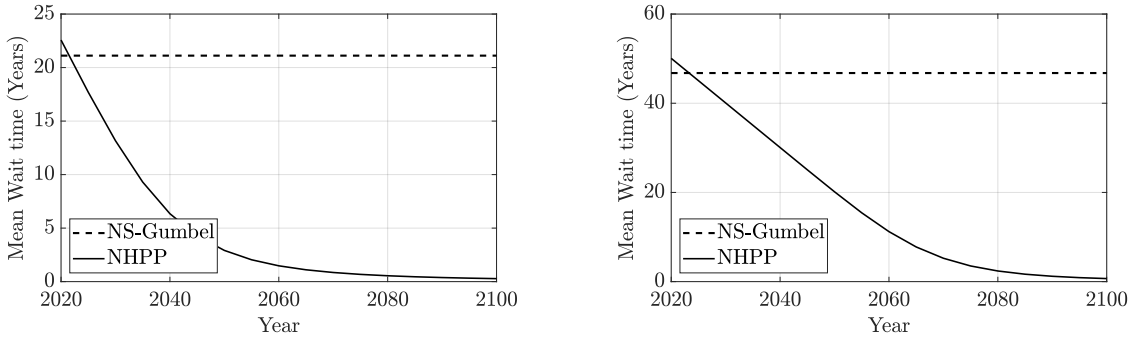
4.3.3 Mean waiting times

The waiting times of high duration heatwaves were calculated following the same principles outlined in Chapter 3. For this demonstration, the duration of 9 days and 18 days was chosen as the return levels, since they roughly correspond to waiting times close to 20 years and 50 years in 2020 corresponding to the SSP5(8.5) scenario using Equation (2.47). The first waiting time was calculated for the NS Gumbel model [97] and to provide the comparison. Figure 4.9 shows that for both the return levels, the waiting times will decrease in number over time which is reflected in the waiting time definition of the EV models.

4.4 Conclusions

Similar to the analysis in Chapter 3, another case study was presented in this chapter, in which the heat waves were modelled using stochastic process models. The commencement of the heat waves was considered the arrival times and the duration of the heatwaves was taken as the shock heights.

Some potential arguments against the usage of extreme value distribution to specifically model the heatwave duration can be the fact that the asymptotic nature of the EV model



(a) Return level, 9 days

(b) Return level, 18 days

Figure 4.9: The mean waiting times to the next heatwave event of given return level.

may not be satisfied since a given year does not witness a high number of heatwaves. However, this can be readily modelled using the stochastic process models discussed in this chapter. Hence, instead of the asymptotic theories of the EVDs, it is far more practical to estimate the annual maximum of the duration obtained through the stochastic process models.

It must be noted that the situation would be different if we just wanted to model the maximum temperature reached in a given year, in which case the Gumbel models would satisfy the underlying asymptotic conditions, and equivalent stochastic process models would also provide a good representation of the annual maxima. However, in this situation to better demonstrate the applicability of the stochastic process model, we selected the secondary but very important aspect of an extreme heat event which is its duration and modelled it as the shock height associated to the NHPP arrival process.

The stochastic process modelling of these kinds of climatic hazards is still in its developing stage, and with better understanding of these kinds of processes, we can better model other hazards associated with prolonged spells of high temperatures such as drought events, water crisis, demands on the energy systems for cooling, and coupled with humidity information, these analyses can provide deep insights about the trends in heat-related health hazards and mortality.

Although the shock process models were sufficient to model the heatwave events in this

case since the duration of the heatwaves was much less compared to the inter-arrival times, but for locations where prolonged high temperatures are expected such that the duration of the heat waves and inter-arrival time of these heatwaves become comparable, it will be more practical to model those events using non-stationary pulse processes and develop associated theories.

Another hypothesis regarding heat-related phenomena is that as global warming progresses and temperatures gradually increase, the population in affected regions will adapt to the new thermal conditions. Consequently, the temperature thresholds that define a heat wave may change over time. Therefore, the predicted duration of extreme heatwaves towards the end of the century could be modified, contingent upon future revisions of these definitions.

So far, in Chapters 3 and 4, we have discussed the impacts of climate change on hazard processes and modelled them using the stochastic process models. It may be noted that, apart from climate-driven hazards, other loading processes that are expected to show changes in rates and intensities can be identically modelled to find maxima over any given period (not necessarily annual) and perform time-dependent reliability analysis of structures. To continue the discussion on climate change, the next chapter discusses some impacts of the changing climate on the degradation of concrete structures, more particularly bridges, by means of simulations and forecasts the bridge condition states in changing climates.

Chapter 5

Concrete Degradation in Changing Climate using Markov Process

5.1 Introduction

Does climate change (CC) threaten the durability of infrastructure systems? Different infrastructure systems will surely respond in different ways due to the multifaceted nature of CC. In addition to the fact that CC is predicted to promote an increase in extreme loading on the structures by increasing precipitation and wind speeds, the durability of the structures can be affected due to enhanced degradation motivated by the rise in temperature. One of the related concerns is how the changing climate will affect the prediction of the condition of these systems. Here, let us begin the discussion with some key aspects of the degradation process in concrete structures, since concrete is one of the mass-produced building materials and constitutes a significant fraction of the major civil infrastructure systems. Here, if we focus on bridges, most bridge maintenance systems use Markov chain [35] models in which the transition probabilities are estimated using the inspection data. Due to their simplicity, Markov models have gained significant popularity for predicting bridge conditions in the future [26, 86, 122, 121, 56]. In this study, we investigate the impact of changing weather variables due to CC on these Markov transition probabilities for concrete structures in various regions of Canada and for different carbon emission

scenarios.

In the following section, concrete degradation models developed over time, based on physical and chemical processes, and empirical models based on experimental studies, which are used in this study, have been discussed.

5.2 Literature

Studies on durability suggest that the time to the onset of corrosion of the rebars in reinforced concrete (RC) structures is sensitive to factors such as chloride concentrations on the free concrete surface and the threshold chloride concentration at the reinforcement levels, the chloride diffusivity, and most importantly, the depth of the concrete cover [124, 18, 28, 66]. For example, with the other parameters the same, a 50% decrease in chloride diffusivity doubles the corrosion initiation time. In contrast, the same increase in concrete cover will increase the time by 125% [133]. Therefore, the high uncertainties in the former three quantities (assuming that the cover is relatively specific for a given structure) propagate at the corrosion initiation times.

In addition, some of these parameters in this process depend on environmental conditions such as temperature and relative humidity, which implies that changing climate will also impact the degradation process. A probabilistic study has shown that the critical chloride concentration at the reinforcement surface will reduce by 20-40% across Canada by the year 2100 for an RCP8.5 carbon emission scenario. The corrosion initiation time for high performance RC structures and ordinary Portland concrete is also expected to be reduced by 33% and 50%, respectively [100, 42, 41]. Another study has suggested that the durability of RC structures in marine environments will be most affected by climate change with a reduction of 2% to 18% in useful life by 2100 [9]. Once corrosion is initiated, the progress of corrosion leads to the formation of voluminous by-products in the concrete matrix that build up internal pressure, eventually leading to cracks on the surface of the concrete[19, 53]. Experimental studies showed that the corrosion rate can increase to 117. 14% when the temperature increases from 275 to 310 K while maintaining constant relative humidity. Similarly, the corrosion rate can also increase by 107.2% when relative humidity

increases from 60% to 80% [67].

To model the natural degradation of the bridges, i.e. without interventions and repairs, Markov models are widely used by researchers and bridge management systems. Depending on the bridge maintenance systems and the type of rating used to denote the condition of the bridges, several bridge condition states can be defined. For example, in Ontario, Canada, the bridge conditions are stated in terms of an index called the bridge condition index (range: 0-100) [80], which considers the cost of repairing the damages to the cost of replacing the bridge. In this case, the condition states can be defined by partitioning the range of indices into several segments as done in [132, 112]. In the Netherlands, bridge conditions are classified into six categories based on the severity of the damage, although the metric of measuring severity is not distinct[56]. Similarly, in the Pontis Bridge management system in the United States, around five condition states are defined based on the extent of repairs [40, 36]. However, in these kinds of condition rating system, the structural behavior of bridge elements should be clearly reflected, as pointed out in [61]. In another distinctive approach, we can consider the durability limit states, defined in terms of the visible and measurable crack widths. Based on these durability limit states, the condition states can also be defined[26]. Although there is some ambiguity in the limiting value of the limiting crack width as discussed in section 5.6.3, researchers can choose conservative values or the ones prescribed by the design codes for the region. The methods of estimating Markov transition probabilities have become refined over time, and researchers are currently mainly reliant on methods such as maximum likelihood or constrained minimization of squared errors in predicted states [25, 17]. Sometimes, non-homogeneous Markov models are used to track the age dependence on the transition probabilities, and the transition probabilities can be obtained as a function of age [36, 20]. However, this methodology can be applied when the environmental conditions remain stationary. In the context of changing climate, there have not been enough studies to capture the non-stationarity due to aging and changing climate.

Therefore, little literature is available on the use of the Markov process to assess bridge condition in changing climate situations. The following section begins with a brief discussion of the relevance of climate change in the degradation process for RC structures.

5.3 Research objectives

The following objectives are intended to be accomplished in this chapter. It might be noted here that if the climate conditions are modelled here as done in Chapters 3 and 4, then we would have two time-scales involved in the modelling, first, the time-scale of the climate change and second, the time scale of the structural degradation that initiates at the end of the construction of the structure. Therefore, to study the changes in the Markov transition probabilities, it was important that we assume piece-wise stationarity in the climatic conditions over smaller intervals, here taken as 20 years, and analyze the degradation processes under the weather conditions corresponding to that period. Then it would be easier to understand how these transition probabilities for the degradation processes evolve over time due to changing climatic conditions.

- Segment the time axis into 20-year periods until 2100, and for each segment, using stochastic process models, generate time-series realizations for weather variables like temperature and relative humidity that account for the seasonal variations and the projected changes due to CC different emission scenarios in different regions of Canada.
- Using the realizations for each time segment, simulate degradation paths using the degradation models obtained from the literature.
- Define the Markov condition states and map the degradation path in terms of the defined Markov states.
- Estimate the Markov transition probabilities from the simulated samples and study the effect of CC on these probabilities. After that, it is intended to demonstrate their usage by employing illustrative examples.

5.4 Concrete degradation process and climate change

Concrete degradation is a complex process that depends on temperature, like most other physicochemical process. In addition, relative humidity in the atmosphere and carbon

dioxide concentration also affects the degradation process significantly. Therefore, CC is expected to play an essential role in altering the life expectancy of RC infrastructure systems. Some critical aspects of changing climate relevant to this study and the stages of concrete degradation and their governing models are discussed briefly in this section.

5.4.1 Climate projections

The temperature projections for some important provinces in Canada over the current century are given in fig. 5.1. The results from the simulated models suggest that the relative humidity will not be affected much over the century [14]. The concentration of carbon dioxide in the atmosphere, which affects the carbonation process in concrete structures, and depending on the emission scenario, is expected to increase from 400 ppm in 2020 to 500 ppm (for RCP4.5) and 950 ppm (for RCP8.5) in 2100.

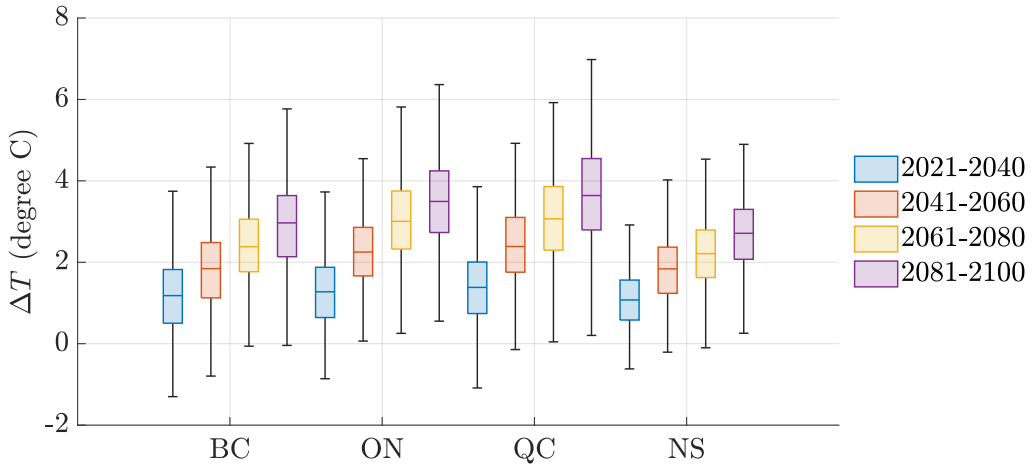
The following sections discuss the various processes related to the degradation of reinforced concrete structures and their dependence on variables such as temperature, relative humidity, and CO_2 concentration based on chemical laws and empirical relations obtained from experiments.

5.4.2 Chloride diffusion

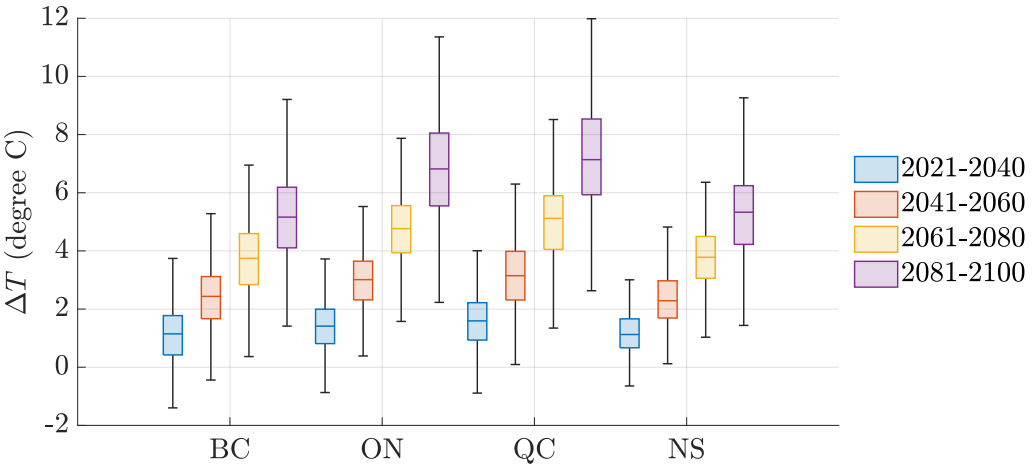
The free chloride ingresses from the free surface of the concrete to the matrix following the diffusion process. The concentration of Cl^-, $(C_{Cl^-}(\mathbf{x}, t))$ at any time,(t) and at any point, $(\mathbf{x})$ in the concrete mass can be obtained by solving Fick's law of diffusion as follows.

$$\frac{\partial C_{Cl^-}(\mathbf{x}, t)}{\partial t} = \nabla^2 \left(D_{Cl^-} \cdot C_{Cl^-}(\mathbf{x}, t) \right) \tag{5.1}$$

where, D_{Cl^-} is the chloride diffusion coefficient, and $\nabla^2(\cdot)$ is the Laplacian. The initial and boundary conditions for solving the above equation have to be specified as $C_{Cl^-}(\mathbf{x}, 0) = C_i(\mathbf{x})$ and $C_{Cl^-}(\mathbf{x} = \mathbf{x_0}, t) = C_b(\mathbf{x_0}, t)$. The diffusion coefficient can be considered a function of time and space. In most situations, it is considered constant for simplicity, especially since chloride diffusion is a slow process.



(a) RCP 4.5



(b) RCP 8.5

Figure 5.1: Annual average temperature increase in different provinces (BC: British Columbia, ON: Ontario, QC: Quebec, NS: Nova Scotia) for different Carbon emission scenarios [2]

Diffusion coefficient and temperature The effect of temperature on the Chloride diffusion process is well studied [100, 19, 116]. The diffusion coefficient or the rate of Cl^- depends on temperature based on the Arrhenius' law:

$$D_{Cl^-}(T) = D_{Cl^-_}(T_0) exp\left[\frac{E_{Cl^-(D)}}{R}\left(\frac{1}{T_0} - \frac{1}{T}\right)\right] \tag{5.2}$$

where, T_0 is a reference temperature (here 296 K), and $E_{Cl^-(D)}$ is the activation energy of the chloride diffusion process, and R is the universal gas constant. Equation (5.2) suggests that the expected temperature increase will accelerate the process of chloride diffusion in the concrete mass.

5.4.3 Carbonation

The corrosion of the reinforcement occurs also if the depth of carbonation reaches the reinforcement surface. With increasing emissions of greenhouse gases, the concentration of carbon dioxide in the atmosphere is gradually expected to increase over time. The predicted increase CO_2 levels in the atmosphere and temperature will directly influence the carbonation rates in concrete. The depth of carbonation is given by the square-root law as follows.

$$x_{CO_2} = K_{CO_2}\sqrt{t} \tag{5.3}$$

where, $x_{CO_2}, (mm)$ is the depth of carbonation and $K_{CO_2}, (mm/\sqrt{yr})$ is the carbonation rate. The carbonation rate is a function of the environmental factors like temperature (T, K), relative humidity $(RH, (\%))$ and the CO_2 concentration in the atmosphere, $(C_{CO_2}, (\%))$, and material composition of the concrete such as cement content, $(C_e, (kg/m^3))$, admixture content, $(F, (kg/m^3))$ and water-cement ratio (wcr). The following model for the carbonation rate proposed and calibrated by [65] is used here.

$$K_{CO_2} = K_x\sqrt{365}(wcr - 0.106)(C_e - 508.351C_e - 1195.625)(F + 112.624) \\ (RH^2 - 125.41RH + 2351.8)(T - 277.66) \cdot C_{CO_2}^{0.538} \quad (5.4)$$

K_x is an influencing factor in the carbonation process. The values and units of the various quantities used in eq. (5.4) are provided in section 5.6.1. However, it may be noted that carbonation is a slower process than chloride diffusion and is often not the governing process in reinforcement corrosion initiation.

5.4.4 Reinforcement corrosion

Once the chloride concentration on the reinforcement surface reaches a critical value, the passive protective layer on the steel surface breaks and initiates the corrosion process. The critical concentration (C_{cr}) depends on the temperature and decreases with increasing temperature and therefore initiates corrosion at lower chloride levels [100].

$$C_{cr}(T) = C_{cr}(T_0)exp\left[\frac{E_{Cl^-(conc+steel)}}{R}\left(\frac{1}{T} - \frac{1}{T_0}\right)\right] \quad (5.5)$$

where, $C_{cr}(T_0)$ is the threshold concentration at a reference temperature T_0 and $E_{Cl^-(conc+steel)}$ is the activation energy to initiate corrosion in concrete and steel medium. The corrosion can also be initiated if the carbonation depth reaches the steel surface. Let the time taken for the chloride concentration at the steel surface to reach the critical concentration be denoted as $t_{i(Cl^-)}$ and the time taken for the carbonation depth to reach the depth of concrete cover be denoted as $t_{i(CO_2)}$. So, whichever of the two processes occurs earlier decides the time of corrosion initiation, t_i, i.e.

$$t_i = min\{t_{i(Cl^-)}, t_{i(CO_2)}\} \quad (5.6)$$

The rate of steel corrosion and rust expansion is based on Faraday's law [19]. Experimental studies have developed several relations between the corrosion rate and the differ-

ent environmental factors. The following corrosion rate has been adopted from [67] where the authors have presented empirical relations of the corrosion rate, $(i_c, \mu A/cm^2)$ with temperature (T, K), relative humidity, $(RH, \%)$, which are some of the critical variables concerning climate change and other important parameters such as concrete cover depth $d_c(mm)$, water-cement ratio [124] and total chloride concentration $((C_{\text{Cl}^-})_{total}, kg/m^3)$.

$$i_c(t) = 1.3\frac{(1-wcr)^{-1.64}}{\sqrt[3]{(1+t)d_c}} exp\left[1.23 + 0.618ln(C_{\text{Cl}^-}(t))_{total} - \frac{3034}{T(2.5+RH)}\right] \tag{5.7}$$

where, the total Cl^- concentration can be written as:

$$(C_{\text{Cl}^-})_{total} = (C_{\text{Cl}^-})_{free} + (C_{\text{Cl}^-})_{bound} \tag{5.8}$$

The free Chloride concentration, $(C_{\text{Cl}^-})_{free}$ at the reinforcement level can be obtained by solving eq. (5.1) and the bound Chloride concentration, $(C_{\text{Cl}^-})_{bound}$, which can be obtained using the relation, $(C_{\text{Cl}^-})_{bound} = 1.23 \cdot (C_{\text{Cl}^-})_{free}$ as proposed by [72].

5.4.5 Concrete Cracking

With the onset of corrosion and formation of rust, there is a pressure buildup in the concrete matrix surrounding the reinforcement and within a short time, the first cracks or the hairline cracks (with crack width around 0.05mm) appear. Here, the time of first cracking is denoted as $T_{cr(1)}$. After that, with the progress of corrosion, the crack width increases depending on the corrosion rate, i_c. The models for time of first cracking, $T_{cr(1)}$ and the rate of increase, r_c in the crack-width based on experimental data is adopted from [74] as follows:

$$t_{cr(1)} = k_R \cdot \frac{i_{c(exp)}}{i_{c(real)}} t_{cr(exp)} + ti \tag{5.9}$$

where, $t_{cr(exp)}$ is the experimental crack initiation time (Table 1 in [74]) for 40 MPa concrete, k_R is a correction factor that depends on the ratio of experimental corrosion rate,

$i_{c(exp)}$ in the accelerated corrosion tests (Table 1 in [74]) to the real corrosion rates, $i_{c(real)}$ obtained from eq. (5.7) is taken as 0.25 (based on the range of possible values for $i_{c(real)}$) and t_i is the time of corrosion (eq. (5.6)).

$$w(t) = w_0 + \int_0^t r_c(t)dt \tag{5.10}$$

where, $w(t)$ is the crack width at time t, w_0 is the first cracking width (taken as 0.05mm) and $r_c(t)$ is the rate of crack-width growth. Details about $r_c(t)$ are provided in the appendix. It may be noted here that in eq. (5.10), t starts from the time of first cracking.

So far, the deterministic models of concrete degradation have been explained sequentially, affording us several critical times that reflect the structural states. However, due to the inherent uncertainties in the parameters of the physical process as well as the uncertainties in the environmental conditions, predicting the state of the structures in the future requires a probabilistic framework which will be accomplished through the uncertainty propagation and modelling the states of the system using Markov process models.

5.5 Rate of crack-width increase

In [74], the results of accelerated corrosion have been presented and are appropriately adopted in this study. The rate of crack propagation, $r_c, (mm/yr)$ is given as follows:

$$r_c(t) = 7.008 \frac{i_{c(real)}(t)}{i_{c(exp)}} e^{-1.7\psi} \tag{5.11}$$

where $i_{c(real)}$ is the real rate of corrosion and $i_{c(exp)}$ is the experimental rate of corrosion (which was specified as 100 $\mu A/cm^2$). The "cover cracking parameter", ψ is depended on the depth of the cover, $d_c, (mm)$, reinforcement diameter, $d_b, (mm)$ and the tensile strength of concrete, f_t as follows.

$$\psi = \frac{d_c}{d_b f_t}, \quad 0.1 \leq \psi \leq 1.0 \tag{5.12}$$

The rate expression needs to be corrected to account for the differences in the corrosion rates in the experimental setup and real conditions and some cover depth confinement, which gives the following expression:

$$r_c(t) = 7.008 \frac{k_R}{k_c} \frac{i_{c(real)}(t)}{i_{c(exp)}} e^{-1.7\psi} \tag{5.13}$$

where k_R is the 'loading correction factor that is related to the ratio $\frac{i_{c(real)}}{i_{c(exp)}}$ as follows:

$$k_R = 0.95 \left[exp\left(0.3 \frac{i_{c(exp)}}{i_{c(real)}}\right) - \frac{i_{c(exp)}}{2500 i_{c(real)}} + 0.3 \right], \quad k_R \geq 0.25 \tag{5.14}$$

and k_c is the 'confinement factor' with a value of 1 for the reinforcement located in an internal location.

5.6 Analysis

5.6.1 Defining the uncertain parameters

The process of concrete degradation is explained in section 5.4. However, several parameters in each stage of the degradation process are uncertain and need statistical descriptions to obtain the ensemble of the degradation paths. The material parameters of the diffusion process, like the diffusion coefficient, the threshold level of chloride concentration, and the surface chloride concentration, are taken as random variables, and their distributions are taken from the literature and provided in section 5.6.1. Apart from that, in each time segment, the environmental parameters such as the temperature, relative humidity and the concentration of carbon dioxide are taken as a random field whose samples are generated as follows.

Table 5.1: Parameter values

Parameter	Symbol	Distribution	Source
Surface chloride concentration	C_b	Uniform; Range: $2.4 - 4.7 kg/m^3$	Table 1 [133], and [124]
Critical chloride concentration	$C_{cr}(T_0)$	Uniform; Range: $0.30 - 0.71 kg/m^3$	Table 2 [133]
CO_2 concentration	C_{CO_2}	refer to source	[12]
Relative humidity	RH	refer to source	[1]
Temperature increase	ΔT	refer to source	[3]
Chloride diffusion coefficient	$D_{Cl^-}(T_0)$	Uniform; Range: $10^{-12} - 10^{-11}\ m^2/s$	[133]
Influencing factor (Carbonation)	K_x	6.955×10^{-12}	[65]
Water cement ratio	wcr	0.43	[124]
Cement content (M40 grade)	C_e	$510\ kg/m^3$	
Flyash content	F	$90\ kg/m^3$	(15% of total powder content)

The time axis is segmented into 20-year intervals until the year 2100. Then the process $K(\theta, t)$, representing the weather variable (say temperature, T) is given as:

$$K_T(\theta, t) = k_{T_0}(\theta, t) + \Delta T(\theta) + \xi(t) \tag{5.15}$$

where, θ denoting the set of deterministic and random parameters involved in the process, $k_{T_0}(t)$ is the mean of the stochastic process for the reference time on which the temperature increase, ΔT is predicted and $\xi(t)$ is a zero-mean stochastic process giving the fluctuations over the mean process. The seasonal variations of the weather variables are modelled using a sinusoidal mean function.

$$k_{T_0}(\theta, t) = a + b \cdot sin\left[\omega t + \phi\right] \tag{5.16}$$

where the values of the parameters, $\{a, b, \omega, \phi\}$ are estimated from the historical data of the reference period [9]. ΔT is the random variable for the temperature increase corresponding to the time interval. Based on the percentile values obtained from [3], normal distributions are fitted to ΔT to represent the uncertainty in the temperature increase in the different segments of time and $\xi(t)$ is a zero mean process depicting the fluctuations from the mean. These weather variables are simulated using Karhunen–Loève expansion (KLE)

[123, 39, 109], which requires the covariance of the process $K_T(\theta, t)$ and can be easily calculated assuming stationary conditions in the short time intervals as follows:

$$C_{KK}(t_1, t_2) = E[(K_T(\theta, t_1) - E[K_T(\theta, t_1)])((K_T(\theta, t_2) - E[K_T(\theta, t_2)])] \tag{5.17}$$

Using the fact, $E[K_T(\theta, t_1)] = k_{T_0}(\theta, t) + E[\Delta T]$, and using eq. (5.15), the covariance function can be represented as follows:

$$C_{KK}(\tau) = Var(\Delta T) + C_{\xi\xi}(\tau) \tag{5.18}$$

where, τ is the time lag, $(t_1 - t_2)$, $Var(\Delta T)$ is the variance of the temperature increase and $C_{\xi\xi}(\tau)$ is the covariance of the fluctuation process usually given by an exponential function as follows:

$$C_{\xi\xi}(\tau) = a \cdot exp(-|\tau|/\beta) \tag{5.19}$$

where the parameters a and β are estimated from the historical data. Using these results, the process can be represented using KLE as follows:

$$K_T(\theta, t) = E[K_T(\theta, t)] + \sum_{i=1}^{n_d} \sqrt{\lambda_i}\phi_i(t)\eta_i \tag{5.20}$$

where, n_d is the degree of truncation, $\lambda_i' s$ and $\phi_i(t)' s$ are the eigenvalues and normalized eigen-functions of the covariance function $C_{KK}(\tau)$, and η_i are taken standard normal random variables. However, the simulations are performed in discrete time, the numerical formulations of Nystrom integral was used to obtain the normalized eigenvectors of the covariance matrix. This process is exactly similar to conducting a principal component analysis (PCA) where a set of correlated random variables are transformed into a set of uncorrelated random variables and makes it easier to simulate the process.

A realization of the simulated temperature for British Columbia (for RCP8.5 in 2021-2040) is presented in fig. 5.2. Similarly, the other weather variables for all locations, time intervals and emission scenarios were obtained. These temporal uncertainties in the weather variables propagate through the degradation models giving stochastic degradation paths. Using the uncertain parameters in section 5.6.1 and the simulations of weather

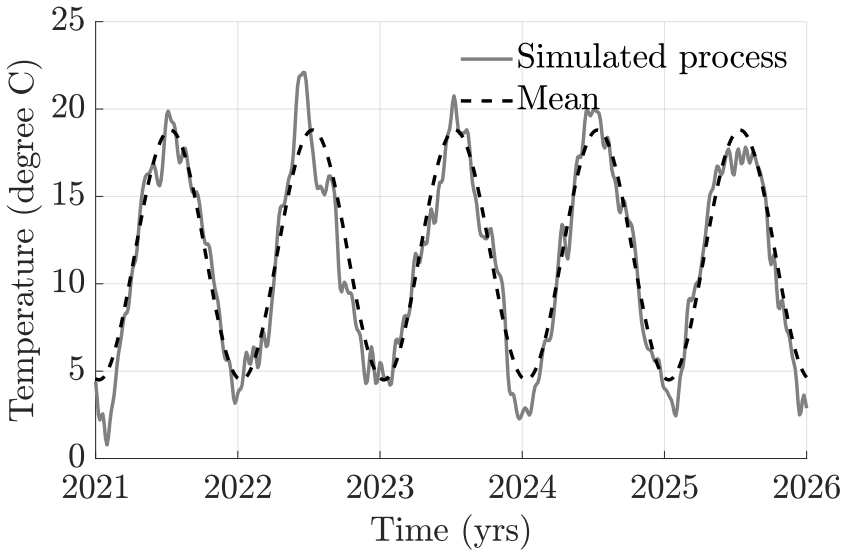


Figure 5.2: Simulated temperature realization in the period 2021-2040

variables, a Monte Carlo simulation was performed to obtain the sample degradation paths with time. The Markov transition probabilities were estimated using the simulated paths as described in the following subsection.

5.6.2 Markov process model

The future state of a system based on the current state of the structure can be predicted using stationary Markov process models, given that the other environmental and loading conditions remain stationary.

Suppose there are $'m'$ possible systems states defined. The probability that a system will be in a particular state S_{n+1} at time t_{n+1}, for a first order Markov process is assumed to depend only on the system state S_n at time t_n and is called the transition probability given as follows.

$$P[S_{n+1} = j | S_n = i] = p_{i,j}, \quad i, j \in \{1, ..., m\} \tag{5.21}$$

Since we want to model the degradation process, we need not account for the interventions and repairs; therefore, $p_{i,j} = 0, \forall\ i < j$. Depending on the inspection intervals, the transition probabilities from one state to another can be calculated so that after an inspection, the state of the system can be predicted till the next inspection or estimate the time when the bridge may require repairs in the future. However, choosing a smaller interval for estimating the transition probabilities is beneficial in case the sojourn time of the system in a certain state is comparatively smaller, in which case larger interval times will tend to overlook the transitions to the immediate next states the system may pass through. For smaller intervals, i.e. $\Delta t = t_{n+1} - t_n$, it is most likely that that state will jump only to the next one or two condition states. Therefore, here we can assume, $p_{i,j} = 0, \forall\ j > i+2$. As a result, the transition probability matrix (TPM) for a Markov chain with six defined states will look as the following, where in total 14 transition probabilities need to be estimated.

$$P = \begin{bmatrix} p_{1,1} & p_{1,2} & p_{1,3} & 0 & 0 & 0 \\ 0 & p_{2,2} & p_{2,3} & p_{2,4} & 0 & 0 \\ 0 & 0 & p_{3,3} & p_{3,4} & p_{3,5} & 0 \\ 0 & 0 & 0 & p_{4,4} & p_{4,5} & p_{4,6} \\ 0 & 0 & 0 & 0 & p_{5,5} & p_{5,6} \\ 0 & 0 & 0 & 0 & 0 & 1 \end{bmatrix} \tag{5.22}$$

with a necessary condition of $p_{i,j} \geq 0,\ \forall\ i, j$ and $\sum_{j=1}^{m} p_{i,j},\ \forall\ i$. Now, due to changing climate conditions, we have divided the time axis into segments of 20 years, and in those segments it is assumed that stationary conditions prevail; therefore, for each segment, the TPM will be estimated with parameters corresponding to the projections of environmental conditions in that time segment. The transition probabilities will be estimated by minimizing the expected states (obtained from the physical degradation models) and the predicted states using the Markov TPM. Details of the estimation procedure are given in the appendix.

5.6.3 Markov condition states and TPM estimation

In visual inspections, the crack-width is a measurable feature that constitutes the durability and serviceability characteristics of RC bridges. The time until any noticeable cracks are present can be assigned a good condition. After the appearance of hairline cracks on the surface, different condition states can be assigned to the bridge depending on the crack width ranges. However, the limiting value of the crack width is not a sacrosanct measure, and different researchers and design codes prescribe different values. Some of the typical crack width values suggested and used by researchers are 0.5mm [115], 1mm [108] and 5mm [61] beyond which the bridge is assumed to have failed in the limits of durability and serviceability and requires major repairs. Therefore, due to the ambiguity in the limiting value of the crack widths, here, a relatively conservative value of the crack width is chosen i.e. a crack width greater than 1 mm is considered a poor condition (S6) and hence the absorbing state in the Markov chain. Another rationale behind choosing crack widths as the deciding parameters of the bridge condition is that the stiffness of the deck at higher loading magnitudes is highly correlated with the mean crack widths as suggested by [130]. It may also be noted that cracking and cracking in concrete can be treated as precursors to more serious structural failures [105, 75]. The different condition states are defined in table 5.2 and depicted in fig. 5.3.

Table 5.2: Markov condition state definitions

Condition definition	Condition state
$w(t) = 0$	S1
$w(t) \in [0.05,\ 0.25)mm$	S2
$w(t) \in [0.25,\ 0.50)mm$	S3
$w(t) \in [0.50,\ 0.75)mm$	S4
$w(t) \in [0.75,\ 1.00)mm$	S5
$w(t) \geq 1.00mm$	S6

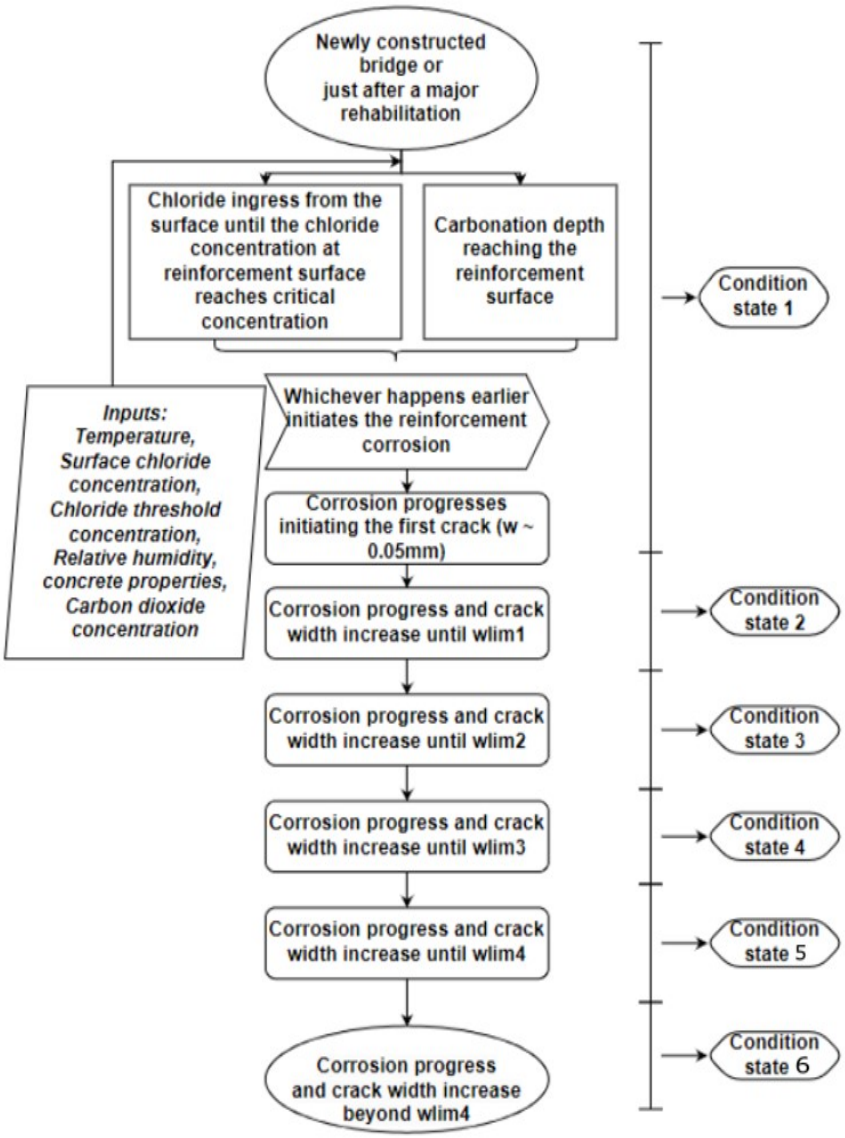


Figure 5.3: Concrete Degradation model and the Condition states

Using these simulated weather time series realizations and the concrete degradation models, a Monte Carlo simulation (MCS) is performed, and sample time-dependent degra-

dation paths are obtained every two years. The path of the condition states was obtained by mapping them to the obtained degradation paths. After that, using the simulated states, the Markov transition probabilities are estimated using the least squared error approximation, as detailed in section 5.7.

5.7 Estimation of Markov transition probabilities

The Markov transition probabilities can be estimated by minimizing the squared error between the true states and the states predicted by the model [61, 17, 35]. Let the true probabilities (given by the proportions of simulated bridges in a given state) be given by the following equation. Let there be a total of n time steps and m states.

$$\pi'_{\mathbf{i}(1\times m)} = \pi'_{\mathbf{i-1}(1\times m)}\mathbf{P}_{(m\times m)} + \epsilon_{i(1\times m)}, \ \forall i \ \in \{1, ..., n\} \tag{5.23}$$

Forming a vector of the error considering all the time steps we have,

$$\epsilon_{(1\times nm)} = \mathbf{p_1}_{(1\times nm)} - \mathbf{p'_0}_{(1\times nm)}\mathbf{\Xi}_{\mathbf{(nm\times nm)}} \tag{5.24}$$

where, $\epsilon = [\epsilon_\mathbf{1}...\epsilon_\mathbf{n}]'$, $\mathbf{p_1} = [\pi_1...\pi_n]'$, $\mathbf{p}_0 = [\pi_0...\pi_{n-1}]'$ and $\mathbf{\Xi}$ is given as follows:

$$\mathbf{\Xi} = \begin{bmatrix} P & 0 & 0 & ... & 0 \\ 0 & P & 0 & ... & 0 \\ \vdots & . & P & . & \vdots \\ . & . & . & \ddots & 0 \\ 0 & . & . & . & P \end{bmatrix} \tag{5.25}$$

Then the transition probabilities in the TPM ($\mathbf{P}$) given in eq. (5.22) can be estimated by minimizing the squared error given by $\epsilon'\epsilon$ with the necessary constraints on the probability values as $0 \leq p_{i,j} \leq 1$ and $\sum_i p_{i,j} = 1, \ \forall \ i$.

5.8 Validation

The problem addressed in this chapter is multi-faceted. So far the concrete degradation models are concerned; these models are drawn from existing literature, wherein their coefficients stem from meticulously derived experimental outcomes and inspection data. Furthermore, they are deemed suitable for application within the range of environmental conditions used here. Under stationary environmental conditions, the methods for estimating transition probabilities align with those of [61, 93]. To establish the validity of our approach, the following validation procedure is adopted. Several experimental studies and data-based studies on the initiation and propagation of corrosion of concrete bridge structures were considered [130, 116, 67, 8]. By replicating the environmental and material parameters stipulated in these prior studies, we estimate the transition probabilities. Subsequently, these probabilities are utilized to construct the distribution of the time of corrosion initiation and the overall lifetime distribution. In certain instances, a comparison is limited to mean lifetimes because of the unavailability of distribution-related information. The results were found to be good compared to those studies. Nonetheless, it is important to acknowledge that precise validation of the degradation process in future scenarios is challenging owing to the evolving climate conditions and the scarcity of analogous studies and relevant data.

5.9 Monte Carlo Simulation cases

In the MCS, 20,000 temperature, relative humidity time series and carbon dioxide concentration samples are generated for each of the 20-year time segments from 2021-2100 (4 segments), RCP4.5 and RCP8.5 emission scenarios for British Columbia, Ontario, Quebec and Nova Scotia, which covers major regions in Canada. The analysis has been performed for three different cover depths of 25mm, 35mm and 60mm, thus totaling 96 cases ($4 \times 2 \times 4 \times 3$).

5.10 Results

Analysis shows that for the two-year interval chosen for the transition probability calculation, only the probabilities of remaining in the same state and jumping to the immediate next condition state, i.e. $p'_{i,i}s$ and $p'_{i,i+1}s$ are significantly greater than zero. Therefore, the TPM for the six states, with the last state being the absorbing state, can be reduced in the following form.

$$P = \begin{bmatrix} p_{1,1} & (1-p_{1,1}) & 0 & 0 & 0 & 0 \\ 0 & p_{2,2} & (1-p_{2,2}) & 0 & 0 & 0 \\ 0 & 0 & p_{3,3} & (1-p_{3,3}) & 0 & 0 \\ 0 & 0 & 0 & p_{4,4} & (1-p_{4,4}) & 0 \\ 0 & 0 & 0 & 0 & p_{5,5} & (1-p_{5,5}) \\ 0 & 0 & 0 & 0 & 0 & 1 \end{bmatrix} \tag{5.26}$$

It has been found that clear cover plays a significant role in the deterioration time; increasing the cover from 25mm to 35mm and 60mm on average increases the probabilities of the system staying in the same states, i.e. $p'_{i,i}s$ by 49% and 80% respectively for RCP8.5. The changing climate accelerates the degradation process in reinforced concrete structures, which has been substantiated by the fact that the probabilities of staying in the same state, i.e., the diagonal terms in the TPM, decrease with time due to increasing temperature and other climatic conditions. For example, in British Columbia, the probability of a bridge deck with a 25mm cover staying in the condition state 1 (good condition) within the next two years reduces from 0.6142 to 0.5596 (for RCP4.5) and 0.4963 (for RCP8.5), which is around 8. 9% and 19. 2% reduction, respectively.

Figure 5.4 shows the variability of the diagonal terms of the TPM over time for the RCP8.5 emission scenario for the different cover depths. The point estimates of the probability values obtained for different cover depth, location, period and emission scenario is provided in the appendix for reference. From fig. 5.4, it is worth noting that the first two diagonal terms of TPM show the most variability with changing climate; this can be attributed to the fact that the initial deterioration phases, i.e. the chloride diffusion phase, is the most sensitive to temperature and in the early stages the corrosion rate is much

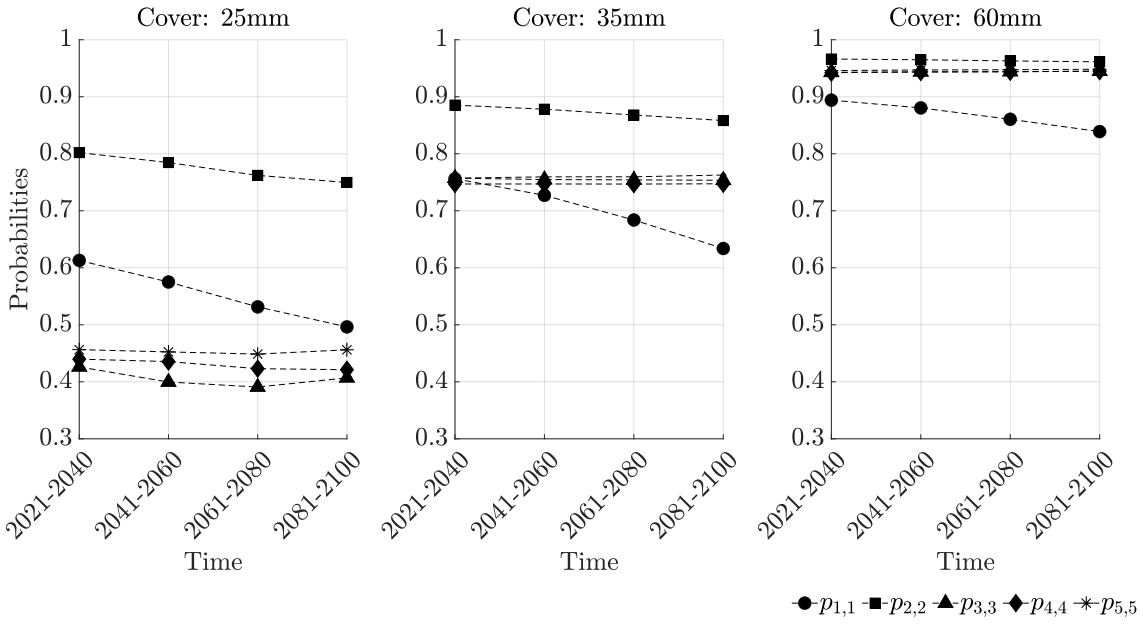


Figure 5.4: Transition probabilities for British Columbia under RCP8.5 emission scenario

higher and attenuates with the progress of corrosion. However, this variability reduces with increase in cover depth.

5.11 Illustrative example

Here different example scenarios are presented to demonstrate the usage of the proposed method and the transition probability matrices obtained to predict the condition states of bridges based on the inspected condition, location of the bridge and year of inspection. For the following cases, it is intended to obtain the expected future condition of the bridges in the next ten years for an emission scenario of RCP8.5.

- Case I: Bridge in British Columbia, in 2025, inspected state: 2 (crack width between 0.05-0.25mm), a good cover of 60mm.

- Case II: Bridge in Ontario, in 2036, inspected state: 3 (crack width between 0.25-0.5mm), poor cover of 25mm.
- Case III: Bridge in Quebec, in 2052, inspected state: 4 (crack width between 0.5-0.75mm), moderate cover of 35mm.

Consider case I, from table B.1, the TPM is constructed using eq. (5.26) and denoted as P. Starting with the initial probability in the year $t_0 = 2025$ as $\pi_0 = [0\ 1\ 0\ 0\ 0\ 0]'$, the probability of each state at a given time can be given as:

$$\pi(t = t_0 + i\delta) = \pi_0' P^i, \quad i = \{0, 1, 2, ... : t \leq 2040\} \tag{5.27}$$

where, $\delta = 2$ years denotes the interval for which the TPMs are estimated. The expected condition and standard deviation can easily be obtained as rules for discrete distributions.

For case II, the process remains the same apart from the fact that here until 2040, the TPM corresponding to the interval 2021-2040 should be used, and then the TPM for the interval 2041-2060 needs to be utilized accordingly, and the same applies for case III.

The expected conditions of the bridge decks for the three cases are plotted in fig. 5.5.

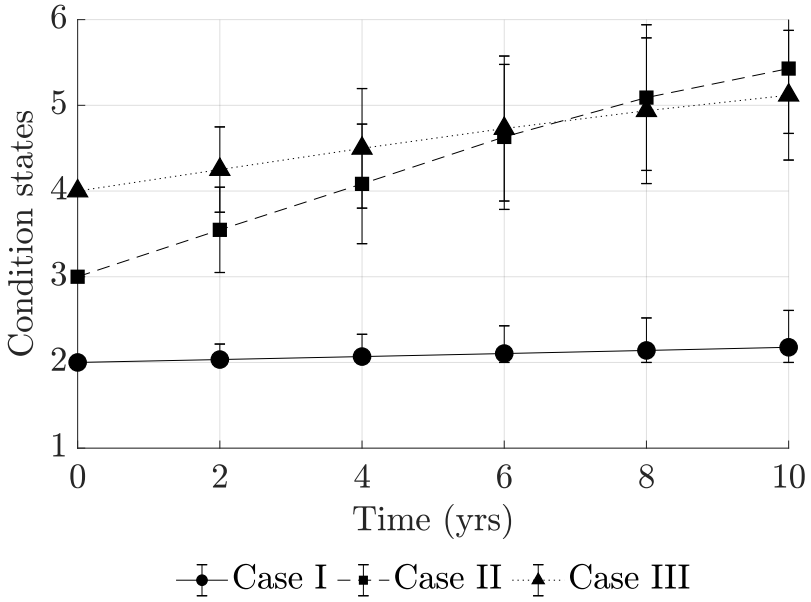


Figure 5.5: Expected states with time for the different cases

5.12 Conclusion

The effect of climate change on the prediction of bridge conditions is studied here. The duration from 2021-2100 is segmented into 20-year duration intervals so that stationary assumptions can be applied in each segment, and the Markov transition probabilities for the bridge condition are estimated. Stochastic process time series realizations of several weather variables such as temperature and relative humidity that directly affect the degradation process in concrete bridges are simulated for different provinces of Canada and RCP4.5 and RCP8.5 emission scenarios based on the projections given by Environment Canada. Concrete degradation models are chosen to simulate the condition of bridges over time using the simulated conditions. The different condition states of the bridges are

defined based on the crack-widths, and the Markov transition probabilities are estimated for each time segment using the least squared error method.

It has been found that the diagonal terms of the transition probabilities, i.e. the probabilities that there will be no jump to the subsequent worse stage, decrease with time for most of the cases, indicating faster degradation with time owing to climate change, and this change is much more significant for the first condition state (good state with no cracks) as compared to other condition states. Good clear cover can significantly retard the degradation process.

Chapter 6

Estimation of Economic Risk

6.1 Introduction

Since a substantial amount of public money is involved in the construction and maintenance of infrastructures, cost optimization has become one of the design criteria recently. In this context, estimating the economic losses due to climate hazards is crucial to answering questions such as whether an investment is economically justified, how much the cost of failures of infrastructure systems can be over a given period, and which of the available alternative designs should be implemented based on economic considerations [46, 50]. With an increase in the global temperature, the frequency and intensity of climate-driven hazards like extreme rainfall, heatwaves, atmospheric river landfalls, high waves in coastal regions and slope failure incidents, the economic impacts of climate change are going to be significant. For optimal design, the economic losses or failure costs are often constructed as a function of the design variable and are minimized to obtain the design values.

Classical cost analysis assumes that the load process is stationary and ample literature has been devoted[10]. However, changes in loading patterns questions the relevance of this assumption. Therefore, cost analysis with stationary assumptions under these scenarios can be erroneous and lead to suboptimal designs.

The implications of climate change on load processes have been discussed in Chapters 1,

3 and 4, and the implications in terms of accelerated degradation have been presented in Chapter 5. Therefore, the time-dependent reliability is expected to decrease over time due to the combined effect of increased degradation rates and the increase of natural loads [73, 52, 96, 38, 11]. For an overall economic analysis of infrastructure systems, inspection, repair, operating, and dismantling costs are generally included [98]. However, these costs, along with the maintenance cost, have little dependence on the design parameters [57] and are not included in this study. This study mainly focuses on the estimation of the economic losses due to climate-driven hazards over a given time, and a major portion of that cost includes the damage cost of the infrastructure systems. This uncertainty in the evaluation of the cost of damage directly depends on the uncertainty in the load process. Therefore, stochastic load process models should be able to capture the trends and patterns of the actual scenario as accurately as possible.

6.1.1 Literature review

The importance of an economic analysis is evident from the perspective of performance-based design. Pertaining to climate change, different adaptive measures can be chosen, e.g. for extreme heatwaves measures such as providing insulation, coatings and maintaining proper window to wall ratio [107, 106]. However, to justify the investments for adaptation measures for strengthening structures against the increasing environmental loads, hazard damage cost analysis can give a critical economic basis. The optimal time for taking the adaptive measures is also dictated by the economic analysis[103], and based on that; the deferral time can be estimated by optimizing the net present or discounted value of the net benefits due to those measures [104]. For structural design, an optimal design can be considered to be the one with minimum discounted cost, with obvious constraints on the safety [91, 118, 49]. In the case of a multi-hazard scenario, cost optimization can be an effective tool for determining the optimal or target reliability for each loading process because different loads have different economic impacts on failure [57, 127, 126]. The expected maintenance cost can be calculated using decision tree analysis, which considers the maintenance actions [33]. In some cases, the annual mean damage is calculated by analyzing the likelihood of hazard events throughout the year. Then, the costs are discounted

to obtain the net present value of the damages to estimate the adaptation measures for the climate-driven hazards [31]. However, most of the literature on cost analysis does not consider the oncoming gradual changes in load patterns due to climate change.

When the occurrence of the hazard events is stationary, i.e. in a stochastic sense, researchers use several classes of stochastic processes to model the randomness in their arrival times and magnitudes. The class of processes for which the loading duration is much smaller than the inter-arrival times can be modelled as shock or point processes, such as the renewal processes, a widely used example of which is the homogeneous Poisson process (HPP). The inter-arrival times of the renewal process are assumed to be identically distributed with a common distribution, and the Renewal theory is used to compute the expected number of failures in a given period. If the hazard arrivals follow a renewal process, the cumulative damage cost at any given time has to be modelled as a compound renewal process, and the total and discounted damage cost for such a failure process can be estimated [85, 55]. The distribution of the economic losses for an HPP can also be obtained using Panjer's recursion [84].

However, as discussed, due to the combined effects of climate change on load and resistance of infrastructure systems, event the failure processes become non-stationary and therefore, the stationary assumption gets challenged in most cases.

In this chapter, we estimated the economic losses due to climate-driven hazards. Changes in the patterns of climate hazards are expected to change, and the nonstationary nature of the hazards can be effectively modelled as a marked-NHPP with time-dependent rate and magnitude. Analytical expressions are developed for the first two moments, that is, the mean and variance, and the distribution of the discounted and undiscounted damage costs or losses incurred by these hazards. When investing in climate adaptation measures, it is important to estimate the reduction in losses due to the measure. Therefore, the formulations are developed such that using different threshold levels of hazards, the statistics of the damage cost can be estimated and provide an economic basis for the justification of the investment in the long run.

6.2 Model of economic loss

The damage cost is incurred when the systems fail under an applied shock load. The failure process $N_f(t_1, t_2)$ is defined as the thinned load process where the events are retained with a probability of loads exceeding the threshold resistance ($R = a$) with a rate $\lambda_f(t)$ (refer to Figure 6.1).

$$\lambda_f(t) = \bar{F_X}(a; t)\, \lambda(t) \tag{6.1}$$

where $\lambda(t)$ is the rate of the load process with load magnitude at time t is given by the distribution $F_X(x; t)$.

At every failure, a cost C_i is incurred, which comprises the cost of material loss, loss of life, and reconstruction. The damage costs $C_i's$ are assumed to be IID with a common distribution $f_C(c)$. The first and second moments of C_i are denoted by μ_C and μ_{2C}. where in the above equation $K_D(t)$ is the discounted losses until t, $N_f(t)$ is the NHPP for failure events, $S_i's$ are the occurrence times of the failure process and ρ is the discount rate. It can often be argued that inflation compensates for interest rates; hence, the discount rate becomes close to zero. Therefore, researchers are often interested in undiscounted losses as:

$$K(t) = C_1 + C_2 + ... + C_{N(t)} \tag{6.2}$$

The cost of damage with discounting can be given as follows [85]:

$$K_D(t) = C_1 e^{-\rho S_1} + C_2 e^{-\rho S_2} + ... + C_{N_f(t)} e^{-\rho S_{N_f(t)}} \tag{6.3}$$

6.3 Case I: IID damage costs

If the damage costs $C_i's$ in Equation (6.2) are considered to be IID then the expressions of the mean, variance, and distribution of the discounted and undiscounted losses or the cumulative damage costs can be derived as follows.

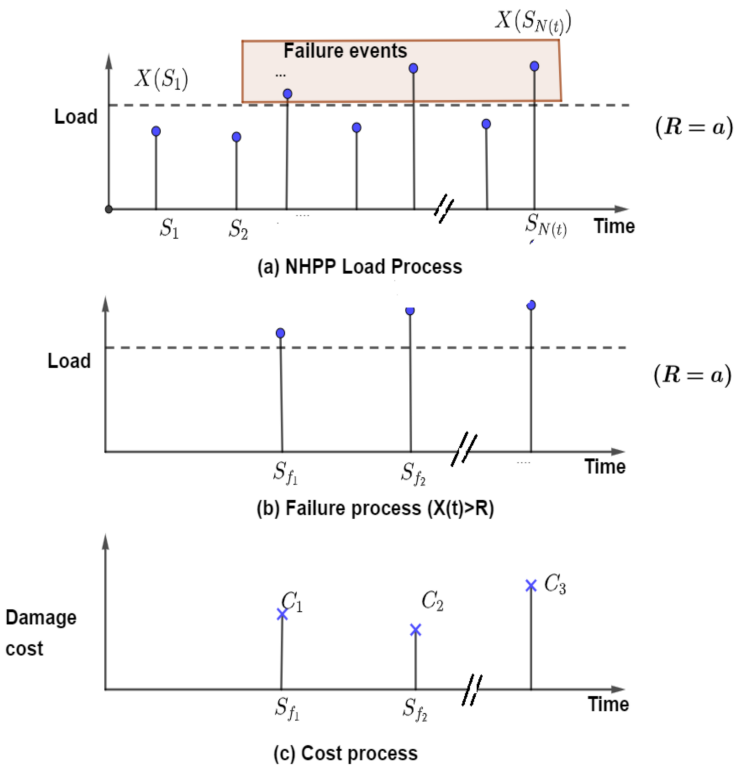


Figure 6.1: The damage cost process

6.3.1 Expected damage cost

The expected value of the discounted damage cost is therefore given as:

$$E[K_D(t)] = \Sigma_{n=1}^{\infty} E[C_1 e^{-\rho S_1} + C_2 e^{-\rho S_2} + ... + C_{N_f(t)} e^{-\rho S_{N(t)}} | N_f(t) = n] P_N(n) \tag{6.4}$$

Since, $C_i's$ are considered IID with mean $E[C]$, in the above equation, the term $E[C_1 e^{-\rho S_1} + C_2 e^{-\rho S_2} + ... + C_{N(t)} e^{-\rho S_{N(t)}} | N(t) = n]$ with further conditioning on the arrival times of the NHPP can be written as:

$$E[C_1 e^{-\rho S_1} + C_2 e^{-\rho S_2} + ... + C_{N(t)} e^{-\rho S_{N(t)}} | N(t) = n]$$
$$= E[C] E[e^{-\rho S_1} + e^{-\rho S_2} + ... + e^{-\rho S_{N(t)}} | N(t) = n] \tag{6.5}$$

$$= E[C] \int ... \int_{0<s_{(1)}<...<s_{(n)}<t} (e^{-\rho s_{(1)}} + e^{-\rho s_{(2)}} + ... + e^{-\rho s_{(n)}})$$
$$f_{s_{(1)}...s_{(n)}}(s_{(1)}, ..., s_{(n)}) ds_{(1)} ... ds_{(n)} \tag{6.6}$$

It may be noted that $E[e^{-\rho s_1} + e^{-\rho s_2} + ... + e^{-\rho s_{N(t)}}]$ is a symmetric function i.e. the function is permutationally invariant. Therefore, using Permutation invariant theorem, the above expression can be simplified as follows:

$$= E[C] \int_0^t n \frac{\lambda_f(s) e^{-\rho s}}{\Lambda_f(t)} ds = n \frac{\mu_C}{\Lambda_f(t)} \int_0^t \lambda_f(s) e^{-\rho s} ds = n \frac{\mu_C}{\Lambda_f(t)} I(\rho, t) \tag{6.7}$$

where, $I(\rho, t) = \int_0^t \lambda_f(s) e^{-\rho s} ds$. Now, substituting Equation (6.7) back to Equa-

tion (6.4), we get the following.

$$E[K_D(t)] = \Sigma_{n=1}^{\infty} n \frac{\mu_C}{\Lambda_f(t)} I(\rho,t) P_N(n) \tag{6.8}$$

$$= \frac{\mu_C}{\Lambda_f(t)} I(\rho,t) \Sigma_{n=1}^{\infty} n P_N(n) \tag{6.9}$$

$$= \frac{\mu_C}{\Lambda_f(t)} I(\rho,t) \Sigma_{n=1}^{\infty} n \frac{[\lambda_f(t)]^n}{n!} e^{-\Lambda_f(t)} \tag{6.10}$$

$$= \mu_C I(\rho,t) \Sigma_{n=1}^{\infty} \frac{n}{\Lambda_f(t)} \frac{[\Lambda_f(t)]^{n-1}}{(n-1)!} e^{-\Lambda_f(t)} \frac{\Lambda_f(t)}{n} \tag{6.11}$$

$$= \mu_C I(\rho,t) \Sigma_{n=0}^{\infty} P_N(n) \tag{6.12}$$

$$= \mu_C I(\rho,t) = \mu_C \int_0^t \lambda_f(s) e^{-\rho s} ds \tag{6.13}$$

For the undiscounted costs, the discounting rate ρ can be taken as zero, then the mean undiscounted damage cost can be calculated as:

$$E[K(t)] = \mu_C \int_0^t \lambda_f(s) ds = \mu_C \Lambda_f(t) \tag{6.14}$$

For an HPP, $\Lambda_f(t)$ can be replaced by $\lambda_f t$ and the following expressions for the mean can be obtained for discounted and undiscounted LCC

$$E[K_D(t)]_{HPP} = \mu_C \lambda_f \int_0^t e^{-\rho s} ds = \frac{\mu_C \lambda_f}{\rho} (1 - e^{-\rho t}) \tag{6.15}$$

$$E[K(t)]_{HPP} = \mu_C \lambda_f t \tag{6.16}$$

6.3.2 Second moment and variance of damage cost

The second moment of the damaged cost can be defined as follows:

$$E[(K_D(t))^2] = \Sigma_{n=1}^{\infty} E[(C_1 e^{-\rho S_1} + C_2 e^{-\rho S_2} + ... + C_{N(t)} e^{-\rho S_{N(t)}})^2 | N(t) = n] P_N(n) \tag{6.17}$$

Following the derivations in the last section, the second moment and hence the variance can be obtained as follows:

$$Var[K_D(t)] = E[(K_D(t))^2] - (E[K_D(t)])^2 \tag{6.18}$$

$$= \mu_{2C} \int_0^t e^{-2\rho s} \lambda_f(s) ds \tag{6.19}$$

The detailed derivation is provided in Appendix C. The undiscounted variance can be obtained by putting $\rho = 0$, in Equation (C.17), as follows:

$$Var[K(t)] = \mu_{2C} \int_0^t \lambda_f(s) ds = \mu_{2C} \Lambda_f(t) \tag{6.20}$$

For an HPP, the variances of the discounted and undiscounted LCC reduces to

$$Var[K_D(t)]_{HPP} = \mu_{2C} \lambda_f \int_0^t e^{-2\rho s} ds = \frac{\mu_{2C} \lambda_f}{2\rho} (1 - e^{-2\rho t}) \tag{6.21}$$

and

$$Var[K(t)]_{HPP} = \mu_{2C} \lambda_f t \tag{6.22}$$

6.3.3 Undiscounted cost

If the discount rate in the previous section is reduced to zero, the case for the non-discounted losses is obtained. The mean gets the well-known form in the literature [94] as given below.

$$E[K(t)] = \mu_C \int_0^t \lambda_f(s) ds = \mu_C \Lambda_f(t) \tag{6.23}$$

where $\Lambda_f(t)$ is the mean value function of the failure process with standard deviation as Equation (6.24).

$$\sigma[K(t)] = \sqrt{\mu_{2C} \int_0^t \lambda_f(s) ds} = \sqrt{\mu_{2C} \Lambda_f(t)} \tag{6.24}$$

6.3.4 Distribution of damage cost

For the undiscounted process, the distribution of the process can also be computed using Panjer's recursion technique. However, in such a case, the probability distribution of the cost $f_C(i\delta)$ is considered discrete with the mass concentrated at multiples of a unit cost δ, and the distribution of the hazard losses is obtained in the form of a probability mass function (PMF). The PMF $f_{K(t)}(i\delta)$ of the undiscounted losses for a Poisson failure process with a constant rate λ_f can be obtained using the following recursive formulation [84]:

$$f_{K(t)}(i\delta) = (\Lambda_f(t)) \sum_{j=1}^{i} \frac{j}{i} f_C(j\delta) f_{K(t)}((i-j)\delta) \tag{6.25}$$

where $i = 1, 2, ...$ and $j = 1, 2, .., i$.

See Appendix C for more details.

6.4 Case II: Time dependent costs

If the damage costs $C_i's$ in Equation (6.2) cannot be considered to be IID, which is a more general scenario, then the expressions of the mean, and variance can be obtained using generalization of the theories given in the previous section, although the distribution cannot be given in a closed form. Here for simplicity of derivations, let us define the discounted damage cost/losses corresponding to a given event be denoted as $Z_i(S_i)$ as follows:

$$Z_i(S_i) = C_i(S_i)e^{-\rho S_i} \tag{6.26}$$

and therefore, the cumulative discounted loss can be given following Equation (6.3) as follows:

$$K_D(t) = \sum_{i}^{N(t)} Z_i(S_i) \tag{6.27}$$

In this section, we present an alternative method to obtain generalized solution of the various statistics of the damage cost by developing simple differential equations following

the definition of NHPP provided in Chapter 2. This method provides a more convenient way to arrive at the closed form expressions of the time-dependent statistics of the net damage costs and the other benefit of using this method is that it can be solved using any standard differential equation solver in the commercial packages.

We begin our discussion by obtaining the moment generating function of the net losses, since in theory the MGF gives the complete description of a random variable and show the applicability of the method at arriving to closed form solutions by comparing this result with expression of MGF available in the literature. Then we will proceed to obtain simpler expressions for the various moments of the net losses.

6.4.1 Moment generating function

Using the fact that the moment-generating functions (MGF) of the sum of two random variables is the product of the MGFs of the individual random variables, we propose the following: If we denote the MGF of the net discounted losses $K(t)$ as $M(s,t)$, then the MGF at a time $t+\Delta t$ can be expressed in terms of the MGF at time t as in Equation (6.29). This expression uses the fact that there can be two mutually exclusive and exhaustive sets of possibilities i.e. either there will or will not be a hazard occurrence in the interval Δt, following which in the instant $t+\Delta t$, the MGF will either be factored by the MGF of the discounted loss or otherwise stay the same. Therefore, the theorem of total probability can be used to arrive at the following expression. $M_{Z_i}(s,t)$ denotes the MGF of the discounted damage due to a single hazard occurrence can be obtained as:

$$M_{Z_i}(s,t) = \int_{-\infty}^{+\infty} e^{-sz} f_{Z_i}(z,t)dz \tag{6.28}$$

$$\begin{aligned} M(s,t+\Delta t) = M(s,t)P\left[N(t,t+\Delta t)=0\right] \\ + M(s,t)\cdot M_{Z_i}(s,t)P\left[N(t,t+\Delta t)=1\right] \end{aligned} \tag{6.29}$$

Using the definition of the NHPP as given in [94], we find that the corresponding probabilities of occurrence and non-occurrence of the hazard in a small interval Δt is given as $[\lambda(t)\Delta t + O(\Delta t)]$ and $[1 - \lambda(t)\Delta t + O(\Delta t)]$, respectively with $\lambda(t)$ being the NHPP rate function defined in Equation (2.28). It must be noted here that the condition of more than one event occurs in the interval $(t, t+\Delta t)$, since the corresponding probability $(O(\Delta t)$ will equate to zero under limiting conditions.

$$\lim_{\Delta t \to 0} M(s, t+\Delta t) = M(s,t)(1-\lambda(t)\Delta t+O(\Delta t))+M(s,t)\cdot M_{Z_i}(s,t)(\lambda(t)\Delta t+O(\Delta t)) \quad (6.30)$$

Simplifying and taking the limit over the time difference in Equation (6.30), the following is obtained.

$$\lim_{\Delta t \to 0} \frac{M(s, t+\Delta t) - M(s,t)}{\Delta t} = M(s,t)\lambda(t)\left[M_{Z_i}(s,t) - 1\right] \quad (6.31)$$

Giving us the following differential equation:

$$\frac{dM(s,t)}{dt} = M(s,t)\lambda(t)\left[M_{Z_i}(s,t) - 1\right] \quad (6.32)$$

with a boundary condition as $M(s,0) = 0$. Solving the differential equation along with the boundary condition, we get the following form:

$$ln(M(s,t)) = \int_0^t \lambda(t)\left[M_{Z_i}(s,t) - 1\right] dt \quad (6.33)$$

giving us the following expression which is identical to the expression obtained using the order statistics property for the NHPP arrival times and applying the permutation invariant theorem obtained in [62].

$$M(s,t) = exp\left[\int_0^t \lambda(t)\left[M_{Z_i}(s,t) - 1\right] dt\right] \quad (6.34)$$

However, using the Moment generating function for obtaining the moments is suitable only for simple functions like exponentially distributed damages. For more complicated damage distribution functions, the integrand in Equation (6.34) will become non-integrable, and a closed-form solution for the MGF cannot be obtained that can be suitably differentiated to

obtain the several moments. However, as mentioned, in theory, an MGF gives the complete description of a random variable.

6.4.2 Expected loss

Using a similar approach, the differential equations for the expected value of the present value of the net risk can be obtained. The expectation operator is denoted as $E[\cdot]$. Here, we use the fact that if there is a hazard occurrence in the interval Δt, the expected value of the discounted loss due to that event adds up to the expected value at time instant t.

$$E[K(t+\Delta t)] = E[K(t)](1-\lambda(t)\Delta t + O(\Delta t)) \\ + E[K(t)+Z(t)](\lambda(t)\Delta t + O(\Delta t)) \quad (6.35)$$

Similarly, taking the limit of $\Delta t \to 0$, and an initial condition that the expected damage at $t = 0$ is zero, the differential equation can be formed as follows. This result will also be utilized later for estimating the variance of the discounted losses.

$$\frac{dE[K(t)]}{dt} = \mu_Z(t)\lambda(t) \quad (6.36)$$

and the mean value of the damage cost can be calculated by solving the above differential equation:

$$E[K(t)] = \int_0^t \mu_Z(s)\lambda(s)ds \quad (6.37)$$

where, $\mu_Z(t) = E_Z[Z(t)]$ and can be given following Equation (2.36), and μ_X denoting the mean of $X_i's$ as:

$$\mu_Z(t) = E_Z[Z(t)] = E_X[(X\phi_1(t)+\phi_2(t))e^{-\rho t}] \quad (6.38)$$

$$= (\mu_X\phi_1(t)+\phi_2(t))e^{-\rho t} \quad (6.39)$$

Combining Equations (6.37) and (6.38), we get the following final expression for the ex-

pected losses:

$$E[K(t)] = \int_0^t (\mu_X \phi_1(s) + \phi_2(s)) e^{-\rho s} \lambda(s) ds \tag{6.40}$$

It may be noted that for a constant rate function, $\lambda(t) = \lambda_0$, zero discount rate and $\phi_1(t)$ and $\phi_2(t)$ equal to 1 and 0, respectively, in Equation (6.40), we will retrieve the solution for an HPP with IID damages following Wald's theorem [125].

If one is interested only in events that cross a given threshold or, in other words, in the thinned process, then the rate function $\lambda(t)$ and the moments of the damage costs $\mu'_{iZ}s$ should correspond to those of the thinned process in Equation (6.36).

6.4.3 Variance

We derive the variance of net discounted risk by first estimating the second moment of the net discounted losses as follows. It may be noted that there are no additional assumptions required for these derivations apart from the conditions required for defining the shock process to be an NHPP.

$$\begin{aligned} E[(K(t+\Delta t))^2] = E[(K(t))^2](1 - \lambda(t)\Delta t + O(\Delta t)) \\ + E[(K(t) + Z(t))^2](\lambda(t)\Delta t + O(\Delta t)) \end{aligned} \tag{6.41}$$

Simplifying and applying the limit $\Delta t \to 0$, we can obtain the following differential equation:

$$\frac{dE[(K(t))^2]}{dt} = 2E[K(t)]\lambda(t)\mu_Z + E[(Z(t))^2]\lambda(t) \tag{6.42}$$

Now from Equation (6.36) we can use the following result for the first term on the right of Equation (6.42).

$$\frac{d(E[K(t)]^2)}{dt} = 2E[K(t)]\lambda(t)\mu_Z \tag{6.43}$$

We can rewrite the expression in Equation (6.42), and arrive at the following condensed differential equation for the variance of the discounted losses where $Var[\cdot]$ is the variance operator.

$$\frac{d[E[(K(t))^2] - (E[K(t)])^2]}{dt} = \frac{d[Var(K(t)]}{dt} = E[(Z(t))^2]\lambda(t) \tag{6.44}$$

Therefore, by solving the above differential equation with the initial condition $Var[K(0)] = 0$, we can arrive at the following solution for the variance of the net losses.

$$Var[K(t)] = \int_0^t E[(Z(s))^2]\lambda(s)ds \tag{6.45}$$

Now, as per our definition of $Z(t)$ from Equation (2.36), we will have the following integrand for estimating the variance.

$$Var[K(t)] = \int_0^t (\mu_{2X}\phi_1^2(s) + 2\mu_X\phi_1(s)\phi_2(s) + \phi_2^2(s))e^{-2\rho s}\lambda(s)ds \tag{6.46}$$

where, μ_{2X} is the second moment of $X_i's$.

6.4.4 General n^{th} moment

Following the similar line of derivation as the mean and second moment and using the binomial theorem, the n^{th} ($\forall\ n \in \{1, 2, ...\infty\}$) moment of the discounted cumulative risk can be given as follows:

$$\frac{dE[(K(t))^n]}{dt} = \lambda(t)\sum_{i=1}^{n}\binom{n}{i}E[(K(t))^{n-i}]\mu_{iZ} \tag{6.47}$$

where, $\mu_{iZ} = E[(Z(t))^n]$, is the i^{th} moment of $Z(t)$ and $\binom{n}{i}$ is the binomial expression defined as:

$$\binom{n}{i} = \frac{n!}{i!(n-i)!} \tag{6.48}$$

Hence, raw moments of any order n for the discounted losses can be obtained recursively using the moments till order $(n-1)$ and using the initial condition $E[(K(0))^n] = 0\ \forall\ n$ as follows.

$$E[(K(t))^n] = \int_0^t \lambda(s)\sum_{i=1}^{n}\binom{n}{i}E[(K(s))^{n-i}]\mu_{iZ}ds \tag{6.49}$$

Using the raw moments, the central moments of the discounted net risk or losses can be calculated using the binomial theorem:

$$E[(K(t) - E[K(t)])^n] = \sum_{j=0}^{n} \binom{n}{j} (-1)^j E[(K(t))^{n-j}](E[K(t)])^j \tag{6.50}$$

Putting $n = 1$ in Equation (6.49) and $n = 2$ in Equation (6.50), the expressions for the mean and the variance obtained in Equations (6.37) and (6.45) can be retrieved, respectively. Although, the knowledge of all the raw and central moments can be assumed to completely represent a random variable, however, in the absence of analytical formulations to determine the exact distribution of the total discounted risk, one may select some standard positive valued distributions like Log-normal, Gamma or Weibull distribution, and depending on the number of parameters in standard distributions, these raw and central moments may be used to fit distributions using method of moments and compare them based on the closeness to the estimates of other moments. Although otherwise, the higher order moments are not the most useful for practical purposes but do provide some insights regarding the tail of a distribution [64].

6.5 Simulation based validation of analytical results

For the verification of the analytical results presented in Section 6.3, a Monte Carlo simulation (MCS) is conducted with 10^5 samples. A generalized form of rate function is chosen here that depicts a linear increase in mean rate with time and the seasonal fluctuations in several weather variables.

$$\lambda(t) = 10 + 0.01t + 2sin(6t) \quad (per\ yr) \tag{6.51}$$

The hazard magnitudes are assumed to be linearly scaled with time as $X(t) = X_0(1+0.01t)$ which represents the magnitude intensification of hazards with time, where X_0 is log-normally distributed with a mean of 10 units and coefficient of variation of 0.8 representing the base magnitude which may be obtained from historical data; similarly, the cost of damage when the hazards exceed the capacity is also assumed log-normal with a mean

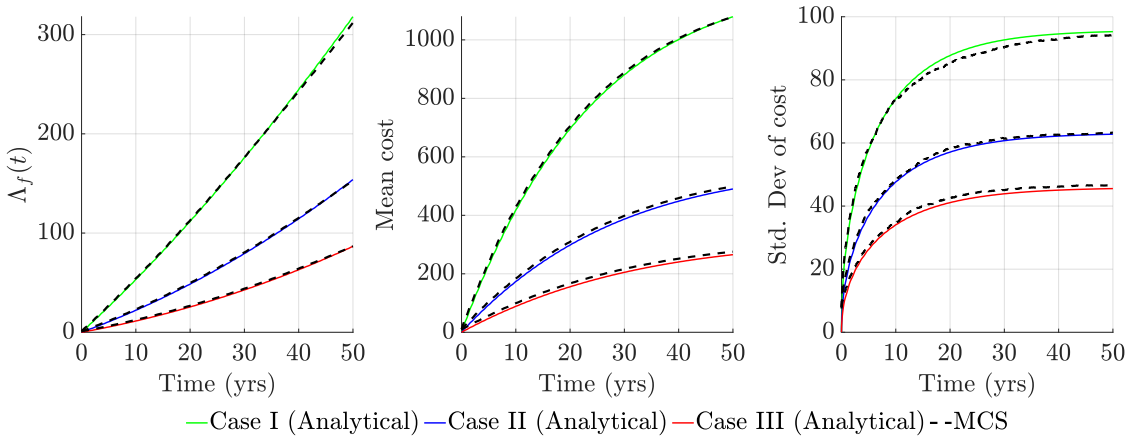


Figure 6.2: Verification using Monte Carlo simulation (MCS)

of 10 units (say $ Million) and CoV of 0.8, since the loads and costs usually have high variability. Three cases have been considered where the capacity is taken as the 50th, 80th and 90th percentile of the hazard distribution. The mean value function for the failure process $\Lambda_f(t)$, the expected discounted costs and its standard deviation over time are calculated for an annual discount rate of 5% analytically and through the simulation. The results for the three cases are plotted in Figure 6.2. The mean and standard deviation between the simulated and analytical results are compared, and it is found that based on Euclidean norms, their differences are less than 5% and 3%, respectively, which can be attributed to sampling errors in the MCS.

6.6 Examples

6.6.1 Example 1: Tornadoes in Ontario, Canada

Tornadoes in Canada cause large-scale loss of property and vegetation and incur high damage costs all around the year. The data provided by the Environment and Climate Change (ECCC), [101], based on the tornado events in 1980-2009, says that on a yearly basis, around 66.5 tornadoes incur a damage cost of around 18 Million dollars on average.

Table 6.1: Fujita scale classification

Fujita Scale	**Wind speed (m/s)**	**Expected Damage**	**Fraction of occurrences**
F0	17.8-32.6	Light	0.657
F1	32.7-50.3	Moderate	0.257
F2	50.4-70.3	Considerable	0.07
F3	70.4-91.9	Severe	0.013
F4	92.0-116.6	Devastating	0.003
F5	116.7-142.5	Incredible	0.001

Based on the studies [70], and governmental reports, [14], it can be said that there is an increasing trend in the frequency of tornado events in Canada over time as a result of global climate change. A brief trend analysis on tornado frequencies,[16] has shown using a Mann-Kendall test on the Auto-Regressive model (AR(1)) that, with 99% confidence there is an increasing trend of 1.6 tornadoes/decade in frequency. This translates to over 80% rise in mean tornado frequencies by the end of the twenty-first century in Ontario.

Based on the damage-causing capability of a tornado, they are classified into several classes based on their wind speed. One such classification scale is Fujita Scale [37] as reproduced in (Table 6.1). It may be noted here that although Canada started using the enhanced Fujita (EF) scale in 2013, but the data available for the mentioned time period has the classification based on the old Fujita (F) scale and hence the same is used in this example to maintain the coherency. From the report [101], the fraction of occurrences of different classes of tornadoes in the period is also mentioned in the same table for reference.

If mitigation strategies or adaptive measures are made in the design of engineering structures such as strengthening the connections between truss, wall, floor and sill plates [45], or enhancements in the Building code requirements by increasing the design wind speed and including provisions for power and communication failures [102], so that the buildings can sustain the tornadoes of lower intensity without much damage, it is important to evaluate the reduction in economic losses due to the investments made in these measures. Depending on the level of adaptive measures and enhancements, the rate of occurrence of tornadoes exceeding the threshold capacity level can be computed using the thinning property. The adaptation measures depend on the intensity of tornadoes we want our

infrastructure to resist. For example, to mitigate lower intensity tornadoes, like F0 and F1 tornadoes, for which the damages are minimal to moderate and characterized as minor damages to chimneys, uprooting of trees, and overturning of automobiles, investments need to be made for proper prediction and warning systems. However, for higher intensity tornadoes like F4 or F5, additional structural strengthening measures are recommended that make them resistant to high wind speeds, for example, using J-bolts or dowels to strengthen the anchorage between the sill plate and foundation wall and strengthening connections between the roof and wall [45]. Another cost-benefit analysis based on a case study on the Oklahoma City tornado suggested that a 30% reduction in a home's insured losses can be ensured with a strengthened construction at an investment of less than $500 [111].

Therefore, this economic analysis bears critical importance in planning investments in risk-mitigation strategies by concerned authorities. Damage cost data were obtained from the Canadian Governmental database [4]. For the purpose of analysis, we consider the region of Ontario, since it is one of the provinces that see very high frequencies of tornadoes in Canada.

NHPP rate model The tornado database provides information regarding the tornadoes that occurred in Ontario and based on the data, here the rate of tornado events is taken as 14.18/year as the average yearly number of tornadoes for the last decade. The tornado frequency in Ontario increased by 1.6 tornadoes/decade with 99% confidence as analyzed by [16] over the period 1950-2007. In the absence of any other data or projections, it has been assumed that the increase in tornado frequency in Ontario will follow a similar trend in the remaining duration of the current century. Therefore, the linear rate function is taken as Equation (6.52) and the corresponding mean value function is given as Equation (6.53).

$$\lambda(t) = 14.18 + 0.16t, (per\ year) \tag{6.52}$$

$$\Lambda(t) = 14.18t + 0.08t^2 \tag{6.53}$$

where t is in years and $t = 0$ in 2020. The linear rate function here is justified for a number of reasons, the linear regression performed by [16] has detected the increas-

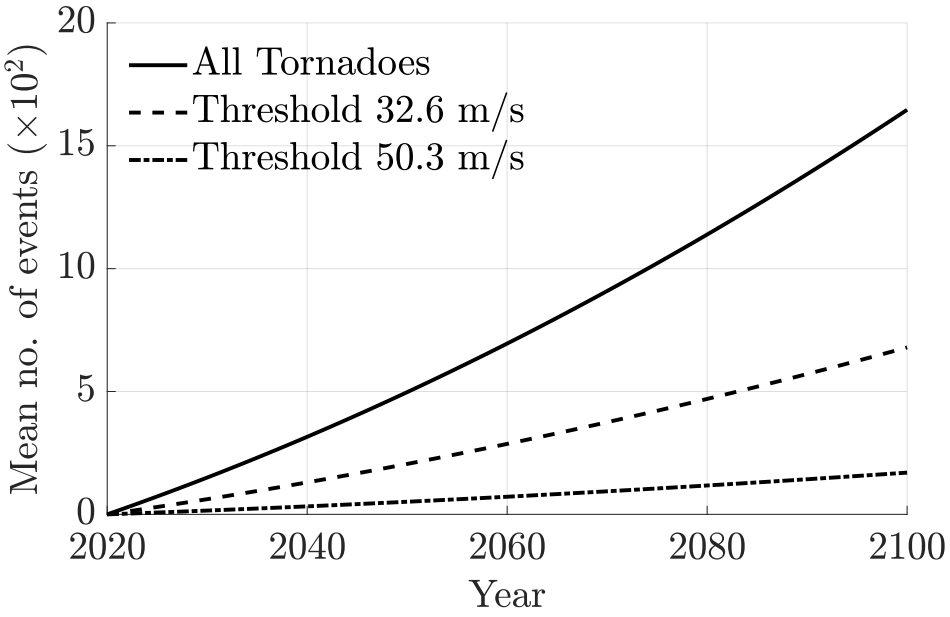


Figure 6.3: Expected number of tornadoes (Mean value function) until a given year exceeding different threshold wind speeds

ing trend at a confidence level of 95%, second, the change in the rate is slow i.e 0.16 tornadoes/year, implying that fitting higher order functions may lead to over-fitting and give drastically inaccurate results. For more accurate projections one may use dynamic Bayesian frameworks by mapping tornadoes with other weather variables like temperature and precipitation, however, that is beyond the scope of this study. For different adaptation measures in the design of infrastructure systems, the number of tornadoes that can cause significant damage will be ones that exceed the design wind speeds. The mean number of tornadoes exceeding the design threshold is calculated using the thinning of the base rate given in Equation (6.52) and integrating until the given time as shown in Figure 6.3.

Wind speed distribution Based on Table 6.1 and the tornado wind speed data, a three-parameter Weibull distribution with location, scale and shape as 17.22 m/s, 16.98

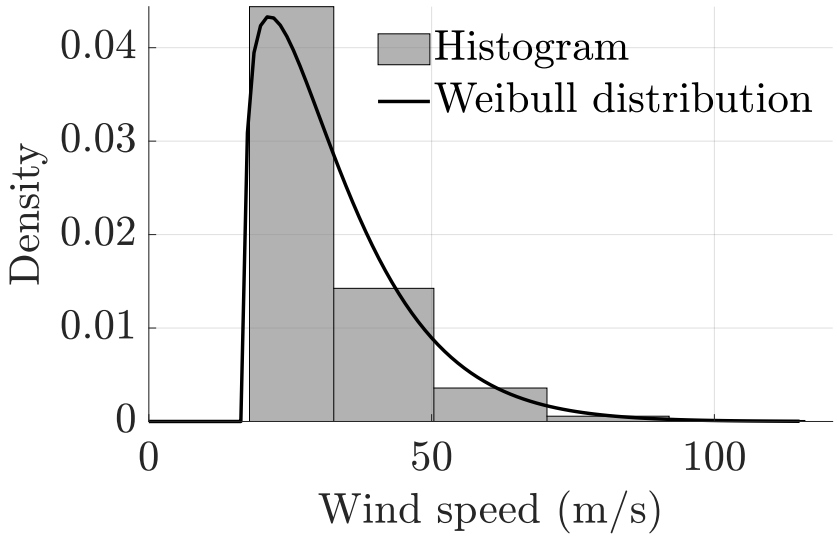
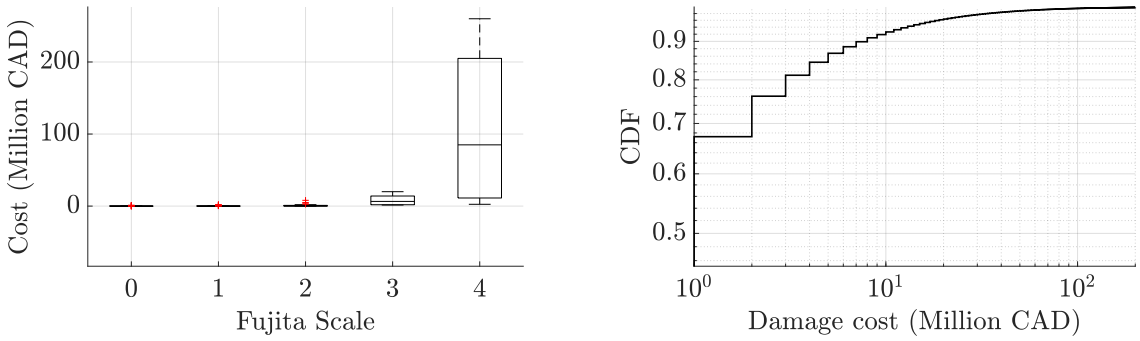


Figure 6.4: Tornado wind speed distribution

m/s and 1.23 respectively was seen to be a good fit for the samples as shown in Figure 6.4.

Damage cost From the Canadian National Tornado Database (CNTD), the damage costs for the individual tornado events of Ontario in the duration 1980-2009 are obtained. It can be found in Figure 6.5a, that for lower intensity tornadoes (Fujita scale 0 and 1) the economic losses are negligible as compared to that of Fujita scale 2,3 and 4, therefore we consider two threshold wind speeds 32.6 and 50.3 m/s, the corresponding upper bounds of F0 and F1 Fujita scale respectively for our analysis. The mean and second moments of the damage costs are 6.14 Million CAD with COV of 5.33 (for 32.6 m/s threshold), and 13.55 Million CAD with COV of 3.57 (for 50.3m/s threshold). For the discounted analysis, a discount rate of five per cent is used.

Results The plots in Figure 6.6 display the discounted and undiscounted LCCs over a century showing the mean values and range of values within one standard deviation. The results indicate that taking adaptation measures to prevent damages from F0 and F1



(a) Damage cost with Fujita scales

(b) CDF of damage cost for a single tornado

Figure 6.5: Tornado damage costs

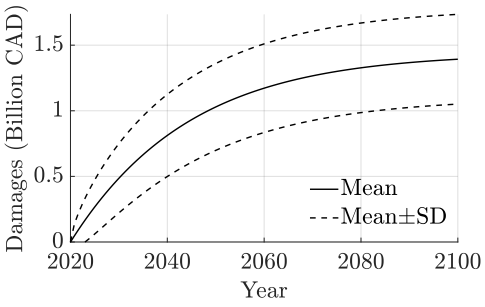
tornadoes can reduce the mean losses by 38.8% and 66.2% respectively, which means that until 2100 the discounted losses go down by about 0.53 and 0.92 Billion CAD while the undiscounted losses go down by 2.64 and 4.51 Billion CAD.

The distribution of the undiscounted damage cost to be incurred by all the tornadoes if no adaptive measures are taken by the end of 2040, 2070 and 2100 is calculated using Panjer's recursion technique and plotted in Figure 6.7. Figure 6.8 shows the coefficient of variation (COV) of the discounted and undiscounted LCC for both threshold values. The COV reduces over time for all the cases, with the COV of the undiscounted LCC of 50.3 m/s being the lowest.

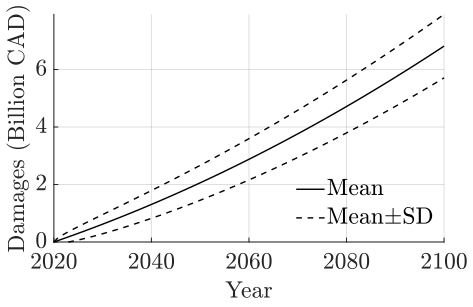
6.6.2 Example 2: Heat wave (HW) in US cities

From a study [43], based on data from 50 US cities over the duration 1960-2000, it has been found that due to climate change, the number of HWs per year has increased at a rate of 0.6 ± 0.14 per decade.

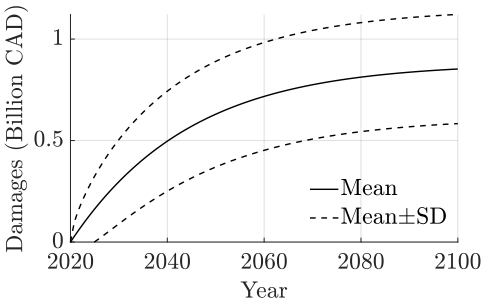
To demonstrate the method in this study, let us construct the NHPP model with the rate as the rate of occurrence of the HWs and the load using the time-dependent intensities. The data for the decade 2000s can be taken as the base model and assuming that the same trend follows for the rest of the century the model can be prepared as follows:



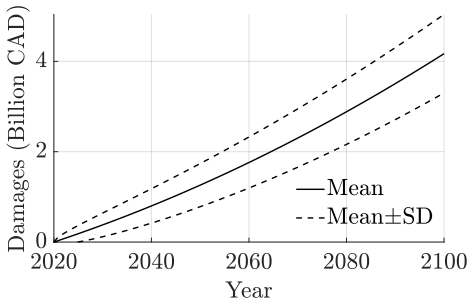
(a) All tornadoes (discounted)



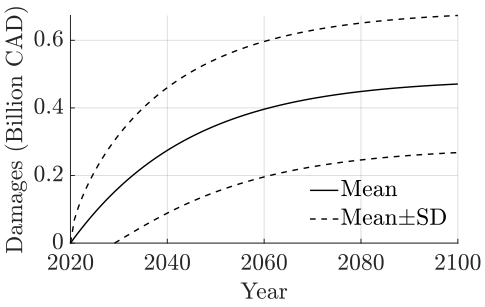
(b) All tornadoes (undiscounted)



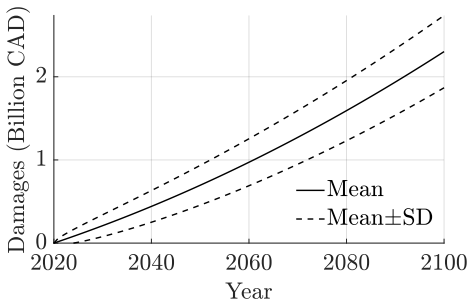
(c) Threshold 32.6 m/s (discounted)



(d) Threshold 32.6 m/s (undiscounted)



(e) Threshold 50.3 m/s (discounted)



(f) Threshold 50.3 m/s (undiscounted)

Figure 6.6: Discounted and undiscounted damage costs for the Tornadoes with a threshold of 32.6 m/s (i.e. above F0) and 50.3 m/s (i.e. above F1)

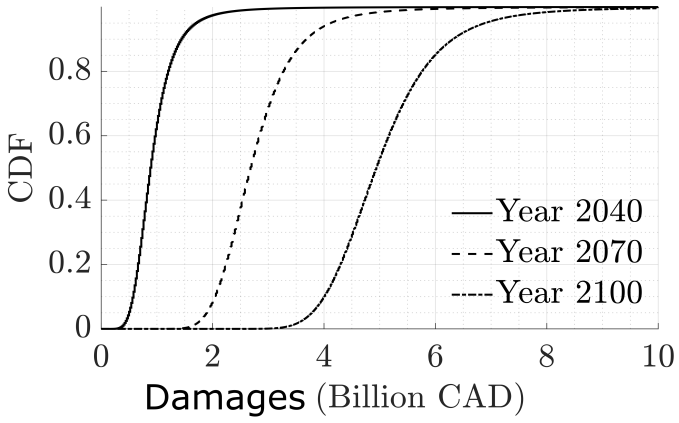


Figure 6.7: Cumulative distribution of damages

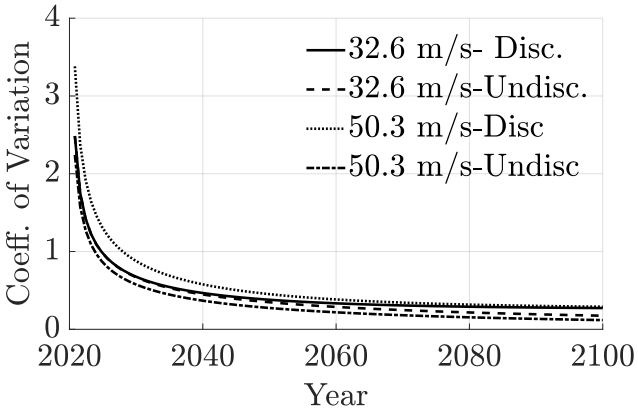


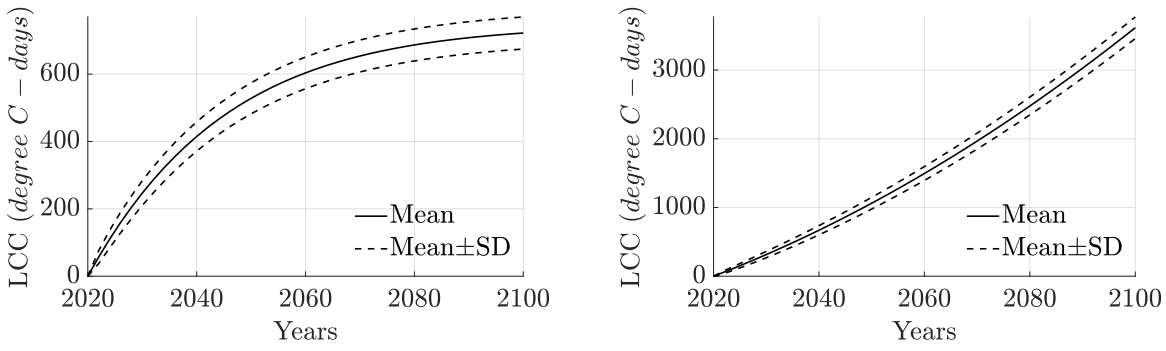
Figure 6.8: Coefficient of Variation of the damages

$$\lambda = 4.47 + \frac{0.6}{10}t, \ (per\ year) \tag{6.54}$$

where, t represents the time from 2000, e.g., t for the year 2025 is 25. The equivalent cost per HW can be considered as the product of the average duration of the heat waves and the average temperature above the threshold with a mean $\mu_C = 6.5246°C\ days/HW$ and COV 0.2 or $\mu_{2C} = 44.21(°C\ days)^2/HW$. For a discount rate of 5%, the mean and standard deviation of discounted and undiscounted LCC can be calculated for the remaining century as shown in Figure 6.9.

6.7 Conclusions

In conclusion, this chapter presents a novel method for estimating economic losses due to hazards whose frequency and intensity are driven by climate change. The arrival times and magnitudes of the loads are modeled as a marked non-homogeneous Poisson process (NHPP) to capture the nonstationarity in the process. The analytical formulations for computing the mean, variance, and distribution of losses that haven't been discounted, as well as the mean and variance of losses that have been discounted, within a given time



(a) Discounted

(b) Undiscounted

Figure 6.9: Cost in equivalent $°C - days$

period are presented. The results are applied to estimate the losses due to tornadoes in Ontario, Canada, until 2100. This study also emphasizes that if adaptive measures are taken to strengthen infrastructure systems against climate-driven hazards such that the losses due to events under a given threshold magnitude are negligible, then by using the thinning property of the NHPP, the reduced losses can also be calculated which will further facilitate a cost-benefit analysis for the adaptive measure. The formulation was also used to estimate the expected degree days due to heat wave events in US cities until the end of the current century.

References

[1] Average Annual Humidity at Canadian Cities, howpublished = https://www.currentresults.com/weather/canada/cities/humidity-annual-average.php, note = Accessed: 2023-11-07.

[2] CMIP5 Multi-model Ensembles of Temperature projections , howpublished = https://open.canada.ca/data/en/dataset/ce5b431c-9ea3-43d2-be84-5ab89d52c878, note = Accessed: 2023-11-07.

[3] Coupled Model Intercomparison Project Phase 6 climate scenarios, howpublished = https://climate-scenarios.canada.ca/?page=cmip6-scenarios, note = Accessed: 2023-11-07.

[4] Canadian National Tornado Database, 2015. Accessed: 2021-08-23.

[5] Criteria for public weather alerts, 2024.

[6] Dmitri V Alexandrov, Irina A Bashkirtseva, Michel Crucifix, and Lev B Ryashko. Nonlinear climate dynamics: From deterministic behaviour to stochastic excitability and chaos. *Physics Reports*, 902:1–60, 2021.

[7] Moises Angeles-Malaspina, Jorge E González-Cruz, and Nazario Ramírez-Beltran. Projections of heat waves events in the intra-americas region using multimodel ensemble. *Advances in Meteorology*, 2018(1):7827984, 2018.

[8] KY Ann, S-W Pack, J-P Hwang, H-W Song, and S-H Kim. Service life prediction of a concrete bridge structure subjected to carbonation. *Construction and Building Materials*, 24(8):1494–1501, 2010.

[9] Emilio Bastidas-Arteaga, Alaa Chateauneuf, Mauricio Sánchez-Silva, Ph Bressolette, and Franck Schoefs. Influence of weather and global warming in chloride ingress into concrete: A stochastic approach. *Structural Safety*, 32(4):238–249, 2010.

[10] Fabio Biondini and Dan M Frangopol. Life-cycle performance of civil structure and infrastructure systems: Survey. *Journal of Structural Engineering*, 144(1):06017008, 2018.

[11] Harold E Brooks. Severe thunderstorms and climate change. *Atmospheric research*, 123:129–138, 2013.

[12] E Bush and D.S Lemmen. *Canada's Changing Climate*. Government of Canada, Ottawa, Ontario, 2019.

[13] Ray Bustinza, Germain Lebel, Pierre Gosselin, Diane Bélanger, and Fateh Chebana. Health impacts of the july 2010 heat wave in québec, canada. *BMC public health*, 13:1–7, 2013.

[14] AJ Cannon, DI Jeong, X Zhang, and FW Zwiers. Resilient buildings and core public infrastructure: An assessment of the impact of climate change on climatic design data in Canada. *Environment and Climate Change Canada: Gatineau, QC, Canada*, 2020.

[15] Alex J. Cannon, Dae Il Jeong, Xuebin Zhang, and Francis W. Zwiers. Resilient Buildings and Core Public Infrastructure: An Assessment of the Impact of Climate Change on Climatic Design Data in Canada. Technical report, 2020.

[16] Zuohao Cao and Huaqing Cai. Detection of tornado frequency trend over ontario, canada. *The Open Atmospheric Science Journal*, 5(1), 2011.

[17] Mark A. Cesare, Carlos Santamarina, Carl Turkstra, and Erik H. Vanmarcke. Modeling Bridge Deterioration with Markov Chains. *Journal of Transportation Engineering*, 118(6):820–833, 11 1992.

[18] Alaa Chateauneuf, Ali Messabhia, Ayman Ababneh, et al. Reliability analysis of corrosion initiation in reinforced concrete structures subjected to chlorides in presence of epistemic uncertainties. *Structural Safety*, 86:101976, 2020.

[19] Dong Chen and Sankaran Mahadevan. Chloride-induced reinforcement corrosion and concrete cracking simulation. *Cement and Concrete Composites*, 30(3):227–238, 2008.

[20] Hua-Peng Chen and Mehrdad Bahari Mehrabani. Reliability analysis and optimum maintenance of coastal flood defences using probabilistic deterioration modelling. *Reliability Engineering & System Safety*, 185:163–174, 2019.

[21] Linyin Cheng and Amir AghaKouchak. Nonstationary precipitation intensity-duration-frequency curves for infrastructure design in a changing climate. *Scientific reports*, 4(1):7093, 2014.

[22] Stuart Coles, Joanna Bawa, Lesley Trenner, and Pat Dorazio. *An introduction to statistical modeling of extreme values*, volume 208. Springer, 2001.

[23] Gustavo Souza Correia, Leandro Farina, Claudia Klose Parise, Gabriel Bonow Münchow, and M Alves Rita de Cássia. Ensemble hindcasting of winds and waves for the coastal and oceanic region of southern brazil. *Computers & Geosciences*, 191:105658, 2024.

[24] Daryl J Daley, David Vere-Jones, et al. *An introduction to the theory of point processes: volume I: elementary theory and methods*. Springer, 2003.

[25] Warren Dent and Richard Ballintine. A REVIEW OF THE ESTIMATION OF TRANSITION PROBABILITIES IN MARKOV CHAINS. *Australian Journal of Agricultural Economics*, 15(2):69–81, 8 1971.

[26] Ebrahim Afsar Dizaj, Jamie E Padgett, and Mohammad M Kashani. A markov chain-based model for structural vulnerability assessmentof corrosion-damaged reinforced concrete bridges. *Philosophical Transactions of the Royal Society A*, 379(2203):20200290, 2021.

[27] Scott R Eliason. *Maximum likelihood estimation: Logic and practice*, volume 96. Sage, 1993.

[28] Svend Engelund and John D Sørensen. A probabilistic model for chloride-ingress and initiation of corrosion in reinforced concrete structures. *Structural safety*, 20(1):69–89, 1998.

[29] Environment and Climate Change Canada. Understanding shared socio-economic pathways (ssps). https://climatedata.ca/resource/understanding-shared-socio-economic-pathways-ssps/. Accessed: 04-18-2024.

[30] Veronika Eyring, Sandrine Bony, Gerald A Meehl, Catherine A Senior, Bjorn Stevens, Ronald J Stouffer, and Karl E Taylor. Overview of the coupled model intercomparison project phase 6 (cmip6) experimental design and organization. *Geoscientific Model Development*, 9(5):1937–1958, 2016.

[31] Amanda W Fadel, Guilherme F Marques, Joel A Goldenfum, Josué Medellín-Azuara, and Amaury Tilmant. Full flood cost: insights from a risk analysis perspective. *Journal of Environmental Engineering*, 144(9):04018071, 2018.

[32] Francisco J Fernández, Felipe Vásquez-Lavín, Roberto D Ponce, René Garreaud, Francisco Hernández, Oscar Link, Francisco Zambrano, and Michael Hanemann. The economics impacts of long-run droughts: Challenges, gaps, and way forward. *Journal of Environmental Management*, 344:118726, 2023.

[33] Dan M Frangopol and Jung S Kong. Expected maintenance cost of deteriorating civil infrastructures. In *Life-cycle cost analysis and design of civil infrastructure systems*, pages 22–47. American Society of Civil Engineers, 2001.

[34] Christopher M Free, Sean C Anderson, Elizabeth A Hellmers, Barbara A Muhling, Michael O Navarro, Kate Richerson, Lauren A Rogers, William H Satterthwaite, Andrew R Thompson, Jenn M Burt, et al. Impact of the 2014–2016 marine heatwave on us and canada west coast fisheries: Surprises and lessons from key case studies. *Fish and Fisheries*, 24(4):652–674, 2023.

[35] David Freedman. *Markov chains*. Springer Science & Business Media, 2012.

[36] Gongkang Fu, Dinesh Devaraj, et al. Methodology of homogeneous and non-homogeneous Markov Chains for modeling bridge element deterioration. 2008.

[37] Tetsuya Theodore Fujita. Proposed characterization of tornadoes and hurricanes by area and intensity, 1971.

[38] Paolo Gardoni, Colleen Murphy, and Arden Rowell. *Risk analysis of natural hazards: Interdisciplinary challenges and integrated solutions*. Springer, 2016.

[39] Roger G Ghanem and Pol D Spanos. *Stochastic finite elements: a spectral approach*. Courier Corporation, 2003.

[40] Kamal Golabi and Richard Shepard. Pontis: A system for maintenance optimization and improvement of us bridge networks. *Interfaces*, 27(1):71–88, 1997.

[41] Geoffrey Guest, Jieying Zhang, Rebecca Atadero, and Hamidreza Shirkhani. Incorporating the effects of climate change into bridge deterioration modeling: the case of slab-on-girder highway bridge deck designs across canada. *Journal of Materials in Civil Engineering*, 32(7):04020175, 2020.

[42] Geoffrey Guest, Jieying Zhang, Omran Maadani, and Hamidreza Shirkhani. Incorporating the impacts of climate change into infrastructure life cycle assessments: A case study of pavement service life performance. *Journal of Industrial Ecology*, 24(2):356–368, 2020.

[43] Dana Habeeb, Jason Vargo, and Brian Stone. Rising heat wave trends in large US cities. *Natural Hazards*, 76:1651–1665, 2015.

[44] J Hansen, Mki Sato, R Ruedy, A Lacis, K Asamoah, K Beckford, S Borenstein, E Brown, B Cairns, B Carlson, et al. Forcings and chaos in interannual to decadal climate change. *Journal of Geophysical Research: Atmospheres*, 102(D22):25679–25720, 1997.

[45] Craig Henderson, Tim Huff, and Gary Bouton. Structural observations and tornado damage mitigation concepts: March 2020 tennessee tornadoes. *Practice Periodical on Structural Design and Construction*, 26(2):05021001, 2021.

[46] Renata Schneiderova Heralova. Life cycle cost optimization within decision making on alternative designs of public buildings. *Procedia engineering*, 85:454–463, 2014.

[47] Julio E Herrera-Estrada and Justin Sheffield. Uncertainties in future projections of summer droughts and heat waves over the contiguous united states. *Journal of Climate*, 30(16):6225–6246, 2017.

[48] Annette L Hirsch, Nina N Ridder, Sarah E Perkins-Kirkpatrick, and Anna Ukkola. Cmip6 multimodel evaluation of present-day heatwave attributes. *Geophysical Research Letters*, 48(22):e2021GL095161, 2021.

[49] Danny Hopkin, Ian Fu, and Ruben Van Coile. Adequate fire safety for structural steel elements based upon life-time cost optimization. *Fire Safety Journal*, 120:103095, 2021.

[50] Danny Hopkin, Michael Spearpoint, Matthew Arnott, and Ruben Van Coile. Cost-benefit analysis of residential sprinklers–application of a judgement value method. *Fire safety journal*, 106:61–71, 2019.

[51] Y Hundecha, A St-Hilaire, TBMJ Ouarda, S El Adlouni, and Philippe Gachon. A nonstationary extreme value analysis for the assessment of changes in extreme annual wind speed over the gulf of st. lawrence, canada. *Journal of applied meteorology and climatology*, 47(11):2745–2759, 2008.

[52] Arne Instanes. Impacts of a changing climate on infrastructure: buildings, support systems, and industrial facilities. In *2006 IEEE EIC Climate Change Conference*, pages 1–4. IEEE, 2006.

[53] Amin Jamali, Ueli Angst, Bryan Adey, and Bernhard Elsener. Modeling of corrosion-induced concrete cover cracking: A critical analysis. *Construction and Building Materials*, 42:225–237, 2013.

[54] Dae II Jeong, Alex J Cannon, and Bin Yu. Influences of atmospheric blocking on north american summer heatwaves in a changing climate: a comparison of two canadian earth system model large ensembles. *Climatic Change*, 172(1):5, 2022.

[55] Gaofeng Jia and Paolo Gardoni. Stochastic life-cycle analysis: Renewal-theory life-cycle analysis with state-dependent deterioration stochastic models. *Structure and Infrastructure Engineering*, 15(8):1001–1014, 2019.

[56] M. J. Kallen. *Markov processes for maintenance optimization ofcivil infrastructure in the Netherlands*. PhD thesis, Delft University of Technology, Delft, Netherlands, 2007.

[57] Yong-Joong Kang. *Minimum life-cycle cost structural design against natural hazards*. University of Illinois at Urbana-Champaign, 2000.

[58] Xiaoxia Lai, Jiahong Wen, Xinmeng Shan, Liucheng Shen, Chengcheng Wan, Lin Shao, Yanjuan Wu, Bo Chen, and Weijiang Li. Cost-benefit analysis of local knowledge-based flood adaptation measures: A case study of Datian community in Zhejiang Province, China. *International Journal of Disaster Risk Reduction*, 87:103573, 2023.

[59] Douglas LeComte. Global weather highlights 2010: Flooding, heatwaves, and fires. *weatherwise: THE POWER, THE BEAUTY, THE EXCITEMENT*, 64(3):21–28, 2011.

[60] Sanghoon Lee, James R Wilson, and Melba M Crawford. Modeling and simulation of a nonhomogeneous poisson process having cyclic behavior. *Communications in Statistics-Simulation and Computation*, 20(2-3):777–809, 1991.

[61] Nam Lethanh, Jürgen Hackl, and Bryan T Adey. Determination of Markov transition probabilities to be used in bridge management from mechanistic-empirical models. *Journal of bridge engineering*, 22(10):04017063, 2017.

[62] Ghislain Léveillé and Emmanuel Hamel. Conditional, non-homogeneous and doubly stochastic compound poisson processes with stochastic discounted claims. *Methodology and Computing in Applied Probability*, 20:353–368, 2018.

[63] Chao Li, Francis Zwiers, Xuebin Zhang, Guilong Li, Ying Sun, and Michael Wehner. Changes in annual extremes of daily temperature and precipitation in cmip6 models. *Journal of Climate*, 34(9):3441–3460, 2021.

[64] Bruce G Lindsay and Prasanta Basak. Moments determine the tail of a distribution (but not much else). *The American Statistician*, 54(4):248–251, 2000.

[65] Peng Liu, Zhiwu Yu, and Ying Chen. Carbonation depth model and carbonated acceleration rate of concrete under different environment. *Cement and Concrete Composites*, 114:103736, 2020.

[66] Yajun Liu and Xianming Shi. Stochastic modeling of service life of concrete structures in chloride-laden environments. *Journal of materials in civil engineering*, 24(4):381–390, 2012.

[67] Pei-Yuan Lun, Zhao-Hui Lu, Xiao-gang Zhang, Qiang Zhang, and Ran Zhao. Experimental study and suggested mathematical model for chloride-induced reinforcement corrosion rate. In *Structures*, volume 34, pages 2014–2029. Elsevier, 2021.

[68] Elizaveta Malinina and Nathan P Gillett. The 2021 heatwave was less rare in western canada than previously thought. *Weather and Climate Extremes*, 43:100642, 2024.

[69] Elia Mario, Lafortezza Raffaele, Cappelluti Onofrio, Costa-Saura Josè Maria, Bacciu Valentina, Giannico Vincenzo, Changliang Shao, and Sanesi Giovanni. Coupling heat wave and wildfire occurrence across multiple ecoregions within a Eurasia longitudinal gradient. *Science of the total environment*, 912:169269, 2024.

[70] GA McBean. Risk mitigation strategies for tornadoes in the context of climate change and development. In *Mitigation of natural hazards and disasters: International perspectives*, pages 25–34. Springer, 2005.

[71] Seung-Ki Min, Xuebin Zhang, Francis W Zwiers, Petra Friederichs, and Andreas Hense. Signal detectability in extreme precipitation changes assessed from twentieth century climate simulations. *Climate Dynamics*, 32:95–111, 2009.

[72] TU Mohammed and H Hamada. Relationship between free chloride and total chloride contents in concrete. *Cement and concrete research*, 33(9):1487–1490, 2003.

[73] Max A Moritz, Marc-André Parisien, Enric Batllori, Meg A Krawchuk, Jeff Van Dorn, David J Ganz, and Katharine Hayhoe. Climate change and disruptions to global fire activity. *Ecosphere*, 3(6):1–22, 2012.

[74] John A Mullard and Mark G Stewart. Corrosion-Induced Cover Cracking: New Test Data and Predictive Models. *ACI Structural Journal*, 108(1), 2011.

[75] Luís C Neves and Dan M Frangopol. Condition, safety and cost profiles for deteriorating structures with emphasis on bridges. *Reliability engineering & system safety*, 89(2):185–198, 2005.

[76] Marc Norgate, PR Tiwari, Sushant Das, and Dhirendra Kumar. On the heat waves over india and their future projections under different ssp scenarios from cmip6 models: Climate change, heat wave, health. *International Journal of Climatology*, 2024.

[77] National Oceanic and Atmospheric Administration. Climate models. https://www.climate.gov/maps-data/climate-data-primer/predicting-climate/climate-models. Accessed: 04-22-2024.

[78] Government of Canada. Cmip6 and shared socio-economic pathways overview. https://climate-scenarios.canada.ca/?page=cmip6-overview-notes. Accessed: 04-18-2024.

[79] Government of Canada. Representative concentration pathways. https://climate-scenarios.canada.ca/?page=scen-rcp. Accessed: 04-18-2024.

[80] Ontario. Transportation Engineering Branch. Bridge Office. *Ontario Structure Inspection Manual: OSIM*. Ontario Ministry of Transportation, Bridge Office.

[81] D Panagoulia, P Economou, and C Caroni. Stationary and nonstationary generalized extreme value modelling of extreme precipitation over a mountainous area under climate change. *Environmetrics*, 25(1):29–43, 2014.

[82] Mahesh D Pandey and Z Lounis. Stochastic modelling of non-stationary environmental loads for reliability analysis under the changing climate. *Structural Safety*, 103:102348, 2023.

[83] Mahesh D Pandey and N Manzana. An investigation of non-stationary nature of ice accretion data. In *Proceedings - Int. Workshop on Atmospheric Icing of Structures*, pages 1–6, 2019.

[84] Mahesh D. Pandey and J. A.M. van der Weide. Probability distribution of the seismic damage cost over the life cycle of structures. *Structural Safety*, 72:74–83, 2018.

[85] Mahesh D Pandey and JAM Van Der Weide. Stochastic renewal process models for estimation of damage cost over the life-cycle of a structure. *Structural Safety*, 67:27–38, 2017.

[86] MD Pandey and JM Van Noortwijk. Gamma process model for time-dependent structural reliability analysis. In *Bridge Maintenance, Safety, Management and Cost, Proceedings of the Second International Conference on Bridge Maintenance, Safety and Management (IABMAS), Kyoto, Japan*, pages 18–22, 2004.

[87] Angela Peck, Predrag Prodanovic, and Slobodan PP Simonovic. Rainfall intensity duration frequency curves under climate change: City of london, ontario, canada. *Canadian Water Resources Journal/Revue canadienne des ressources hydriques*, 37(3):177–189, 2012.

[88] Humberto Pereira, Ana Picado, Magda C Sousa, Ines Alvarez, and João M Dias. Assessing cmip6 models in simulating meteo-oceanographic variability on spanish continental coasts. *Ocean Modelling*, page 102395, 2024.

[89] SE Perkins-Kirkpatrick and SC Lewis. Increasing trends in regional heatwaves. *Nature communications*, 11(1):3357, 2020.

[90] Sjoukje Y Philip, Sarah F Kew, Geert Jan Van Oldenborgh, Faron S Anslow, Sonia I Seneviratne, Robert Vautard, Dim Coumou, Kristie L Ebi, Julie Arrighi, Roop Singh, et al. Rapid attribution analysis of the extraordinary heat wave on the pacific coast of the us and canada in june 2021. *Earth System Dynamics*, 13(4):1689–1713, 2022.

[91] Rüdiger Rackwitz. Optimization—the basis of code-making and reliability verification. *Structural safety*, 22(1):27–60, 2000.

[92] Steven E "Rigdon and Asit P" Basu. *"Statistical methods for the reliability of repairable systems"*. Wiley, 2000.

[93] Guido Roelfstra, Rade Hajdin, Bryan Adey, and Eugen Brühwiler. Condition evolution in bridge management systems and corrosion-induced deterioration. *Journal of Bridge Engineering*, 9(3):268–277, 2004.

[94] Sheldon M Ross. *Introduction to probability models*. Academic press, 2014.

[95] Simone Russo, Alessandro Dosio, Rune G Graversen, Jana Sillmann, Hugo Carrao, Martha B Dunbar, Andrew Singleton, Paolo Montagna, Paulo Barbola, and Jürgen V Vogt. Magnitude of extreme heat waves in present climate and their projection in a warming world. *Journal of Geophysical Research: Atmospheres*, 119(22):12–500, 2014.

[96] Ajay Saini and Iris Tien. Impacts of climate change on the assessment of long-term structural reliability. *ASCE-ASME Journal of Risk and Uncertainty in Engineering Systems, Part A: Civil Engineering*, 3(3):04017003, 2017.

[97] Jose D Salas and Jayantha Obeysekera. Revisiting the concepts of return period and risk for nonstationary hydrologic extreme events. *Journal of hydrologic engineering*, 19(3):554–568, 2014.

[98] Kamal C Sarma and Hojjat Adeli. Life-cycle cost optimization of steel structures. *International Journal for Numerical Methods in Engineering*, 55(12):1451–1462, 2002.

[99] Richard Serfozo. *Basics of applied stochastic processes*. Springer Science & Business Media, 2009.

[100] Hamidreza Shirkhani, Jieying Zhang, and Zoubir Lounis. Ensemble analysis of climate-change impacts on design-service life of reinforced concrete bridge decks across Canada. *Natural Hazards Review*, 21(3):04020030, 2020.

[101] David Sills. Canadian Tornado Fact Sheet, 2015. Accessed: 2021-08-23.

[102] Thomas L Smith, Manuel Perotin, and Erin Walsh. Enhancing tornado performance of critical facilities: findings and recommendations of fema's mitigation assessment team. In *Structures Congress 2012*, pages 977–988, 2012.

[103] Mark G Stewart. Climate adaptation engineering: An optimist's view. *ASCE-ASME Journal of Risk and Uncertainty in Engineering Systems, Part A: Civil Engineering*, 9(1):02522002, 2023.

[104] Mark G Stewart and Xiaoli Deng. Climate impact risks and climate adaptation engineering for built infrastructure. *ASCE-ASME Journal of Risk and Uncertainty in Engineering Systems, Part A: Civil Engineering*, 1(1):04014001, 2015.

[105] Mark G Stewart and David V Rosowsky. Structural safety and serviceability of concrete bridges subject to corrosion. *Journal of Infrastructure systems*, 4(4):146–155, 1998.

[106] Mark G Stewart and David V Rosowsky. Extreme events for infrastructure: Uncertainty and risk. *Engineering for Extremes: Decision-Making in an Uncertain World*, pages 3–27, 2021.

[107] Mark G Stewart and David V Rosowsky. Engineering for extremes. *Springer International Publishing*, 2022.

[108] Mark G Stewart and Dimitri V Val. Multiple limit states and expected failure costs for deteriorating reinforced concrete bridges. *Journal of Bridge Engineering*, 8(6):405–415, 2003.

[109] Bruno Sudret. Probabilistic models for the extent of damage in degrading reinforced concrete structures. *Reliability Engineering & System Safety*, 93(3):410–422, 2008.

[110] Qiaohong Sun, Chiyuan Miao, Martin Hanel, Alistair GL Borthwick, Qingyun Duan, Duoying Ji, and Hu Li. Global heat stress on health, wildfires, and agricultural crops under different levels of climate warming. *Environment international*, 128:125–136, 2019.

[111] Daniel Sutter, Dakshina DeSilva, and Jamie Kruse. An economic analysis of wind resistant construction. *Journal of Wind Engineering and Industrial Aerodynamics*, 97(3-4):113–119, 2009.

[112] Maedeh Taghaddos and Yasser Mohamed. Predicting bridge conditions in ontario: A case study. In *ISARC. Proceedings of the International Symposium on Automation and Robotics in Construction*, volume 36, pages 166–171. IAARC Publications, 2019.

[113] Karl E Taylor, Ronald J Stouffer, and Gerald A Meehl. An overview of cmip5 and the experiment design. *Bulletin of the American meteorological Society*, 93(4):485–498, 2012.

[114] Vikki Thompson, Alan T Kennedy-Asser, Emily Vosper, YT Eunice Lo, Chris Huntingford, Oliver Andrews, Matthew Collins, Gabrielle C Hegerl, and Dann Mitchell. The 2021 western north america heat wave among the most extreme events ever recorded globally. *Science Advances*, 8(18):eabm6860, 2022.

[115] Dimitri V Val. Factors affecting life-cycle cost analysis of RC structures in chloride contaminated environments. *Journal of infrastructure systems*, 13(2):135–143, 2007.

[116] Dimitri V Val and Pavel A Trapper. Probabilistic evaluation of initiation time of chloride-induced corrosion. *Reliability Engineering & System Safety*, 93(3):364–372, 2008.

[117] CR Vallarino. Fitting the log-linear rate to poisson processes. In *Proceedings., Annual Reliability and Maintainability Symposium*, pages 257–261. IEEE, 1989.

[118] Ruben Van Coile, Robby Caspeele, and Luc Taerwe. Lifetime cost optimization for the structural fire resistance of concrete slabs. *Fire technology*, 50(5):1201–1227, 2014.

[119] TD Van Der Pol, EC Van Ierland, S Gabbert, H-P Weikard, and EMT Hendrix. Impacts of rainfall variability and expected rainfall changes on cost-effective adaptation of water systems to climate change. *Journal of Environmental Management*, 154:40–47, 2015.

[120] Jan M van Noortwijk and Johannes AM van der Weide. Applications to continuous-time processes of computational techniques for discrete-time renewal processes. *Reliability Engineering & System Safety*, 93(12):1853–1860, 2008.

[121] Arun Veeramany and Mahesh D Pandey. Reliability analysis of nuclear component cooling water system using semi-markov process model. *Nuclear Engineering and Design*, 241(5):1799–1806, 2011.

[122] Arun Veeramany and Mahesh D Pandey. Reliability analysis of nuclear piping system using semi-markov process model. *Annals of Nuclear Energy*, 38(5):1133–1139, 2011.

[123] B Sharanbaswa Vishwanath and Swagata Banerjee. Considering uncertainty in corrosion process to estimate life-cycle seismic vulnerability and risk of aging bridge piers. *Reliability Engineering & System Safety*, 232:109050, 2023.

[124] Kim Anh T Vu and Mark G Stewart. Structural reliability of concrete bridges including improved chloride-induced corrosion models. *Structural safety*, 22(4):313–333, 2000.

[125] Abraham Wald. On cumulative sums of random variables. *The Annals of Mathematical Statistics*, 15(3):283–296, 1944.

[126] Y. K. Wen. Minimum lifecycle cost design under multiple hazards. *Reliability Engineering and System Safety*, 73(3):223–231, 2001.

[127] Y. K. Wen. Reliability and performance-based design. *Structural Safety*, 23(4):407–428, 2001.

[128] Rachel H White, Sam Anderson, James F Booth, Ginni Braich, Christina Draeger, Cuiyi Fei, Christopher DG Harley, Sarah B Henderson, Matthias Jakob, Carie-Ann

Lau, et al. The unprecedented pacific northwest heatwave of june 2021. *Nature Communications*, 14(1):727, 2023.

[129] Yi Wu, Chiyuan Miao, Xuewei Fan, Jiaojiao Gou, Qi Zhang, and Haiyan Zheng. Quantifying the uncertainty sources of future climate projections and narrowing uncertainties with bias correction techniques. *Earth's Future*, 10(11):e2022EF002963, 2022.

[130] Jin Xia, Wei-Liang Jin, and Long-Yuan Li. Effect of chloride-induced reinforcing steel corrosion on the flexural strength of reinforced concrete beams. *Magazine of Concrete Research*, 64(6):471–485, 2012.

[131] Jiabo Yin, Pierre Gentine, Louise Slater, Lei Gu, Yadu Pokhrel, Naota Hanasaki, Shenglian Guo, Lihua Xiong, and Wolfram Schlenker. Future socio-ecosystem productivity threatened by compound drought–heatwave events. *Nature Sustainability*, 6(3):259–272, 2023.

[132] Ahmed Yosri, Yasser Elleathy, Sonia Hassini, and Wael El-Dakhakhni. Genetic algorithm-Markovian model for predictive bridge asset management. *Journal of Bridge Engineering*, 26(8):04021052, 2021.

[133] Jieying Zhang and Zoubir Lounis. Sensitivity analysis of simplified diffusion-based corrosion initiation model of concrete structures exposed to chlorides. *Cement and concrete research*, 36(7):1312–1323, 2006.

Appendix A

Estimated Parameters for Precipitation Analysis

A.1 Stationary case (1950-1990): Benchmark Case

Table A.1: Estimated parameters of the Gumbel distributions and the Homogeneous Poisson Process for all the climate models for the stationary benchmark scenario i.e. 1950-1990 period.

Model	μ	σ	λ	α	β
Units	mm/day	mm/day	per year	-	mm/day
KACE.1.0.G	33.43	9.15	2.93	0.94	8.52
HadGEM3.GC31.LL	37.01	7.37	3.55	0.96	8.55
UKESM1.0.LL	34.26	8.33	3.08	1.06	8.81
CMCC.ESM2	36.71	10.92	2.95	0.99	10.37
GFDL.ESM4	34.60	9.67	3.28	0.99	7.91
BCC.CSM2.MR	35.04	10.78	3.40	0.80	7.48
INM.CM4.8	34.50	9.86	2.93	0.87	7.93
FGOALS.g3	36.90	10.62	3.28	0.94	9.13
TaiESM1	35.61	8.86	3.03	0.85	8.44
NorESM2.MM	33.93	10.27	3.30	0.90	8.49
CanESM5	33.83	7.64	3.20	0.98	7.57
KIOST.ESM	36.57	8.79	3.13	1.00	8.71
NorESM2.LM	35.35	9.69	3.33	0.93	8.83
INM.CM5.0	34.85	9.73	3.08	0.92	8.73
IPSL.CM6A.LR	35.20	9.36	3.13	0.96	8.43
CNRM.CM6.1	35.33	8.95	3.35	0.96	8.75
MIROC6	34.05	8.31	3.00	1.08	8.93
MIROC.ES2L	36.20	9.80	3.10	0.98	9.45
CNRM.ESM2.1	34.26	7.92	3.35	1.03	8.15
MRI.ESM2.0	35.51	8.90	3.30	1.02	9.22
EC.Earth3	34.46	6.89	3.18	0.94	7.43
MPI.ESM1.2.LR	33.60	7.91	3.38	0.95	7.69
MPI.ESM1.2.HR	34.54	10.01	2.90	0.97	8.90
EC.Earth3.Veg	36.80	9.05	3.23	0.94	9.38
ACCESS.ESM1.5	35.78	9.61	3.23	0.98	9.26
ACCESS.CM2	33.50	8.15	3.18	1.00	8.66

A.2 Non-stationary Case I: 2020-2100 Period

A.2.1 Non-stationary Gumbel parameters

Table A.2: Estimated Parameters of non-stationary Gumbel distributions for all models in the period 2020-2100.

Model	μ_0	μ_1	σ_0	σ_1
Units	mm/day	$mm/day/year$	mm/day	$mm/day/year$
KACE.1.0.G	38.84	0.08	11.00	0.00
HadGEM3.GC31.LL	36.01	0.13	8.60	0.07
UKESM1.0.LL	35.99	0.11	5.90	0.09
CMCC.ESM2	42.02	0.00	11.00	0.05
GFDL.ESM4	39.70	0.05	7.87	0.08
BCC.CSM2.MR	33.98	0.09	9.24	0.00
INM.CM4.8	35.79	0.09	9.93	0.00
FGOALS.g3	37.22	0.11	9.71	0.03
TaiESM1	35.23	0.17	7.88	0.04
NorESM2.MM	31.91	0.13	8.69	0.04
CanESM5	34.66	0.19	11.00	0.03
KIOST.ESM	39.97	0.08	9.63	0.01
NorESM2.LM	33.29	0.14	8.26	0.06
INM.CM5.0	36.71	0.03	10.25	0.02
IPSL.CM6A.LR	32.10	0.17	6.56	0.08
CNRM.CM6.1	41.56	0.03	11.00	0.03
MIROC6	38.08	0.12	10.65	0.05
MIROC.ES2L	33.37	0.19	8.14	0.06
CNRM.ESM2.1	33.44	0.20	6.62	0.10
MRI.ESM2.0	35.95	0.10	9.78	0.03
EC.Earth3	42.76	0.07	10.48	0.04
MPI.ESM1.2.LR	35.16	0.11	9.77	0.02
MPI.ESM1.2.HR	39.46	0.00	8.89	0.04
EC.Earth3.Veg	40.24	0.12	11.00	0.03
ACCESS.ESM1.5	39.13	0.07	10.61	0.03
ACCESS.CM2	40.28	0.02	9.33	0.04

A.2.2 NHPP parameters

Table A.3: Estimated Parameters of Non-homogeneous Poisson process for all models in the period 2020-2100.

Model	λ_0	λ_1	x_0	α	β_0	β_1
Units	per year	per $year^2$	mm/day	-	mm/day	$mm/day/year$
KACE.1.0.G	1.0310	0.0028	30.0	0.9504	10.54	0.0160
HadGEM3.GC31.LL	1.3096	0.0021	26.0	1.0000	8.26	0.0730
UKESM1.0.LL	0.9859	0.0081	28.0	1.0521	9.99	0.0050
CMCC.ESM2	1.0296	0.0000	29.0	1.0218	11.56	0.0316
GFDL.ESM4	1.4102	0.0016	26.0	0.9603	8.34	0.0510
BCC.CSM2.MR	1.1775	0.0040	26.0	0.8858	6.65	0.0404
INM.CM4.8	1.0134	0.0042	26.0	0.9253	9.67	0.0000
FGOALS.g3	0.8825	0.0061	29.0	1.0523	9.76	0.0376
TaiESM1	1.2244	0.0032	28.0	1.1134	8.08	0.0663
NorESM2.MM	0.4853	0.0100	29.0	0.9580	8.61	0.0172
CanESM5	0.5924	0.0089	30.0	0.9149	9.59	0.0458
KIOST.ESM	0.8343	0.0080	29.0	1.0010	11.55	0.0037
NorESM2.LM	0.7159	0.0062	28.0	0.9680	8.59	0.0581
INM.CM5.0	0.4606	0.0071	30.0	0.9810	10.94	0.0000
IPSL.CM6A.LR	0.7354	0.0077	27.0	1.0642	8.01	0.0721
CNRM.CM6.1	1.0474	0.0088	27.0	0.8204	9.54	0.0000
MIROC6	0.6872	0.0065	30.0	0.9774	9.81	0.0558
MIROC.ES2L	0.7533	0.0065	30.0	1.0681	7.74	0.0888
CNRM.ESM2.1	0.6912	0.0090	30.0	1.0480	7.53	0.0725
MRI.ESM2.0	0.6269	0.0085	30.0	0.9706	9.38	0.0269
EC.Earth3	1.1177	0.0047	28.0	0.9439	10.65	0.0214
MPI.ESM1.2.LR	0.6559	0.0073	29.0	1.0025	9.59	0.0186
MPI.ESM1.2.HR	1.1787	0.0000	27.0	1.0638	11.20	0.0000
EC.Earth3.Veg	1.2319	0.0065	26.0	0.9260	10.90	0.0079
ACCESS.ESM1.5	1.0799	0.0031	29.0	0.9754	9.85	0.0343
ACCESS.CM2	0.7048	0.0077	31.0	1.0078	10.62	0.0155

A.3 Non-stationary Case II: 2070-2100 Period

A.3.1 Non-stationary Gumbel parameters

Table A.4: Estimated Parameters of non-stationary Gumbel distributions for all models in the period 2070-2100.

Model	μ_0	μ_1	σ_0	σ_1
Units	mm/day	$mm/day/year$	mm/day	$mm/day/year$
KACE.1.0.G	44.304	0.010	13.335	-0.200
HadGEM3.GC31.LL	48.780	-0.300	13.290	-0.153
UKESM1.0.LL	44.110	-0.069	9.233	-0.026
CMCC.ESM2	34.693	0.480	15.435	-0.200
GFDL.ESM4	44.051	-0.115	6.763	0.314
BCC.CSM2.MR	37.598	0.162	8.028	-0.022
INM.CM4.8	39.998	0.090	8.463	0.015
FGOALS.g3	41.478	0.276	12.706	-0.094
TaiESM1	45.255	0.093	10.452	-0.006
NorESM2.MM	36.242	0.262	9.223	0.163
CanESM5	41.784	0.387	12.034	-0.009
KIOST.ESM	43.787	0.070	6.768	0.161
NorESM2.LM	41.501	-0.046	11.283	0.029
INM.CM5.0	37.279	0.057	11.697	0.001
IPSL.CM6A.LR	44.114	-0.024	14.608	-0.200
CNRM.CM6.1	40.499	0.308	10.341	0.152
MIROC6	40.732	0.480	16.565	-0.200
MIROC.ES2L	48.051	-0.046	14.269	-0.200
CNRM.ESM2.1	42.769	0.165	8.880	0.225
MRI.ESM2.0	35.798	0.409	10.451	0.056
EC.Earth3	46.231	0.112	8.233	0.327
MPI.ESM1.2.LR	36.180	0.480	10.348	-0.072
MPI.ESM1.2.HR	39.035	-0.085	9.666	0.141
EC.Earth3.Veg	51.567	-0.114	14.071	-0.069
ACCESS.ESM1.5	37.673	0.375	11.886	-0.002
ACCESS.CM2	39.173	0.166	11.774	0.086

A.3.2 NHPP parameters

Table A.5: Estimated Parameters of Non-homogeneous Poisson process for all models in the period 2020-2100.

Model	λ_0	λ_1	x_0	α	β_0	β_1
Units	per year	per $year^2$	mm/day	-	mm/day	$mm/day/year$
KACE.1.0.G	1.1783	0.0039	30.0	1.1371	11.6874	0.0365
HadGEM3.GC31.LL	1.5002	-0.0177	26.0	1.0273	12.5066	-0.0100
UKESM1.0.LL	1.3396	-0.0048	28.0	1.0917	9.7390	0.0458
CMCC.ESM2	0.7715	0.0231	29.0	0.9259	12.9088	-0.0100
GFDL.ESM4	1.1785	0.0014	26.0	1.0891	12.5747	-0.0100
BCC.CSM2.MR	1.1491	0.0133	26.0	1.1105	10.0155	-0.0100
INM.CM4.8	1.3918	-0.0036	26.0	0.9258	9.2325	0.0113
FGOALS.g3	1.2769	-0.0013	29.0	1.0638	10.2030	0.1507
TaiESM1	1.2840	-0.0042	28.0	1.1669	10.5868	0.1118
NorESM2.MM	1.2780	0.0074	29.0	0.9966	9.6744	0.0550
CanESM5	1.2929	0.0028	30.0	1.0245	10.3152	0.2025
KIOST.ESM	1.0774	0.0140	29.0	1.0529	12.1425	-0.0100
NorESM2.LM	1.5266	-0.0121	28.0	0.9319	10.4679	0.0379
INM.CM5.0	0.7780	0.0227	30.0	1.1226	12.4962	-0.0100
IPSL.CM6A.LR	1.4439	-0.0070	27.0	0.9781	10.9472	0.0741
CNRM.CM6.1	0.9607	0.0234	27.0	0.9740	12.2163	-0.0100
MIROC6	0.7850	0.0284	30.0	0.8996	11.1667	0.0996
MIROC.ES2L	1.2840	0.0034	30.0	0.9514	12.4578	-0.0100
CNRM.ESM2.1	0.9446	0.0203	30.0	1.0146	10.1850	0.0886
MRI.ESM2.0	0.6029	0.0364	30.0	1.0381	10.3754	0.0941
EC.Earth3	1.3651	-0.0059	28.0	1.0541	11.6439	0.0694
MPI.ESM1.2.LR	1.0338	0.0150	29.0	1.0928	7.9728	0.2001
MPI.ESM1.2.HR	1.0821	0.0057	27.0	1.1022	10.1656	0.0738
EC.Earth3.Veg	1.2828	0.0001	26.0	0.9628	12.8857	0.0374
ACCESS.ESM1.5	1.0115	0.0119	29.0	0.9141	9.2185	0.1168
ACCESS.CM2	1.1194	0.0120	31.0	0.9952	11.1257	0.0489

Appendix B

Markov transition probabilities

B.1 Markov probabilities

The estimated transition probabilities for the Markov condition states for the provinces of British Columbia, Ontario, Quebec and Nova Scotia are presented here for the RCP4.5 and RCP8.5 carbon emission scenarios and cover depth of 25, 35 and 60 mm until 2100. The tables B.1 to B.4 can be used to predict the probabilities and expected bridge condition states in the future based on the inspected condition state at present.

Table B.1: Probabilities for British Columbia

Cover	Probabilities	RCP4.5				RCP8.5			
		2021-2040	2041-2060	2061-2080	2081-2100	2021-2040	2041-2060	2061-2080	2081-2100
25 mm	$p_{1,1}$	0.6142	0.5885	0.5697	0.5596	0.6129	0.5751	0.5314	0.4963
	$p_{2,2}$	0.8027	0.7909	0.7821	0.7771	0.802	0.7846	0.7621	0.7497
	$p_{3,3}$	0.4227	0.4136	0.4088	0.4023	0.4261	0.3996	0.3908	0.4069
	$p_{4,4}$	0.4427	0.4368	0.43	0.4321	0.4398	0.4355	0.423	0.4212
	$p_{5,5}$	0.455	0.4582	0.4572	0.4554	0.4565	0.4524	0.4486	0.4561
35 mm	$p_{1,1}$	0.758	0.7385	0.7225	0.7119	0.7562	0.7271	0.6838	0.6338
	$p_{2,2}$	0.8856	0.8811	0.8781	0.8752	0.8853	0.8782	0.868	0.8583
	$p_{3,3}$	0.7562	0.7558	0.7592	0.7574	0.7572	0.7548	0.7542	0.7535
	$p_{4,4}$	0.7462	0.7488	0.7495	0.7481	0.747	0.747	0.7469	0.7473
	$p_{5,5}$	0.7591	0.7614	0.7624	0.76	0.7572	0.7595	0.7596	0.7627
60 mm	$p_{1,1}$	0.8948	0.8865	0.8791	0.8734	0.894	0.8804	0.8604	0.8389
	$p_{2,2}$	0.9664	0.9656	0.9649	0.9641	0.9662	0.9649	0.9629	0.9612
	$p_{3,3}$	0.9432	0.9439	0.9443	0.9438	0.9429	0.9436	0.944	0.9448
	$p_{4,4}$	0.9427	0.9436	0.944	0.9436	0.9422	0.9435	0.9438	0.9448
	$p_{5,5}$	0.9462	0.947	0.9476	0.9472	0.9459	0.947	0.9474	0.9483

Table B.2: Probabilities for Ontario

Cover	Probabilities	RCP4.5				RCP8.5			
		2021-2040	2041-2060	2061-2080	2081-2100	2021-2040	2041-2060	2061-2080	2081-2100
25 mm	$p_{1,1}$	0.6777	0.6361	0.6087	0.5989	0.6695	0.6087	0.5505	0.5061
	$p_{2,2}$	0.8245	0.8110	0.7997	0.7947	0.8223	0.7991	0.7725	0.7526
	$p_{3,3}$	0.4552	0.4422	0.4386	0.4282	0.4528	0.4231	0.4092	0.4199
	$p_{4,4}$	0.4758	0.4630	0.4580	0.4576	0.4726	0.4572	0.4405	0.4339
	$p_{5,5}$	0.4665	0.4687	0.4691	0.4679	0.4673	0.4641	0.4618	0.4632
35 mm	$p_{1,1}$	0.8016	0.7738	0.7546	0.7446	0.7952	0.7542	0.7038	0.6476
	$p_{2,2}$	0.8964	0.8897	0.8852	0.8830	0.8945	0.8845	0.8735	0.8614
	$p_{3,3}$	0.7580	0.7598	0.7624	0.7603	0.7585	0.7588	0.7607	0.7593
	$p_{4,4}$	0.7488	0.7515	0.7524	0.7522	0.7492	0.7499	0.7498	0.7518
	$p_{5,5}$	0.7606	0.7630	0.7646	0.7633	0.7581	0.7623	0.7633	0.7653
60 mm	$p_{1,1}$	0.9123	0.9016	0.8937	0.8884	0.9098	0.8932	0.8700	0.8438
	$p_{2,2}$	0.9685	0.9675	0.9666	0.9658	0.9681	0.9664	0.9641	0.9619
	$p_{3,3}$	0.9429	0.9440	0.9444	0.9441	0.9425	0.9441	0.9446	0.9455
	$p_{4,4}$	0.9422	0.9435	0.9439	0.9438	0.9419	0.9437	0.9447	0.9455
	$p_{5,5}$	0.9457	0.9468	0.9476	0.9474	0.9453	0.9472	0.9481	0.9490

Table B.3: Probabilities for Quebec

Cover	Probab-ilities	RCP4.5				RCP8.5			
		2021-2040	2041-2060	2061-2080	2081-2100	2021-2040	2041-2060	2061-2080	2081-2100
25 mm	$p_{1,1}$	0.7340	0.6907	0.6635	0.6474	0.7249	0.6634	0.5893	0.5309
	$p_{2,2}$	0.8391	0.8273	0.8186	0.8114	0.8370	0.8177	0.7895	0.7627
	$p_{3,3}$	0.4626	0.4579	0.4621	0.4471	0.4627	0.4463	0.4246	0.4215
	$p_{4,4}$	0.4856	0.4786	0.4822	0.4764	0.4862	0.4758	0.4521	0.4470
	$p_{5,5}$	0.4749	0.4781	0.4769	0.4687	0.4727	0.4701	0.4638	0.4698
35 mm	$p_{1,1}$	0.8384	0.8104	0.7909	0.7799	0.8319	0.7911	0.7387	0.6787
	$p_{2,2}$	0.9056	0.8986	0.8934	0.8893	0.9035	0.8930	0.8803	0.8674
	$p_{3,3}$	0.7530	0.7570	0.7614	0.7591	0.7525	0.7582	0.7606	0.7618
	$p_{4,4}$	0.7491	0.7519	0.7529	0.7507	0.7487	0.7496	0.7510	0.7537
	$p_{5,5}$	0.7586	0.7628	0.7635	0.7618	0.7564	0.7608	0.7631	0.7667
60 mm	$p_{1,1}$	0.9263	0.9161	0.9081	0.9027	0.9239	0.9080	0.8854	0.8581
	$p_{2,2}$	0.9701	0.9690	0.9680	0.9670	0.9697	0.9678	0.9654	0.9628
	$p_{3,3}$	0.9412	0.9430	0.9435	0.9430	0.9414	0.9430	0.9441	0.9452
	$p_{4,4}$	0.9408	0.9424	0.9430	0.9426	0.9406	0.9425	0.9440	0.9453
	$p_{5,5}$	0.9441	0.9457	0.9465	0.9461	0.9439	0.9459	0.9475	0.9487

Table B.4: Probabilities for Nova Scotia

Cover		RCP4.5				RCP8.5			
		2021-2040	2041-2060	2061-2080	2081-2100	2021-2040	2041-2060	2061-2080	2081-2100
25 mm	$p_{1,1}$	0.7501	0.7172	0.7018	0.6917	0.744	0.6986	0.644	0.5951
	$p_{2,2}$	0.8464	0.8363	0.8329	0.8278	0.8443	0.8311	0.8116	0.7916
	$p_{3,3}$	0.4488	0.4463	0.4556	0.4483	0.4472	0.4404	0.4215	0.4101
	$p_{4,4}$	0.4635	0.4547	0.4673	0.4605	0.4621	0.4571	0.4434	0.429
	$p_{5,5}$	0.4636	0.4646	0.4662	0.459	0.4645	0.4589	0.4456	0.4536
35 mm	$p_{1,1}$	0.849	0.8278	0.8168	0.8098	0.8453	0.8154	0.7783	0.7419
	$p_{2,2}$	0.9098	0.903	0.9006	0.8974	0.9076	0.8995	0.8893	0.8811
	$p_{3,3}$	0.7422	0.745	0.7513	0.7482	0.7407	0.7469	0.749	0.7551
	$p_{4,4}$	0.7439	0.745	0.7456	0.7436	0.7426	0.7415	0.7432	0.7463
	$p_{5,5}$	0.7516	0.7544	0.7552	0.7528	0.7493	0.7531	0.7521	0.7577
60 mm	$p_{1,1}$	0.9306	0.9228	0.9186	0.9154	0.9288	0.9178	0.903	0.8871
	$p_{2,2}$	0.9707	0.9696	0.969	0.9683	0.9702	0.9688	0.9669	0.9651
	$p_{3,3}$	0.9393	0.9408	0.941	0.9408	0.9389	0.9408	0.9418	0.9429
	$p_{4,4}$	0.9387	0.94	0.9403	0.9401	0.9381	0.9401	0.9413	0.9425
	$p_{5,5}$	0.9419	0.9434	0.9436	0.9433	0.9413	0.9435	0.9446	0.9459

Appendix C

Formulas for computing risk

C.1 Variance and second moment of damage costs

The second moment of the damaged cost can be defined as follows:

$$E[(K_D(t))^2] = \Sigma_{n=1}^{\infty} E[(C_1 e^{-\rho S_1} + C_2 e^{-\rho S_2} + ... + C_{N(t)} e^{-\rho S_{N(t)}})^2 | N(t) = n] P_N(n) \quad \text{(C.1)}$$

$$= \int ... \int_{0<s_{(1)}<...<s_{(n)}<t} (C_1 e^{-\rho s_{(1)}} + ... + C_n e^{-\rho s_{(n)}})^2 \\ f_{s_{(1)}...s_{(n)}}(s_{(1)}, ..., s_{(n)}) ds_{(1)} ... ds_{(n)} \quad \text{(C.2)}$$

Since the above expression, the integrand is permutable, the ordered set of arrival time variables can be converted into an unordered set of variables and the integration can be carried out as follows:

$$= \int_0^t \int_0^t ... \int_0^t (C_1 e^{-\rho S_1} + C_2 e^{-\rho S_2} + ... + C_{N(t)} e^{-\rho S_{N(t)}})^2 \\ f(s_1) f(s_2) ... f(s_n) ds_1 ... ds_n \quad \text{(C.3)}$$

$$= \int_0^t \int_0^t ... \int_0^t (E[C^2](e^{-2\rho s_1} + e^{-2\rho s_2} + ..(n\ terms).. + e^{-2\rho s_n}) + 2(E[C])^2(e^{-\rho(s_1+s_2)} + .. \left(\frac{n(n-1)}{2}\ terms\right) .. + e^{-\rho(s_{n-1}+s_n)})) f(s_1)f(s_2)...f(s_n)ds_1...ds_n \quad (C.4)$$

The above equation can be simplified to the following expression:

$$= \mu_{2C}\left[n\int_0^t e^{-2\rho s} f(s)ds\right] + \mu_C^2\left[\frac{n(n-1)}{2}2\left[\int_0^t e^{-\rho s} f(s)ds\right]^2\right] \quad (C.5)$$

$$= \mu_{2C}\left[n\int_0^t e^{-2\rho s} \frac{\lambda_f(s)}{\Lambda_f(t)}ds\right] + \mu_C^2\left[\frac{n(n-1)}{2}2\left[\int_0^t e^{-\rho s} \frac{\lambda_f(s)}{\Lambda(t)}ds\right]^2\right] \quad (C.6)$$

$$= \frac{n\mu_{2C}}{\Lambda_f(t)}\left[\int_0^t e^{-2\rho s}\lambda_f(s)ds\right] + \frac{n(n-1)\mu_C^2}{[\Lambda_f(t)]^2}\left[\int_0^t e^{-\rho s}\lambda_f(s)ds\right]^2 \quad (C.7)$$

$$= \frac{n\mu_{2C}}{\Lambda_f(t)}I_1(\rho,t) + \frac{n(n-1)\mu_C^2}{[\Lambda_f(t)]^2}I_2(\rho,t) \quad (C.8)$$

where, $I_1(\rho,t) = \left[\int_0^t e^{-2\rho s}\lambda_f(s)ds\right]$ and $I_2(\rho,t) = \left[\int_0^t e^{-\rho s}\lambda_f(s)ds\right]^2$. Substituting back and applying total expectation theorem we get,

$$E[(K_D(t))^2] = \Sigma_{n=1}^{\infty}\left[\frac{n\mu_{2C}}{\Lambda_f(t)}I_1(\rho,t) + \frac{n(n-1)\mu_C^2}{[\Lambda_f(t)]^2}I_2(\rho,t)\right]P_N(n) \quad (C.9)$$

Let us consider each term in the above equation one by one. The first term is expanded as follows:

$$Term\ I = \Sigma_{n=1}^{\infty}\left[\frac{n\mu_{2C}}{\Lambda_f(t)}I_1(\rho,t)\right]P_N(n) \quad (C.10)$$

$$= \Sigma_{n=1}^{\infty}\left[\frac{n\mu_{2C}}{\Lambda_f(t)}I_1(\rho,t)\right]\frac{e^{-\Lambda_f(t)}[\Lambda_f(t)]^n}{n!} \quad (C.11)$$

$$= \mu_{2C}I_1(\rho,t) = \mu_{2C}\int_0^t e^{-2\rho s}\lambda_f(s)ds \quad (C.12)$$

Similarly, the second term gives the following.

$$Term\ II = \Sigma_{n=1}^{\infty}\left[\frac{n(n-1)\mu_C^2}{[\Lambda_f(t)]^2}I_2(\rho,t)\right]P_N(n) \tag{C.13}$$

$$= \mu_{2C}I_2(\rho,t) = \mu_C^2\left[\int_0^t e^{-\rho s}\lambda_f(s)ds\right]^2 \tag{C.14}$$

Substituting the terms back in Equation (C.9), the second moment is obtained as:

$$E[(K_D(t))^2] = \mu_{2C}\int_0^t e^{-2\rho s}\lambda_f(s)ds + \left[\mu_C\int_0^t e^{-\rho s}\lambda_f(s)ds\right]^2 \tag{C.15}$$

$$= \mu_{2C}\int_0^t e^{-2\rho s}\lambda_f(s)ds + \left(E[K_D(t)]\right)^2 \tag{C.16}$$

Therefore the variance is obtained as:

$$Var[K_D(t)] = E[(K_D(t))^2] - \left(E[K_D(t)]\right)^2 \tag{C.17}$$

$$= \mu_{2C}\int_0^t e^{-2\rho s}\lambda_f(s)ds \tag{C.18}$$

The undiscounted variance can be obtained by putting $\rho = 0$, in Equation (C.17), as follows:

$$Var[K(t)] = \mu_{2C}\int_0^t \lambda_f(s)ds = \mu_{2C}\Lambda_f(t) \tag{C.19}$$

For an HPP, the variances of the discounted and undiscounted LCC reduces to

$$Var[K_D(t)]_{HPP} = \mu_{2C}\lambda_f\int_0^t e^{-2\rho s}ds = \frac{\mu_{2C}\lambda_f}{2\rho}(1-e^{-2\rho t}) \tag{C.20}$$

and

$$Var[K(t)]_{HPP} = \mu_{2C}\lambda_f t \tag{C.21}$$

C.2 Distribution

It was observed that the distribution of net damage costs for a stationay poisson process in [84] can be generalized for a NHPP for IID damage costs. The detailed derivation for this generalization is provided as follows.

For the NHPP failure process $N_f(t)$, the probability of the number of events n in a given time t, is Poisson distributed with a mean value of $\Lambda_f(t)$ can be rewritten in a recursive format as:

$$f_{N_f(t)}(n) \;=\; \begin{cases} e^{-\Lambda_f(t)} & n = 0 \\ \dfrac{[\Lambda_f(t)]}{n} f_{N_f(t)}(n-1) & n \geq 1 \end{cases} \tag{C.22}$$

The distribution of the undiscounted LCC as given in **??** conditioned on the number of events $N_f(t) = n$, is given by the n-fold convolution of the PMF of C, $f_C(i\delta)$ and which also can be represented in a recursive format as shown below:

$$\begin{aligned} P[K(t) = i\delta | N(t) = n] \;&= f_C^{(n)}(i\delta) \\ &= \sum_{j=0}^{i} f_C^{(n-1)}((i-j)\delta) f_C(j\delta) \end{aligned} \tag{C.23}$$

where $i = 0, 1, 2, ...$ is the integer multiple of some unit cost δ. Here we use the result $f_C^{(0)}(0) = 1$ and $f_C^{(0)}(i\delta) = 0$. Using the total probability theorem, the expectation over the number of failures in time, t, can be expressed as an infinite sum as below:

$$\begin{aligned} f_{K(t)}(i\delta) &= \sum_{n=0}^{\infty} P[K(t) = i\delta | N_f(t) = n] f_{N_f(t)}(n) \\ &= \sum_{n=0}^{\infty} f_C^{(n)}(i\delta) f_{N_f(t)}(n) \\ &= \sum_{n=1}^{\infty} f_C^{(n)}(i\delta) f_{N_f(t)}(n), \;\; for \; i \geq 1 \end{aligned} \tag{C.24}$$

One more useful result that comes to our aid is the recursive formulation of the convo-

lution of discrete distributions using which $f_C^{(n)}(i\delta)$ in Equation (C.24) can be represented as follows:

$$\frac{1}{n} f_C^{(n)}(i\delta) \;=\; \sum_{j=1}^{i} f_C(j\delta) f_C^{(n-1)}((i-j)\delta) \tag{C.25}$$

Once, the Equations (C.24) and (C.25) are combined and simplified, the PMF of the LCC can be obtained as a simple recursive formulation known as Panjer's recursion used in reliability analyses [120] as:

$$f_{K(t)}(i\delta) = \Lambda_f(t) \sum_{j=1}^{i} \frac{j}{i} f_C(j\delta) f_{K(t)}((i-j)\delta). \;\; i \geq 1 \tag{C.26}$$

For the case $i = 0$,the following can be seen:

$$\begin{aligned} f_{K(t)}(0) &= \sum_{n=0}^{\infty} P[K(t) = 0 | N_f(t) = n] f_{N_f(t)}(n) \\ &= \sum_{n=0}^{\infty} f_C^{(n)}(0) f_{N_f(t)}(n) \\ &= \sum_{n=0}^{\infty} [f_C(0)]^n e^{-\Lambda(t)} \frac{[\Lambda(t)]^n}{n!} \\ &= e^{-\Lambda(t)} \sum_{n=0}^{\infty} \frac{[\Lambda(t) f_C(0)]^n}{n!} \\ &= e^{-\Lambda(t)} e^{\Lambda(t) f_C(0)} = e^{\Lambda(t)(1 - f_C(0))} \end{aligned} \tag{C.27}$$

Using a linear mean value function $\Lambda(t)$, will give the results for an HPP as produced by [84]. Another thing to note here is that in all the above equations, the limits of integration can be changed from $(0, t)$ to any other time interval (t_1, t_2) to obtain the different statistics of the damage cost in that time interval. This is one of the robust features of NHPP models.